UNIVERSITÀ DEGLI STUDI DI TRIESTE

Sede Amministrativa del Dottorato di Ricerca

XIX ciclo del Dottorato di Ricerca in Fisica

Chemical evolution of neutron capture elements in our Galaxy and in the dwarf spheroidal galaxies of the Local Group

Settore scientifico-disciplinare: FIS/05 ASTRONOMIA E ASTROFISICA

DOTTORANDO
GABRIELE CESCUTTI

COORDINATORE DEL COLLEGIO DEI DOCENTI
PROF. GAETANO SENATORE

TUTORE
PROF. FRANCESCA MATTEUCCI

RELATORE
PROF. FRANCESCA MATTEUCCI

Anno Accademico 2005/2006

I dedicate this work to
my mother
my father
and
my brother

Abstract

We model the evolution of the abundances of several neutron capture elements (Ba, Eu, La, Sr, Y and Zr) in the Milky Way and then we extend our predictions to some dwarf spheroidal galaxies of the Local Group.

Two major neutron capture mechanisms on iron seeds are generally invoked: the slow process (s-process) and the rapid process (r-process), where the slow and the rapid are defined relative to the timescale of the β-decay. Nucleosynthesis calculations for r-process are very few, owing to the difficulties in modelling the physics the r-process and the lack of knowledge about the sites of productions of these elements. For s-process elements instead some calculations are available but the sites of production are also uncertain.

By adopting a chemical evolution model for the Milky Way already reproducing the evolution of several chemical elements (H, He, C, N, O, α-elements and iron peak elements), we compare our theoretical results with accurate and new stellar data of neutron capture elements and we are able to impose strong constraints on the nucleosynthesis of the studied elements. We can suggest the stellar sites of production for each element. In particular, the r-process component of each element (if any) is produced in the mass range from 10 to 30 $M_{\odot}$, whereas the s-process component arises from stars in the range from 1 to 3 $M_{\odot}$.

Using the same chemical evolution model, extended to different galactocentric distances, we obtain results on the radial gradients of the Milky Way. We compare the results of the model not only for the neutron capture elements but also for α-elements and iron peak elements with new data of Cepheids stars. For the first time with these data, it is possible to verify the predictions for the gradients of very heavy elements. We conclude that the model, with an inside-out scenario for the building up of the disc and a constant density distribution of the gas for the halo phase, can be considered successful; in fact, for almost all the considered elements with our nucleosynthesis prescriptions, the model well reproduces the observed abundance gradients.

We give a possible explanation to the considerable scatter of neutron capture elements observed in low metallicity stars in the solar vicinity, compared to the small star to star scatter observed for the α-elements. In fact, we have developed a stochastic chemical evolution model, in which the main assumption is a random formation of new stars, subject to the condition that the cumulative mass distribution follows a given initial mass function. With our model we are able to reproduce the different features of neutron capture elements and α-elements. The reason for this resides in the random birth of stars coupled with different stellar mass ranges from where α-elements and neutron capture elements originate. In particular, the site of production of α-elements is the whole range of the massive stars, whereas the mass range of production for neutron capture elements has an upper limit of $30M_{\odot}$.

Finally, we test the prescriptions for neutron capture elements also for the dwarf spheroidal galaxies of the Local Group. We use a chemical evolution model already able to reproduce the abundances for α-elements in these systems. We conclude that the same prescriptions used for the Milky Way well reproduce the main features of neutron capture elements also in the dwarf spheroidal galaxies for which we have observational data. In dwarf spheroidal galaxies for which we do not have observational data we only give predictions. We predict that the chemical evolution of these elements in dwarf spheroidal galaxies is different from the evolution in the solar vicinity. This is due to their different histories of star formation relative to our Galaxy and indicates that dwarf spheroidal galaxies (we see nowadays) cannot be the building blocks of our Galaxy.

Contents

Chapter 1

Introduction

"It is written in the stars above" by Depeche Mode

"The stars above us, govern our conditions" by William Shakespeare

1.1 The galactic chemical evolution

Galactic chemical evolution is the study of the evolution in time and in space of the abundances of the chemical elements in the interstellar gas in galaxies. This process is influenced by many parameters such as the initial conditions, the star formation and evolution, the nucleosynthesis and possible gas flows. So, in order to build a chemical evolution model one needs to specify the initial conditions, namely whether the system is closed or open and whether the gas is primordial (no metals [1]) or already chemically enriched. Then, it is necessary to define the stellar birthrate function, which is generally expressed as the product of two independent functions, the star formation rate (SFR) and the initial mass function (IMF), namely:

$$B(m,t) = \psi(t)\varphi(m)\ dt\ dm \tag{1.1}$$

where $\varphi(t)$ is the SFR and $\psi(m)$ is the IMF. The SFR is assumed to be only a function of the time and the IMF only a function of the mass. This oversimplification is due to the absence of a clear knowledge of the star formation process. Moreover, it is necessary to know the stellar evolution ad the nuclear burnings which take place in the stellar interiors during the stellar lifetime and produce new chemical elements, in particular metals. These

---

[1] In astrophysics all the chemical elements heavier than ^{4}He

metals, together with the pristine stellar material are restored into the interstellar medium (ISM) at the star death. This process clearly affects crucially the chemical evolution of the ISM. In order to take in account the elemental production by stars we define the "yields", in particular the stellar yields, as the amount of elements produced by a single star. Finally, the supplementary parameters are the infall of extragalactic gas, radial flows and the galactic winds, which are important ingredients in building galactic chemical evolution models.

The SFR is one of the most important drivers of galactic chemical evolution: it describes the rate at which the gas is turned into stars in galaxies. Since the physics of the star formation process is still not well known, several parameterizations are used to describe the SFR. A common aspect to the different formulations of the SFR is that they include a dependence upon the gas density. Here we recall the most commonly used parameterizations for the SFR adopted so far in the literature. An exponentially decreasing SFR provides an easy to handle formula:

$$\psi(t) = \nu e^{-t/\tau_\star} \tag{1.2}$$

with $\tau_\star$ = 5-15 Gyr in order to obtain a good fit to the properties of the solar neighborhood (Tosi, 1988) and ν= 1 - 2 Gyr^{-1}, being ν the efficiency of star formation which is expressed as the inverse of the timescale of star formation. However, the most famous formulation and most widely adopted for the SFR is the Schmidt (1959) law:

$$\psi(t) = \nu \sigma_{gas}^{k} \tag{1.3}$$

which assumes that the SFR is proportional to some power of the volume or surface gas density (σ_{gas}). The exponent suggested by Schmidt was k = 2 but Kennicutt (1998) suggested that the best fit to the observational data on spiral disks and starburst galaxies is obtained with an exponent k = 1.4± 0.15. A more complex formulation, including a dependence also on the total surface mass density (σ_{tot}), which is induced by the SN feedback, was suggested by the observations of Dopita & Ryder (1994) who proposed the following formulation:

$$\psi(t) = \nu \sigma_{tot}^{k1} \sigma_{gas}^{k2} \tag{1.4}$$

Kennicutt suggested also an alternative law to the Schmidt-like one discussed above:

$$\psi(t) = 0.017 \Omega_{gas} \sigma_{gas} \tag{1.5}$$

being Ω_{gas} the angular rotation speed of the gas.

The IMF is a probability distribution function and the most common parameterization for the IMF is that proposed by Salpeter (1955), which assumes a one-slope power law with x = 1.35, in particular:

$$\varphi(m) = Am^{-(1+x)} \tag{1.6}$$

$\varphi(m)$ is the number of stars with masses in the interval M, M+dM, and A is a normalization constant. The IMF is generally normalized as:

$$\int_0^\infty m\varphi(m)dm = 1 \tag{1.7}$$

More recently, multi-slope expressions of the IMF have been adopted since they better describe the luminosity function of the main sequence stars in the solar vicinity (Scalo 1986, 1998; Kroupa et al. 1993). Generally, the IMF is assumed to be constant in space and time, with some exceptions such as the one suggested by Larson (1998), which adopts a variable slope:

$$x = 1.35(1 + m/m_1)^{-1} \tag{1.8}$$

where m_1 is variable with time and associated to the Jeans mass, (the typical mass at which the internal pressure is no longer strong enough to prevent gravitational collapse). The effects of a variable IMF on the galactic disk properties have been studied by Chiappini et al. (2000), who concluded that only a very "ad hoc" variation of the IMF can reproduce the majority of observational constraints, thus favoring chemical evolution models with IMF constant in space and time.

The stellar yields are fundamental ingredients in galactic chemical evolution. In the past ten years a large number of calculations has become available for stars of all masses and metallicities. However, uncertainties in stellar yields are still present. This is due to uncertainties in the nuclear reaction rates, treatment of convection, mass cut, explosion energies, neutron fluxes and possible fall-back of matter onto the proto-neutron star. Moreover, the ^{14}N nucleosynthesis and its primary and/or secondary nature are still under debate. The most recent calculations are summarized below:

- Low and Intermediate mass stars (0.8 $M_\odot$ <M< 8.0 $M_\odot$) (van den Hoeck & Groenewegen 1997; Meynet & Maeder 2002; Ventura et al. 2002; Siess et al. 2002). These stars produce ^{4}He, C, N and heavy elements (A > 90).

- Massive stars (M > 10 $M_\odot$) (Woosley & Weaver 1995; Langer & Henkel 1995; Thielemann et al. 1996; Nomoto et al. 1997; Rauscher et al. 2002; Limongi & Chieffi 2003).

These stars produce mainly α-elements (O, Ne, Mg, Si, S, Ca), some Fe-peak elements, heavy elements.

- Type Ia SNe (Nomoto et al. 1997; Iwamoto et al. 1999) produce mainly Fe-peak elements.
- Very massive objects (M $> 100M_{\odot}$), if they exist, should produce mostly oxygen (Portinari et al. 1998; Umeda & Nomoto 2001; Nakamura & Umemura 2001).

Depending on the galactic system, the infall rate (IR) can be assumed to be constant in space and time, or more realistically the infall rate can be variable in space and time:

$$IR(r,t) = A(r)e^{-t/\tau(r)} \tag{1.9}$$

with $\tau(r)$ constant or varying along the disk. The parameter A(r) is derived by fitting the present time total surface mass density in the disk of the Galaxy, $\sigma_{tot}(t_{now})$. Otherwise, for the formation of the Galaxy one can assume two independent episodes of infall during which the halo and perhaps part of the thick-disk formed first and then the thin-disk, as in the two-infall model of Chiappini et al. (1997). For the rate of gas outflow or galactic wind there are no specific prescriptions but generally one simply assumes that the wind rate (W) is proportional to the star formation rate (Hartwick 1976, Matteucci & Chiosi 1983):

$$W(t) = -\lambda\psi(t) \tag{1.10}$$

with λ being a free parameter

A good model of chemical evolution should be able to reproduce a minimum number of observational constraints and the number of indipendent observational constraints should be larger than the number of free parameters which are: τ, k_1, k_2, the $\varphi(m)$ slope(s) and the parameter describing the wind, λ if adopted.

The main observational constraints in the Milky Way (see an image in Fig1.1), in particular in the solar vicinity, that a good model should reproduce (see Chiappini et al. 2001) are:

- The present time surface gas density: $\Sigma_{gas} = 13 \pm 3$ M$_{\odot}$pc^{-2}
- The present time surface star density $\Sigma_{\star} = 35 \pm 5$ M$_{\odot}$pc^{-2}
- The present time total surface mass density: $\Sigma_{tot} = 48 \pm 9$ M$_{\odot}$pc^{-2}

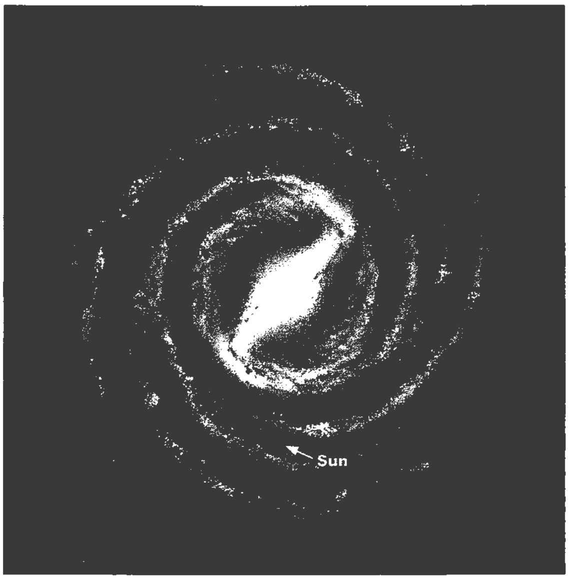

Figure 1.1. An image of the Milky Way in an artist's rendering. Understanding its formation and evolution is fundamental to improve the knowledge of the formation of spiral galaxies and in general of all the galaxies.

- The present time SFR: $\psi_0 = 2$ - $5\mathrm{M}_\odot\ \mathrm{pc}^{-2}\mathrm{Gyr}^{-1}$
- The present time infall rate: 0.3 - $1.5\mathrm{M}_\odot\ \mathrm{pc}^{-2}\ \mathrm{Gyr}^{-1}$
- The present day mass function (PDMF).
- The solar abundances, namely the chemical abundances of the ISM at the time of birth of the solar system 4.5 Gyr ago.
- The age-metallicity relation, namely the relation between the ages of the stars and the metal abundances of their photospheres, assumed to be equivalent to the stellar [Fe/H][2].
- The G-dwarf metallicity distribution, namely the number of stars with a lifetime equal or larger than the age of the Galaxy as a function of their metallicities.
- The distributions of gas and stars formation rate along the disk.

---

[2] We adopt the usual spectroscopic notations that [A/B]= $log_{10}(N_A/N_B)_\star - log_{10}(N_A/N_B)_\odot$ and that $log\epsilon(A) = log_{10}(N_A/N_H) + 12.0$, for elements A and B

- The average SNII and Ia rates along the disk (SNII=1.2±0.8 cen^{-1} and SNIa=0.3±0.2 cen^{-1}).
- The observed abundances in the stars and the [A/Fe] vs. [Fe/H] relations.

The chemical compositions of stars of all Galactic generations contains very important information about the cumulative nucleosynthesis history of the Galaxy. The difference in the timescales for the occurrence of SNII and Ia produces a timedelay in the Fe production relative to the α-elements (Tinsley 1979; Greggio & Renzini 1983b; Matteucci 1986). In fact, in the single degenerate scenario for a SNIa, originally proposed by Whelan and Iben (1973), the SNIa explodes due to a C-deflagration in a C-O white dwarf (WD) reaching the Chandrasekhar mass limit, $M_{Ch}= 1.44M_{\odot}$, after accreting material from a red giant companion. The progenitors of C-O WDs lie in the range 0.8 - 8.0$M_{\odot}$, therefore, the most massive binary system of two C-O WDs is the $8M_{\odot} + 8M_{\odot}$ one. The clock of the system in this scenario is provided by the lifetime of the secondary star (i.e. the less massive one in the binary system). This implies that the minimum timescale for the appearence of the first type Ia SNe is the lifetime of the most massive secondary star. In this case the time is $t_{SNIamin}$=0.03 Gyr (Greggio & Renzini 1983a; Matteucci & Greggio, 1986; Matteucci & Recchi, 2001). On this basis we can interpret all the observed abundance ratios plotted as functions of metallicity. In particular, this interpretation is known as time-delay model and only a model including both contributions in the percentages of 30% (SNII) and 70% (SNIa) can reproduce the data. Moreover, the stars formed near the beginning of our Galaxy have a very low metallicity because their chemical compositions were produced by few previous generations of massive stars. So, studies of elemental abundances in very old and metal poor stars serve as tests of nucleosynthesis theories and galactic chemical evolution models.

1.2 The neutron capture elements

In this thesis we will mainly deal with very heavy elements. Early work by Gilroy et al. (1988) first proposed that the stellar abundances of very heavy elements with respect to iron, particularly [Eu/Fe], showed a large scatter at low metallicities. Their work suggested that this scatter appeared to diminish with increasing metallicity. This was confirmed by the large spread observed in the [Ba/Fe] and [Eu/Fe] ratios in halo stars (e.g. McWilliam et al. 1995; Ryan et al. 1996). A more extensive study by Burris et al. (2000) confirmed the very large star-to-star scatter in the early Galaxy, while studies of stars at higher metallicities, involving mostly disk stars (Edvardsson et al. 1993; Woolf, Tomkin & Lambert 1995), show little scatter. In the last few years a great deal of observational work on galactic stars appeared: Fulbright (2000), Mashonkina & Gehren (2000, 2001), Koch & Edvardsson (2002), Honda et al. (2004), Ishimaru et al. (2004). All these works confirmed the presence of the spread for these elements. It is worth noting that this spread is not found for the [α/Fe] ratios in very metal poor stars (down to $[Fe/H] = -4.0$, Cayrel et al. 2004). This fact suggests that the spread, if real, is a characteristic of these heavy elements and not only due to an inhomogeneous mixing in the early halo phases, as suggested by several authors (Tsujimoto et al. 1999; Ishimaru & Wanajo 1999).

To have an insight on this peculiar behaviour of these elements, it is important to understand how they are formed. The neutron capture is the main mechanism which forms elements heavier than iron; the other mechanism, the p-process, is required for proton-rich isotopes, whose abundances in the solar system is less than 1%. Two major neutron capture mechanisms are generally invoked: the slow process (s-process) and the rapid process(r-process), where the slow and rapid are defined relative to the timescale of β-decay.

The s-process requires a relatively low neutron density and moves along the valley of β stability. The s-process feeds in particular the elements Sr-Y-Zr, Ba-La-Ce-Pr-Nd and Pb, the three major s-peaks. The reason for the existence of these peaks is that: the neutron capture process imposes certain features on the "spectrum" of the heavy element abundances. For certain neutron numbers N = 50, 82, 126 the neutron capture cross-sections are much smaller than for neighbouring neutron numbers. This means that once one of these "magic" numbers is reached, it becomes significantly less likely for the nucleus to capture more neutrons. These numbers represent a quantum mechanical effect of closed shells, in precisely the same way that closed electron shells produce high chemical stability in the noble gases. Therefore, if the neutron capture process operates in some environment for some finite length of time and then shuts off, we expect a fair number of nuclei to be "stuck" at these "magic" numbers. Elements that correspond to these "magic" numbers of neutrons will thus be especially abundant. The relevant properties necessary for describing the s-process chain are the neutron capture cross section and, in addition, the β-decay rates of those unstable isotopes, which are long-lived enough to allow neutron captures to compete with the β-decay. Käppeler et al. (1989) have calculated the s-process abundances in the solar system, scaling the abundances for the all the

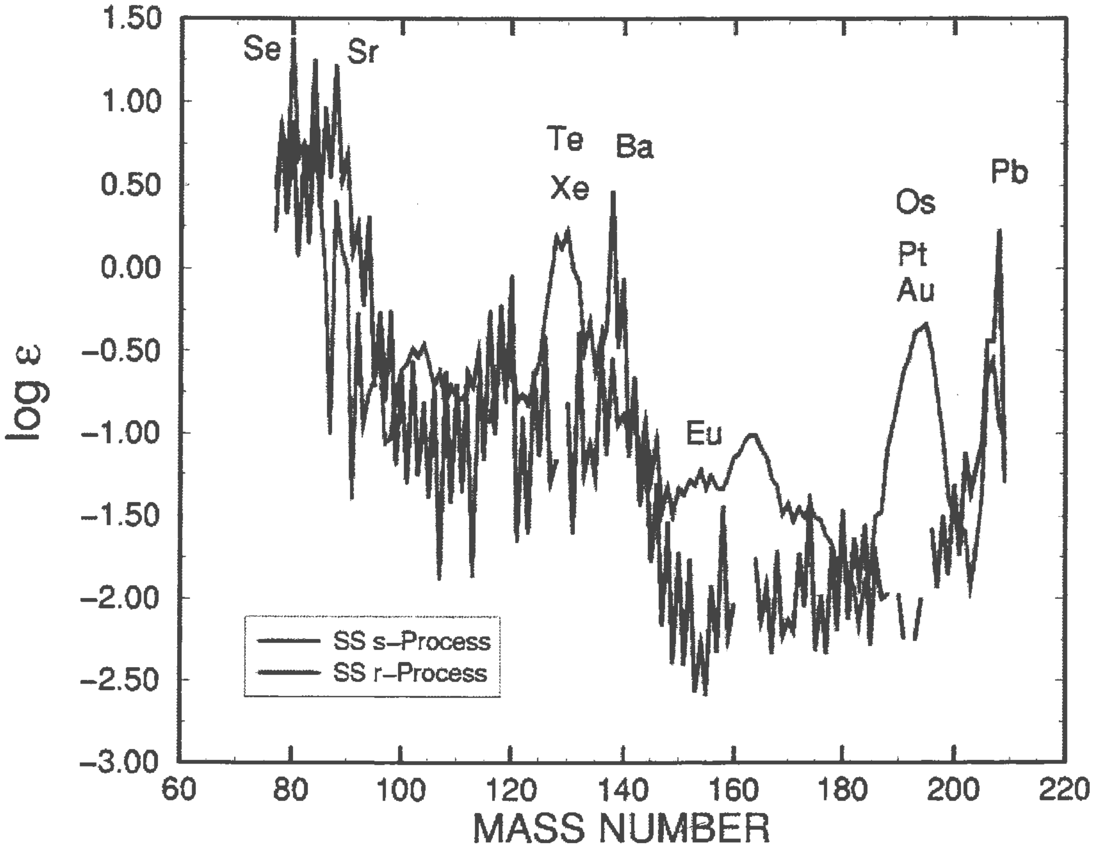

Figure 1.2. s-process (blue line) and r-process (red line) abundances in solar system matter, based upon the work by Kaÿpeler et al. (1989). Note the distinctive s-process signatures at masses ~ 138, and 208. The total solar system abundances for the heavy elements are those compiled by Anders & Grevesse (1989).

isotopes to the s-only isotope ^{150}Sm. They obtained their results by means of the classical analysis. The classical analysis is a phenomenological model and in first approximation any time dependence of the physical parameters is neglected. The classical s-process pattern is shown in Figure 1.2. The r-process pattern, also shown in the figure, is obtained by subtracting the predicted abundance of s-process fraction of each element to the solar system abundance of the same element. As we said, the classical analysis is a phenomenological model but nevertheless, more detailed considerations (see Käppeler et al. 1989) lead to a physical environment characteristic of helium shell-burning zones.

The site of production of the main component of the s-process, accounting for the s-process in the atomic mass number range $90 < A < 208$, was shown to occur in the low-mass (1.5-3.0

$M_\odot$) asymptotic giant branch (AGB) stars during recurrent thermal pulses by stellar models (Gallino et al. 1998; Busso et al. 1999). A dredge down of protons can occur during these thermal pulses , as first suggested by Iben and Renzini (1982a, b). These protons move from the hydrogen-rich envelope into the helium zone in low mass AGB stars, due to the operation of a semiconvective mixing. Subsequently, these protons are captured by ^{12}C in the carbon-rich layer forming a ^{13}C pocket. This pocket is then engulfed by the growing convective region of the next pulse, releasing neutrons via the $^{13}C(\alpha, n)^{16}O$ reaction. The s-process mechanism operating in the AGB model depends on the initial stellar metallicity. In fact, although the ^{13}C pocket, which acts as a neutron producer with the reaction $^{13}C(\alpha, n)^{16}O$, is of primary origin[3] in the work of Gallino et al. (1998) and Busso et al. (1999, 2001), the ensuing s-process production is dependent on the initial abundance of the Fe-group seeds, i.e. on the stellar metallicity. The neutron exposure (the neutron flux per nucleus seed) is roughly proportional to the number of available neutron sources (the ^{13}C nuclei) per seed (the iron nuclei), hence inversely proportional to the stellar metallicity. The strong s-component introduced by Clayton & Rassbach (1967) in order to reproduce more than 50% of solar ^{208}Pb, is not necessary in the these stellar models, being naturally obtained in very metal poor stars by metallicity effects, where the iron seeds are very rare. Moreover this scenario provide to feed also chemical elements in the mass number $\sim$ 90 such Sr, Y and Zr. The $^{22}Ne(\alpha, n)^{25}Mg$ reaction plays also a marginal role in the production of neutron capture elements in low mass ABG stars. In fact, this reaction is triggered when the temperature T exceeds $3 \cdot 10^8$ K and in low mass stars the maximum temperature at the bottom of thermal pulses, although gradually increasing with the pulse number, barely reaches the mentioned value.

The weak s-component is responsible for the s-process nuclides up to $A \simeq 90$ and it is recognized as the result of neutron capture during the helium burning core of massive stars. In this environment, the $^{22}Ne(\alpha, n)^{25}Mg$ neutron producer reaction can operate and first studies by Peters (1968) and Lamb et al. (1977) suggested that the lightest s-process nuclei can be provided by this source. Recent studies (Raiteri et al. 1992, Baraffe et al. 1992) discovered a decrease of the production at low metallicity. In fact, the elevated levels of

---

[3] We define a primary element an element synthesized from the original H and He, independently of metals. On the other hand, a secondary element is an element which is produced proportionally to the abundance of metals already present in the stars and not made in situ.

nuclei from Ne to Ca in the He-burning core of a massive star prevent the neutrons to be captured by the relative rare iron seeds. For these reasons, the solar system contribution from weak s-process is less than 10% for Sr and negligible for Y and Zr (Travaglio et al. 2004).

The r-process takes place in extremely neutron-rich environments in which the mean time between two successive neutron captures is very short, compared with the time necessary for the β-decay. For some time (cfr. Truran et al. 1981, Mathews & Cowan 1990) the similar abundance distributions for Z>56 elements in metal deficient stars have been interpreted as evidence for a universal r-process abundance distribution in the early Galaxy. In particular, more recent observations (Sneden et al. 2002, 1998, 2000; Johnson & Bolte 2001) all seem to confirm this feature, that is generally referred as the "universality" of r-process. Hence, it is generally believed that, at least for Z>56 elements, the astrophysical site and associated yields of r-process nucleosynthesis are unique.

There are, however, some reasons to question the assumption of a universal r-process abundance curve. The material out of which these metal poor stars were formed is likely to have experienced the enrichment by only one or two supernovae before incorporation into the stars. Depending upon which particular progenitor supernova was involved, there might be substantially different abundance distribution curves for these stars, compared to the one represented in Solar-System material, which is a average on many episodes of chemical enrichment (Ishimaru & Wanajo 1999). Recent work by Otsuki et al. (2003) indicates that the coincidence of the observed abundance distribution for $56 < Z < 75$ elements with the Solar r-process abundances does not necessarily mean that all r-process events occur in the same universal environment. Moreover, different abundance distributions for $Z > 75$ and $Z < 56$ elements are produced even when the universal $56 < Z < 75$ abundances are reproduced. Several scenarios have been proposed for the origin of r-process elements: neutrino winds in core-collapse supernovae (Woosley et al. 1994), the collapse of ONeMg cores resulting from stars with initial masses in the range 8-10$M_{\odot}$ (Wanajo et al. 2003) and neutron star mergers (Freiburghaus et al. 1999), even if this last scenario seems to be ruled out from the recent work of Argast et al. (2004) at least as the major one responsible for r-process enrichment in our Galaxy. So if the r-process is generally accepted to take place in SNe II explosions (Hill et al. 2002; Cowan et al. 2002), no clear consensus has been achieved and r-process nucleosynthesis still remains uncertain. Theoretical predictions for r-process production still do not exist, with the exception of the results of Wanajo et al. (2003) and

Woosley and Hoffmann (1992). However, the results of the model of Wanajo et al. cannot be used in galactic chemical evolution models because they do not take into account fallback (after the SN explosion some material can fall back onto central collapsing neutron star) and so the amount of neutron capture elements produced is probably too high (about 2 orders of magnitude higher than the chemical evolution predictions). Furthermore, Woosley and Hoffmann (1992) have given prescriptions for r-processes only until ^{107}Ru. In order to shed light on the nature (s- and/or r- processes) of heavy elements such as Ba and Eu one should examine the abundances of these elements in Galactic stars of all metallicities. These abundances can give us clues to interpret their nucleosynthetic origin when compared with detailed chemical evolution models.

1.3 Chemical evolution of s- and r-process elements

Previous studies of the evolution of the abundances of s- and r-process elements in the Galaxy are from Wheeler, Sneden & Truran (1989), Mathews et al. (1992), Pagel & Tautvaisiene (1997), Travaglio et al. (1999). In the Mathews et al. (1992) paper it was suggested that the observed apparent decrease of the abundance of Eu for [Fe/H] < -2.5 could be due to the fact that Eu originates mainly in low mass core-collapse SNe (7-8 $M_{\odot}$). Wheeler, Sneden & Truran (1989) and Pagel & Tautvaisiene (1997) suggested that to reproduce the observed behaviour of Ba it is necessary to assume that at early stages Ba is produced as an r-process element by a not well identified range of massive stars. A similar conclusion was reached by Travaglio et al. (1999) who showed that the evolution of Ba cannot be explained by assuming that this element is only an s-process element mainly formed in stars with initial masses 2-4$M_{\odot}$, but an r-process origin for it should be considered. In fact, in the hypothesis of a production of Ba only by s-process, a very late appearance of Ba should be expected, at variance with the observations indicating that Ba is already produced at [Fe/H]=-4.0. They suggested that low mass SNII (from 8 to 10$M_{\odot}$) could be responsible for the r-component of Ba. Travaglio et al. (2004) compared their theoretical predictions with the abundance pattern observed in the very r-process rich star CS 22892052 (Sneden et al. 2003). They considered this star as having a pure r-process signature. They extracted from this star the r-fraction of Sr, Y, and Zr (10% of the solar value). In the light of their nucleosynthesis calculations in AGB stars at different metallicities, they concluded that the s-process from AGB stars contributes to the solar abundances of Sr, Y, and Zr by 71%, 69%, and 65%, respectively. Concerning the solar Sr abundance, they also added a small contribution (10%) from the weak s-component from massive stars. As a consequence of the above results, they concluded that a primary component from massive stars is needed to explain 8% of the solar abundance of Sr and 18% of solar Y and Zr. This process is of primary nature, unrelated to the classical metallicity-dependent weak s-component. As already said, another important aspect of the [Ba/Fe] and [Eu/Fe] vs [Fe/H] relations is the observed spread. An attempt to explain the observed spread in s- and r-elements can be found in Tsujimoto et al. (1999) and Ishimaru & Wanajo (1999), who claim an inefficient mixing in the early galactic phases and attribute the spread to the fact that we observe the pollution due to single supernovae. Ishimaru & Wanajo (1999) also concluded that the Eu should originate as an r-process element in stars with masses in the range 8-10$M_{\odot}$. This latter suggestion was confirmed by Ishimaru et al. (2004) by comparing model predictions with new data from Subaru indicating subsolar [Eu/Fe] ratios in three very metal poor stars ([Fe/H]< -3.0).

Recently, several studies have attempted to follow the enrichment history of the Galactic halo with special emphasis given to the gas dynamical processes occurring in the early Galaxy: Tsujimoto, Shigeyama, & Yoshii (1999) provided an explanation for the spread of Eu observed in the oldest halo stars in the context of a model of supernova-induced star formation; Ikuta & Arimoto (1999) and McWilliam & Searle (1999) studied the metal enrichment of the Galactic halo with the help of a stochastic model aimed at reproducing the observed Sr abundances; Raiteri et al. (1999) followed the Galactic evolution of Ba by means of a hydrodynamical N-body/SPH code; Argast et al. (2000) concentrated on the effects of local inhomogeneities in the Galactic halo produced by individual supernova events, accounting in this way for the observed scatter of some (but not all) elements typically produced by type II SNe. They predicted, however, a too large spread for Mg and other α-elements which is not observed. Finally, Travaglio et al. (2004) investigated whether incomplete mixing of the gas in the Galactic halo can lead to local chemical inhomogeneities in the ISM of the heavy elements, in particular Eu, Ba, and Sr. However what has still to be explained is why the spread is present only for neutron capture elements whereas it is very small for the other elements (for example α-elements).

Other important constraints, which are connected to the evolution of the Galaxy disk, are the abundance gradients of the elements along the disk of the Milky Way. Abundance gradients are a feature commonly observed in many galaxies with their metallicities decreasing outward from the galactic centers. The study of the gradients provides strong constraints to the mechanism of galaxy formation; in fact, star formation and the accretion history as function of galactocentric distance in the galactic disk strongly influence the formation and the development of the abundance gradients (see Matteucci & François 1989, Boisser & Prantzos 1999, Chiappini et al. 2001). Many models have been computed to explain the behaviour of abundances and abundance ratios as functions of galactocentric radius (e.g Hou et al. 2000; Chang et al. 1999; Chiappini et al. 2003b; Alibés et al. 2001) but they restrict their predictions to a small number of chemical elements and do not consider very heavy elements.

1.4 S- and r-process elements in dwarf spheroidal galaxies

The proximity and the relative simplicity of the Local Group (LG) dwarf spheroidal (dSph) galaxies make these systems excellent laboratories to test assumptions regarding the nucleosynthesis of chemical elements and theories of galaxy evolution. The Local Group is the group of galaxies that includes the Milky Way. The group comprises about 40 galaxies, with its gravitational center located between the Milky Way and the Andromeda Galaxy (see Fig. 1.3). At the present time, the Milky Way has 12 identified dwarf spheroidal (dSph) galaxy companions and three of them have been discovered very recently (see table 1.1). DSph galaxies can be defined as a low luminosity ($M_V >$ -14), non-nucleated dwarf elliptical galaxy with low surface brightness. Several studies addressing the observation of red giant stars in these dSph galaxies with high resolution spectroscopy allow one to infer accurately the abundances of several elements including α-, iron-peak and very heavy elements, such as barium and europium (Smecker-Hane & McWilliam 1999; Bonifacio et al. 2000; Shetrone, Coté & Sargent 2001; Shetrone et al. 2003; Bonifacio et al. 2004; Sadakane et al. 2004; Geisler et al. 2005). These abundances and abundance ratios are not only central ingredients in galactic chemical evolution studies but are also very important in the attempt to clarify some aspects of the processes responsible for the formation of chemical elements. Shetrone, Coté & Sargent (2001) argued that Draco (see Fig 1.4) and Ursa Minor (see Fig. 1.5) stars exhibit an abundance pattern consistent with one dominated by the r-process, i.e. [Ba/Eu] ranges from solar values at high metallicities to [Ba/Eu] $\sim$ -0.5 at [Fe/H] $\leq$ -1 dex. The pat-

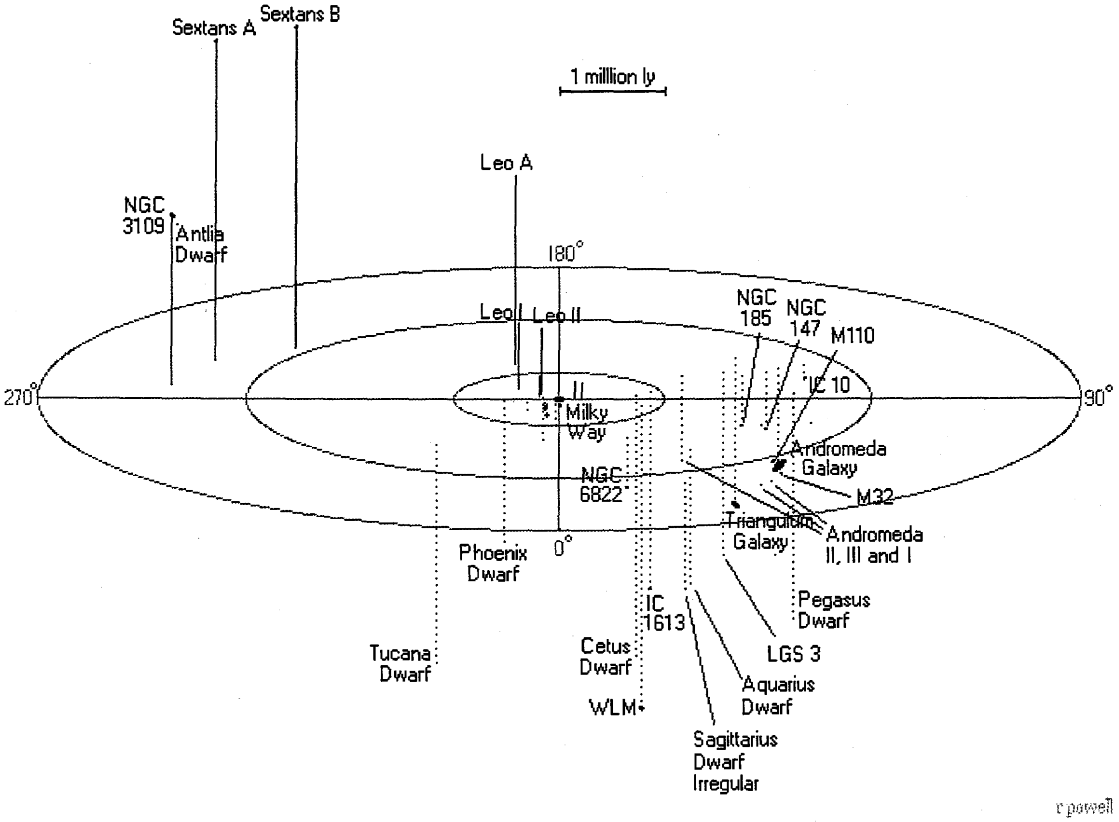

Figure 1.3. The map of the Local Group.The Milky Way is one of three large galaxies belonging to the group of galaxies called the Local Group which also contains several dozen dwarf galaxies. Most of these galaxies are depicted on the map.

Table 1.1. The dSph galaxies of the Milky Way and their characteristic

Name	distance (kpc)	Visual luminosity $L(V)/10^6 M_\odot$	Absolute Visual Magnitude	Total virial mass $M/10^6 M_\odot$	[Fe/H]	Year
Sagittarius	24 ±2	18.1	-13.4	–	-1.0±0.2	1994
Bootes	60 ±?	–	-5.7	–	–	2006
Ursa Minor	66 ±3	0.3	-8.9	23	-2.2±0.1	1954
Sculptor	79 ±4	2.2	-11.1	6	-1.8±0.1	1938
Draco	82 ±6	0.3	-8.8	22	-2.0±0.1	1954
Sextans	86 ±4	0.5	-9.5	19	-1.7±0.2	1990
Ursa Major	100 ±?	–	-6.8	–	–	2005
Carina	101 ±5	0.4	-9.3	13	-2.0±0.2	1977
Fornax	138 ±8	15.5	-13.2	68	-1.3±0.2	1938
Leo II	205 ±12	0.6	-9.6	10	-1.9±0.1	1950
Canes Venatici	220 ±?	–	-7.9	–	–	2006
Leo I	250 ±30	4.8	-11.9	22	-1.5±0.4	1950

tern of [Ba/Fe] and [Eu/Fe] also resembles the one observed in the halo field stars according to these authors. The same conclusion was reached by Shetrone et al. (2003), who analysed these abundance ratios in Sculptor, Fornax and Carina. Shetrone et al. (2003) claimed also that in Sculptor, Fornax and LeoI the pattern of [Eu/Fe] is consistent with the production of Eu in SNe II. On the other hand, Venn et al. (2004), pointed out that, despite the general similarity, the dSph stars span a larger range in [Ba/Fe] and [Eu/Fe] ratios at intermediate metallicities than the Galactic stars and, more important, that about half of the dSph stars exhibit lower [Y/Eu] and 2/3 higher [Ba/Y] than the Galactic stars at the same metallicity, thus suggesting a clear difference between the chemical evolution of our Galaxy and the one of dSph galaxies. The [α/Fe] ratios observed in dSphs also are different from the same ratios in the Milky Way showing in general lower [α/Fe] ratios than the Galactic stars with the same [Fe/H] (Smecker-Hane & McWilliam 1999; Bonifacio et al. 2000; Shetrone, Coté & Sargent 2001; Shetrone et al. 2003; Bonifacio et al. 2004; Sadakane et al. 2004; Geisler et al.

Figure 1.4. The dSph galaxy Draco.

2005).

These observations not only shed some light on the chemical evolution history of these galaxies but allowed also the construction of chemical evolution models aimed at reproducing important observational constraints, such as the elemental abundance ratios, the present gas mass and total mass (Carraro et al. 2001; Carigi, Hernandez & Gilmore 2002; Ikuta & Arimoto 2002; Lanfranchi & Matteucci 2003 (LM03); Lanfranchi & Matteucci 2004 (LM04)).

Among these models the one proposed by LM03 and LM04 for 5 local dSph galaxies (namely Draco, Carina, Sculptor, Ursa Minor and Sagittarius) succeeded in reproducing the observed [α/Fe] ratios, the present gas mass and final total mass by adopting a very low star formation rates proceedings in relatively long bursts as indicated by the color-magnitude diagrams of these galaxies.

This thesis is organized as follows:

Figure 1.5. The dSph galaxy Ursa minor.

in chapter 2, we present the results of a chemical evolution model based on the model developed by Chiappini et al. (2003a) for the Milky Way; we compare our theoretical results relative to the evolution of neutron capture elements (Sr, Y, Zr, Ba, La and Eu) with the newest data of François et al. (2006) and we impose constraints on the nucleosynthesis of the studied elements.

In chapter 3, we calculate the abundance gradients of the largest number of heavy elements (O, Mg, Si, S, Ca, Sc, Ti, Co, V, Fe, Ni, Zn, Cu, Mn, Cr, Sr, Y, Zr, Ba, La and Eu) ever considered in a chemical evolution model; therefore, we are able to test nucleosynthesis prescriptions obtained in the previous chapter as well as the recent nucleosynthesis by François et al. (2004) for the α- and iron peak elements. Chemical evolution models adopting the above nucleosynthesis prescriptions have been shown to reproduce the evolution of the abundances in the solar neighborhood. Here we extend our predictions to the whole disk and we compare our model predictions to new observational data collected by Andrievsky et al. (2002abc, 2004) and Luck et al. (2003) (hereafter 4AL). They measured the abundances of all the selected elements (except Ba) in a sample of 130 galactic Cepheids found in the galactocentric distance range from 5 to 17 kpc.

In chapter 4, we show the results of a stochastic chemical evolution model that we develop with the same nucleosynthesis of the models of the previous chapters. We test if this model is able to reproduce the large spread of the abundances of neutron capture elements observed in low metallicity stars in the solar vicinity and, at the same time, the small star to star scatter observed for the α-elements.

In chapter 5, we adopt the nucleosynthesis prescriptions for Ba and Eu which are able to reproduce the most recent observed data for our Galaxy, as shown in chapter 2, and we compare the predictions of the models with observational data in 5 dSph galaxies. In this way, it is possible to verify if the assumptions made regarding the nucleosynthesis of Ba and Eu can also fit also the data of local dSph galaxies.

In chapter 6, we use the results of chapter 2 and chapter 5, to compare the predictions of the Milky Way to those of the dSph galaxies. We choose, as typical dwarf spheroidal galaxy, Sculptor. We do not show all the data for all the dwarf spheroidal galaxies because as will be shown in chapter 5, the star formation histories are different and also the chemical evolution is different among the dSph galxies, even if they share common behaviors.

Finally, in chapter 7, the main conclusions of our work are drawn.

Chapter 2

Chemical evolution of neutron capture elements in the solar vicinity

“"Man," I cried, "how ignorant art thou in thy pride of wisdom!”
by Mary Shelley

2.1 Barium and europium

We present the results of a chemical evolution model based on the original two-infall model of Chiappini et al. (1997) for the Milky Way in the latest version developed by Chiappini et al. (2003a) and adopted in François et al. (2004). We compare our theoretical results relative to the evolution of Ba and Eu with the newest and very accurate data of François et al. (2007) and we impose constraints on the nucleosynthesis of the studied elements.

2.1.1 Observational data

We preferentially used the most recent available data based on high quality spectra collected with efficient spectrographs and 8-10 m class telescopes. In particular, for the extremely metal poor stars ([Fe/H] between -4 and -3), we adopted the recent results from UVES Large Program "First Star" (Cayrel et al. 2004, François et al. 2007). This sample consists of 31 extremely metal-poor halo stars selected in the HK survey (Beers et al. 1992, 1999). We can deduce from the kinematics of these stars that they were born at very different places in the Galactic halo. This overcomes the possibility of a selection bias. The analysis is made in a systematic and homogeneous way, from very high quality data, giving abundance ratios of unprecedented accuracy in this metallicity range. For the abundances in the remaining range of [Fe/H], we took published high quality data in the literature from various sources: Burris et al. (2000), Fulbright (2000), Mashonkina & Gehren (2000, 2001), Koch & Edvardsson (2002), Honda et al. (2004), Ishimaru et al. (2004). All of these data are relative to solar abundances of Grevesse & Sauval (1998).

2.1.2 Chemical evolution model for the solar vicinity

We model the formation of the Galaxy assuming two main infall episodes: the first forms the halo and the thick disk, the second the thin disk. The timescale for the formation of the halo-thick disk is $\sim 1Gyr$. The timescale for the thin disk is much longer, implying that the infalling gas forming the thin disk comes mainly from the intergalactic medium and not only from the halo (Chiappini et al. 1997). Moreover, the formation of the thin disk is assumed to be a function of the galactocentric distance, leading to an inside out scenario for the Galaxy disk build up (Matteucci & François 1989). In this chapter, all the results shown are for the assumed solar galactocentric distance: 8 kpc. The main characteristic of the two-infall model is an almost independent evolution between the halo and the thin disk (see also Pagel & Tautvaisiene 1995). A threshold in the star formation process (Kennicutt 1989, 1998, Martin & Kennicutt 2001) is also adopted. The model well reproduces an extended set of observational constraints both for the solar neighborhood and for the whole disc. One of the most important observational constraints is represented by the various relations between the abundances of metals (C,N,O,α-elements, iron peak elements) as functions of the [Fe/H] abundance (see Chiappini et al. 2003) Although this model is probably not unique, it reproduces the majority of the observed features of the Milky Way. Many of the assumptions of the model are shared by other authors (e.g. Prantzos & Boissier 2000, Alibés et al. 2001, Chang et al. 1999). The equation below describes the time evolution of G_i, namely the mass fraction of the element i in the gas:

$$\dot{G}_i(t) = -\psi(r,t)X_i(r,t)$$

$$+\int_{M_L}^{M_{Bm}} \psi(t-\tau_m)Q_{mi}(t-\tau_m)\phi(m)dm$$

$$+A\int_{M_{Bm}}^{M_{BM}} \phi(M_B)\cdot\left[\int_{\mu_m}^{0.5} f(\mu)\psi(t-\tau_{m2})Q_{mi}^{SNIa}(t-\tau_{m2})d\mu\right]dM_B$$

$$+(1-A)\int_{M_{Bm}}^{M_{BM}} \psi(t-\tau_m)Q_{mi}(t-\tau_m)\phi(m)dm$$

$$+\int_{M_{BM}}^{M_U} \psi(t-\tau_m)Q_{mi}(t-\tau_m)\phi(m)dm$$

$$+X_{A_i}A(r,t). \tag{2.1}$$

where $X_i(r,t)$ is the abundance by mass of the element i and Q_{mi} indicates the fraction of mass restored by a star of mass m in the form of the element i, the so-called "production matrix" as originally defined by Talbot and Arnett (1973). We indicate with M_L the lightest mass that contributes to the chemical enrichment and it is set at $0.8M_\odot$; the upper mass limit, M_U, is set at $100M_\odot$.

The star formation rate (SFR) $\psi(r,t)$ is defined:

$$\psi(r,t) = \nu\left(\frac{\Sigma(r,t)}{\Sigma(r_\odot,t)}\right)^{2(k-1)}\left(\frac{\Sigma(r,t_{Gal})}{\Sigma(r,t)}\right)^{k-1} G_{gas}^k(r,t). \tag{2.2}$$

ν is the efficiency of the star formation process and is set to be $2Gyr^{-1}$ for the Galactic halo ($t < 1Gyr$) and $1Gyr^{-1}$ for the disk ($t \geq 1Gyr$). $\Sigma(r,t)$ is the total surface mass density, $\Sigma(r_\odot,t)$ the total surface mass density at the solar position, $G_{gas}(r,t)$ the surface density normalized to the present time total surface mass density in the disk $\Sigma_D(r,t_{Gal})$, where $t_{Gal} = 14Gyr$ is the age assumed for the Milky Way and $r_\odot = 8$ kpc the solar galactocentric distance (Reid 1993). The gas surface exponent, k, is set equal to 1.5. With these values for the parameters the observational constraints, in particular in the solar vicinity, are well fitted. Below a critical threshold of the gas surface density ($7M_\odot pc^{-2}$) we assume no star formation. This naturally produces a hiatus in the SFR between the halo-thick disk phase and the thin disk phase. In Fig. (2.1) we show the predicted star formation rate for the halo-thick disc phase and the thin disc phase, respectively.

For ϕ, the initial mass function (IMF), we use the Scalo (1986) one, constant in time and space, while τ_m is the evolutionary lifetime of stars as a function of their mass "m".

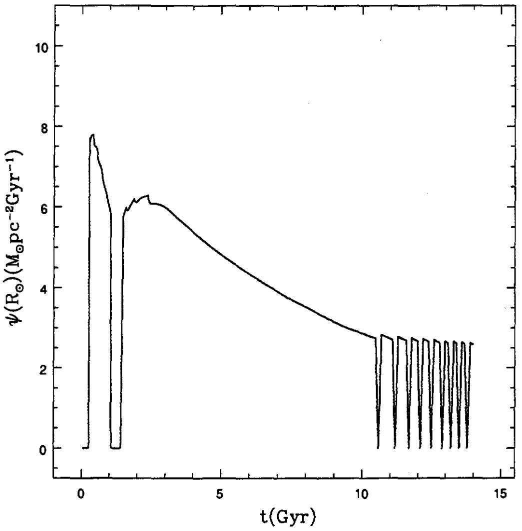

Figure 2.1. The SFR expressed in $M_\odot pc^{-2} Gyr^{-1}$ as predicted by the two infall model. The gap in the SFR at the end of the halo-thick disc phase is evident. The oscillations are due to the fact that at late times in the galactic disc the surface gas density is always close to the threshold density.

The SNIa rate has been computed following Greggio & Renzini (1983a) and Matteucci & Greggio (1986) and it is expressed as:

$$R_{SNeIa} = A \int_{M_{Bm}}^{M_{BM}} \phi(M_B)\left(\int_{\mu_m}^{0.5} f(\mu)\psi(t - \tau_{M_2})d\mu\right)dM_B. \tag{2.3}$$

where M_2 is the mass of the secondary, M_B is the total mass of the binary system, $\mu = M_2/M_B$, $\mu_m = max\,[M(t)_2/M_B, (M_B - 0.5M_{BM})/M_B]$, $M_{Bm} = 3M_\odot$, $M_{BM} = 16M_\odot$. The IMF is represented by $\phi(M_B)$ and refers to the total mass of the binary system for the computation of the SNeIa rate, $f(\mu)$ is the distribution function for the mass fraction of the secondary:

$$f(\mu) = 2^{1+\gamma}(1+\gamma)\mu^\gamma. \tag{2.4}$$

with $\gamma = 2$; A is the fraction of systems in the appropriate mass range that can give rise to SNeIa events. This quantity is fixed to 0.05 by reproducing the observed SNeIa rate at the present time (Cappellaro et al. 1999). Note that in the case of SNIa the"production matrix" is indicated by Q_{mi}^{SNIa} because of its different nucleosynthesis contribution (for details see Matteucci and Greggio 1986). In Fig. 2.2 we show the predicted type II and Ia SN rates. The type II SN rate follows the SFR, as expected, whereas the type Ia SN rate does not have this feature due to the nature of type Ia SN progenitors, which are assumed to be low-intermediate mass stars with long evolutionary time scales.

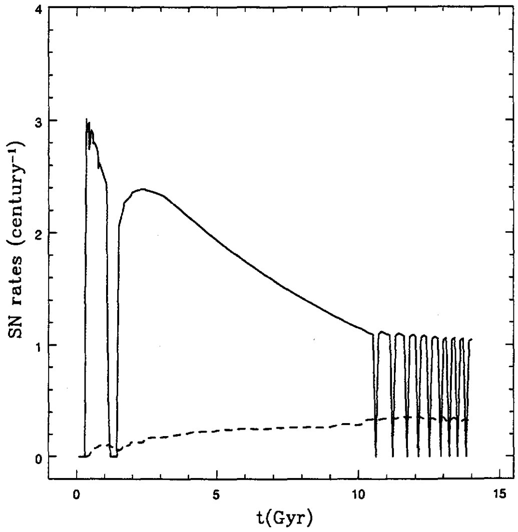

Figure 2.2. Predicted SN II (continuous line) and Ia (dashed line) rates by the two infall model.

The last term in equation 1 represents the gas accretion and it is defined as:

$$A(r,t) = a(r)e^{-t/\tau_H} + b(r)e^{(t-t_{max})/\tau_D(r)}. \tag{2.5}$$

where X_{A_i} are the abundances of the infalling material, assumed to have a primordial chemical composition , $t_{max} = 1Gyr$ is the time for the maximum infall rate on the thin disk, $\tau_H = 2.0Gyr$ is the time scale for the formation of the halo thick-disk and τ_D is the timescale of the thin disk at the solar galactocentric distance ($\tau_D = 7Gyr$). The timescale τ_D increases with the galactocentric distance as we will see in chapter 3. The coefficients $a(r)$ and $b(r)$ are constrained by the present day total surface mass density. In particular, $b(r)$ is assumed to be different from zero for $t > t_{max}$ (see Chiappini et al. 2003, for details).

2.1.3 Nucleosynthesis prescriptions for Ba and Eu

S-process

We have adopted the yields of Busso et al. (2001) in the mass range 1.5-3$M_\odot$ for the s-main component. In this process, the dependence on the metallicity is very important. The s-process elements are made by accretion of neutrons on seed elements (in particular iron) already present in the star. Therefore, this Ba component behaves like a secondary element. The neutron flux is due to the reaction $^{13}C(\alpha, n)^{16}O$ which can easily be activated at the low temperature of these stars (see Busso et al. 1999). The yields are shown in Table 2.1 and Fig. 2.3 as functions of the initial metallicity of the stars. The theoretical results by Busso et al. (2001) suggest negligible europium production in the s-process and therefore we neglected this component in our work. We have added for models 1 and 2 (see Table 2.2) an extension to the theoretical result of Busso et al. (2001) in the mass range $1 - 1.5M_{\odot}$ by simply scaling with the mass the values obtained for stars of $1.5M_{\odot}$. We have extended the prescription in order to better fit the data with a [Fe/H] supersolar and verified that it does not change the results of the model for $[Fe/H] < 0$.

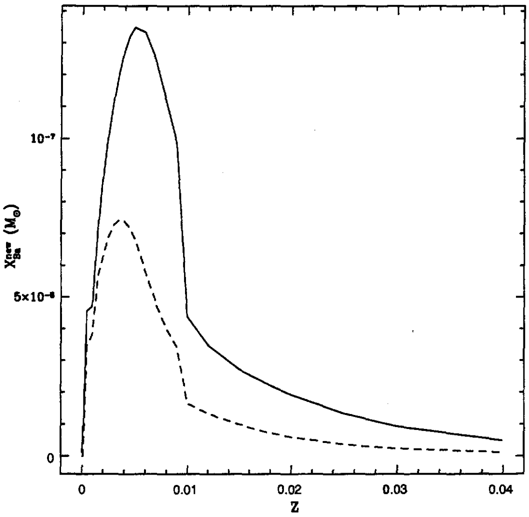

Figure 2.3. The stellar yields X_{Ba}^{new} from Busso et al. (2001) plotted versus metallicity. Dashed line: the prescriptions for stars of $1.5M_{\odot}$, solid line for stars of $3M_{\odot}$.

R-process

The production of r-process elements is still a challenge for astrophysics and even for nuclear physics, due to the fact that the nuclear properties of thousands of nuclei located between the valley of β stability and the neutron drip line, necessary to correctly compute this process, are ignored. In our models we have tested 6 different nucleosynthesis prescriptions for the r-process Ba and Eu, as shown in Tables 2.2, 2.3 and 2.4. Some of the prescriptions refer

Table 2.1. The stellar yields in the range $1.5 - 3M_\odot$ from the paper of Busso et al. (2001).

Metallicity	X_{Ba}^{new} for $1.5M_\odot$	X_{Ba}^{new} for $3M_\odot$
$0.20 \cdot 10^{-3}$	$0.69 \cdot 10^{-8}$	$0.13 \cdot 10^{-7}$
$0.10 \cdot 10^{-2}$	$0.38 \cdot 10^{-7}$	$0.46 \cdot 10^{-7}$
$0.20 \cdot 10^{-2}$	$0.63 \cdot 10^{-7}$	$0.87 \cdot 10^{-7}$
$0.30 \cdot 10^{-2}$	$0.72 \cdot 10^{-7}$	$0.11 \cdot 10^{-6}$
$0.40 \cdot 10^{-2}$	$0.73 \cdot 10^{-7}$	$0.12 \cdot 10^{-6}$
$0.50 \cdot 10^{-2}$	$0.68 \cdot 10^{-7}$	$0.13 \cdot 10^{-6}$
$0.60 \cdot 10^{-2}$	$0.58 \cdot 10^{-7}$	$0.13 \cdot 10^{-6}$
$0.70 \cdot 10^{-2}$	$0.47 \cdot 10^{-7}$	$0.12 \cdot 10^{-6}$
$0.80 \cdot 10^{-2}$	$0.39 \cdot 10^{-7}$	$0.11 \cdot 10^{-6}$
$0.90 \cdot 10^{-2}$	$0.34 \cdot 10^{-7}$	$0.98 \cdot 10^{-7}$
$0.10 \cdot 10^{-1}$	$0.16 \cdot 10^{-7}$	$0.43 \cdot 10^{-7}$
$0.11 \cdot 10^{-1}$	$0.14 \cdot 10^{-7}$	$0.39 \cdot 10^{-7}$
$0.12 \cdot 10^{-1}$	$0.13 \cdot 10^{-7}$	$0.34 \cdot 10^{-7}$
$0.13 \cdot 10^{-1}$	$0.12 \cdot 10^{-7}$	$0.32 \cdot 10^{-7}$
$0.14 \cdot 10^{-1}$	$0.11 \cdot 10^{-7}$	$0.29 \cdot 10^{-7}$
$0.15 \cdot 10^{-1}$	$0.99 \cdot 10^{-8}$	$0.27 \cdot 10^{-7}$
$0.16 \cdot 10^{-1}$	$0.90 \cdot 10^{-8}$	$0.25 \cdot 10^{-7}$
$0.17 \cdot 10^{-1}$	$0.81 \cdot 10^{-8}$	$0.23 \cdot 10^{-7}$
$0.18 \cdot 10^{-1}$	$0.73 \cdot 10^{-8}$	$0.22 \cdot 10^{-7}$
$0.19 \cdot 10^{-1}$	$0.66 \cdot 10^{-8}$	$0.20 \cdot 10^{-7}$
$0.20 \cdot 10^{-1}$	$0.59 \cdot 10^{-8}$	$0.19 \cdot 10^{-7}$
$0.30 \cdot 10^{-1}$	$0.24 \cdot 10^{-8}$	$0.94 \cdot 10^{-8}$
$0.40 \cdot 10^{-1}$	$0.12 \cdot 10^{-8}$	$0.50 \cdot 10^{-8}$

to models by Travaglio et al. (2001) (model 3) and Ishimaru et al. (2004) (models 4, 5 and 6), whereas the others contain yields chosen "ad hoc", namely in order to reproduce the observational data.

In the case of Ba we have included an r-process component, produced in massive stars in the range 12-30$M_\odot$ in model 1 and in the range 10-25$M_\odot$ in model 2. In Fig. 2.4 we show the lightest stellar mass dying as a function of the metallicity of the ISM ([Fe/H]) in our chemical evolution model; it is clear from this plot that it is impossible to explain the observed abundances of [Ba/Fe] in stars with $[Fe/H] < -2$ without the Ba component produced in massive stars. The first stars, which produce s-processed Ba (see Sect. 2.1.3), have a mass of $3M_\odot$ and they start to enrich the ISM only for $[Fe/H] \geq -2$.

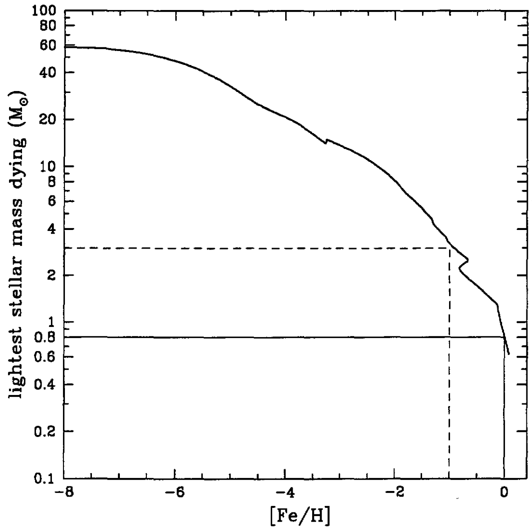

Figure 2.4. In the plot we show the lightest stellar mass dying at the time corresponding to a given [Fe/H]. The solid line indicates the solar abundance ([Fe/H]=0), corresponding to a lightest dying mass star of 0.8$M_\odot$, the dashed line indicates the [Fe/H]=-1 corresponding to a lightest dying star mass of 3$M_\odot$. The adopted stellar lifetimes are from Maeder & Meynet (1989).

We stress that Travaglio et al. (2001) predicted r-process Ba only from stars in the range 8-10$M_\odot$, but their conclusions were based on an older set of observational data.

Moreover, we considered another independent indication for the r-process production of barium; Mazzali and Chugai (1995) observed Ba lines in SN 1987A, which had a progenitor star of 20$M_\odot$. These lines of Ba are well reproduced with a overabundance factor

Table 2.2. Model parameters. The yields X_{Ba}^{new} are expressed as mass fractions. The subscript "ext" stands for extended (the yields have been extrapolated down to $1M_{\odot}$) and M_* for the mass of the star.

Mod	s-process Ba	r-process Ba	s-process Eu	r-process Eu
1	$1. - 3M_{\odot}$ Busso et al. (2001)ext.	$12 - 30M_{\odot}$ yields Table 2.3	none	$12 - 30M_{\odot}$ yields Table 2.3
2	$1. - 3M_{\odot}$ Busso et al. (2001)ext.	$10 - 25M_{\odot}$ yields Table 2.4	none	$10 - 25M_{\odot}$ yields Table 2.4
3	$1.5 - 3M_{\odot}$ Busso et al. (2001)	$8 - 10M_{\odot}$ $X_{Ba}^{new} = 5.7 \cdot 10^{-6}/M_*$ (Travaglio et al. 2001)	none	$12 - 30M_{\odot}$ yields Table 2.3
4	$1.5 - 3M_{\odot}$ Busso et al. (2001)	$10 - 30M_{\odot}$ yields Table 2.3	none	$8 - 10M_{\odot}$ $X_{Eu}^{new} = 3.1 \cdot 10^{-7}/M_*$ (Ishimaru et al.2004 Mod.A)
5	$1.5 - 3M_{\odot}$ Busso et al. (2001)	$10 - 30M_{\odot}$ yields Table 2.3	none	$20 - 25M_{\odot}$ $X_{Eu}^{new} = 1.1 \cdot 10^{-6}/M_*$ (Ishimaru et al.2004 Mod.B)
6	$1.5 - 3M_{\odot}$ Busso et al. (2001)	$10 - 30M_{\odot}$ yields Table 2.3	none	$> 30M_{\odot}$ $X_{Eu}^{new} = 7.8 \cdot 10^{-7}/M_*$ (Ishimaru et al.2004 Mod.C)

Table 2.3. The stellar yields for barium and europium in massive stars (r-process) in the case of a primary origin.

M_{star}	X_{Ba}^{new}	X_{Eu}^{new}
12.	$9.00 \cdot 10^{-7}$	$4.50 \cdot 10^{-8}$
15.	$3.00 \cdot 10^{-8}$	$3.00 \cdot 10^{-9}$
30.	$1.00 \cdot 10^{-9}$	$5.00 \cdot 10^{-10}$

Table 2.4. The stellar yields for Ba and Eu in massive stars (r-process) in the case of secondary origin. The mass fraction does not change as a function of the stellar mass.

Z_{star}	X_{Ba}^{new}	X_{Eu}^{new}
	$10-25M_{\odot}$	$10-25M_{\odot}$
$Z < 5 \cdot 10^{-7}$.	$1.00{\cdot}10^{-8}$	$5.00{\cdot}10^{-10}$
$5 \cdot 10^{-7} < Z < 1 \cdot 10^{-5}$	$1.00{\cdot}10^{-6}$	$5.00{\cdot}10^{-8}$
$Z > 1 \cdot 10^{-5}$	$1.60{\cdot}10^{-7}$	$8.00{\cdot}10^{-9}$

$f = X_{obs}/X_i = 5$ (typical metal abundance for LMC $X_i = (1/2.75)\times$ solar). From this observational data we can derive a $X_{Ba}^{new} \sim 2 \cdot 10^{-8}$for a 20 $M_{\odot}$ star, which is in agreement with our prescriptions.

For Eu we assumed that it is completely due to the r-process and that the yields originate from massive stars in the range 12-30$M_{\odot}$ in model 1 and 10-25$M_{\odot}$ in model 2, as shown in Table 2.2.

In particular, our choice is made to best fit the plots [Ba/Fe] vs.[Fe/H], [Eu/Fe] vs.[Fe/H] and [Ba/Eu] vs [Fe/H] as well as the Ba and Eu solar abundances (taking into account the contribution of the low-intermediate mass star in case of the Ba).

We have tested prescriptions for Ba and Eu both for a primary production and a secondary production (with a dependence on the metallicity). In the first case the main feature of the yields is a strong enhancement in the mass range $12 - 15M_{\odot}$ (model 1) with no dependence on the metallicity and so the elements are considered as primary elements. In the case of metallicity dependence (model 2), the yield behavior is chosen to have a strong enhancement in the range of metallicity $5 \cdot 10^{-7} < Z < 1 \cdot 10^{-5}$ with almost constant yields for Eu and Ba in the whole mass range for a given metallicity.

Iron

For the nucleosynthesis prescriptions of Fe, we adopted those suggested in François et al. (2004), in particular the yields of Woosley & Weaver (1995) (hereafter WW95) for a solar chemical composition. The yields for several elements suggested by François et al. (2004) are those best reproducing the observed [X/Fe] vs. [Fe/H] at all metallicities in the solar vicinity.

Table 2.5. Results after the computation of the mean for the data inside bins along the [Fe/H] axis for the values of [Ba/Fe].

bin center [Fe/H]	bin dim.[Fe/H]	mean [Ba/Fe]	SD [Ba/Fe]	N. of data in the bin
-3.82	0.75	-1.25	0.30	6
-3.32	0.25	-0.96	0.50	7
-3.07	0.25	-0.65	0.65	11
-2.82	0.25	-0.37	0.60	17
-2.57	0.25	-0.15	0.40	11
-2.32	0.25	0.09	0.58	13
-2.07	0.25	0.23	0.50	15
-1.82	0.25	0.10	0.20	20
-1.58	0.25	0.08	0.15	27
-1.33	0.25	0.20	0.22	16
-1.08	0.25	0.07	0.19	20
-0.83	0.25	-0.03	0.08	30
-0.58	0.25	-0.04	0.14	59
-0.33	0.25	0.05	0.20	46
-0.08	0.25	0.03	0.13	53
0.17	0.25	-0.01	0.11	26

2.1.4 Results

Trends

We investigate how the different models fit the the trends of the abundance ratios for [Ba/Fe], [Eu/Fe] and [Ba/Eu] versus [Fe/H] and even for [Ba/Eu] versus [Ba/H].

To better investigate the trends of the data we divide in several bins the [Fe/H] axis and the [Ba/H] axis and compute the mean and the standard deviation from the mean of the ratios [Ba/Fe], [Eu/Fe] and [Ba/Eu] for all the data inside each bin. In Table 2.5 we show the results of this computation for [Ba/Fe] versus [Fe/H], in Table 2.6 for [Eu/Fe] and [Ba/Eu] versus [Fe/H] and in Table 2.7 for [Ba/Eu] versus [Ba/H]. Since the ranges of [Ba/H] and

Table 2.6. Results after the computation of the mean for the data inside bins along the [Fe/H] axis for the values of [Eu/Fe] and [Ba/Eu].

bin center [Fe/H]	bin dim. [Fe/H]	mean [Eu/Fe]	SD [Eu/Fe]	mean [Ba/Eu]	SD [Ba/Eu]	N.of data in the bin
-3.22	0.24	-0.10	0.21	-0.71	0.25	5
-2.98	0.24	0.08	0.60	-0.57	0.13	12
-2.74	0.24	0.46	0.60	-0.64	0.11	14
-2.49	0.24	0.45	0.28	-0.52	0.17	7
-2.25	0.24	0.38	0.36	-0.38	0.33	11
-2.01	0.24	0.51	0.34	-0.36	0.26	10
-1.77	0.24	0.29	0.22	-0.20	0.19	19
-1.53	0.24	0.44	0.15	-0.39	0.22	21
-1.28	0.24	0.42	0.20	-0.26	0.31	18
-1.04	0.24	0.39	0.13	-0.38	0.15	16
-0.80	0.24	0.32	0.12	-0.35	0.14	36
-0.56	0.24	0.23	0.14	-0.27	0.20	55
-0.32	0.24	0.18	0.10	-0.13	0.23	44
-0.07	0.24	0.04	0.07	-0.02	0.14	51
0.17	0.24	-0.02	0.07	0.00	0.12	26

Table 2.7. Results after the computation of the mean for the data inside bins along the [Ba/H] axis for the values of [Ba/Eu].

bin center [Ba/H]	bin dim.[Ba/H]	mean [Ba/Eu]	SD [Ba/Eu]	N of data in the bin
-4.35	0.58	-0.75	0.26	4
-3.76	0.58	-0.60	0.14	12
-3.32	0.29	-0.55	0.14	3
-3.02	0.29	-0.62	0.13	4
-2.73	0.29	-0.58	0.24	13
-2.43	0.29	-0.58	0.21	4
-2.14	0.29	-0.44	0.13	7
-1.84	0.29	-0.33	0.28	20
-1.54	0.29	-0.33	0.20	25
-1.25	0.29	-0.39	0.19	21
-0.95	0.29	-0.31	0.20	36
-0.66	0.29	-0.33	0.18	64
-0.36	0.29	-0.13	0.14	43
-0.07	0.29	-0.03	0.09	68

[Fe/H] are different, we have bins of different width. We have divided in a different way the [Fe/H] for [Ba/Fe] ratio and the [Fe/H] for [Eu/Fe] and [Ba/Eu] ratios, because the [Eu/Fe] ratio for 12 stars at very low metallicity is only an upper limit and therefore the data for these stars have not been considered in the computation of the mean and the standard deviation for [Eu/Fe] and [Ba/Eu] ratios. In the case of [Ba/Eu] and [Eu/Fe] we have simply divided the [Fe/H] axis in 15 bins of equal dimension (see Table 2.6); for [Ba/Fe] we have divided the [Fe/H] in 18 bins but we have merged the first three bins (starting from the lowest value in [Fe/H]) into a single bin in order to have enough data in the first bin (see Table 2.5). For [Ba/Eu] versus [Ba/H] we have split the data into 16 equal bins but again we have merged the first two pairs in two bins for the same reason (see Table 2.7).

In Fig. 2.5 we show the results for the model 3 (with the yields used in Travaglio et al. 2001) for [Ba/Fe] versus [Fe/H]. As evident from Fig. 2.5, this model does not fit the most recent data.

Moreover, the model in Fig. 2.5 is different from the similar model computed by Travaglio et al. (1999). We are using a different chemical evolution model and this gives rise to different results. The main difference between the two chemical evolution models (the one of Travaglio and the present one) is the age-[Fe/H] relation which grows more slowly in the model of Travaglio. The cause for this difference is probably the different adopted stellar lifetimes, the different M_{up} (i.e. the most massive star ending its life as C-O white dwarf) and to the yield prescriptions for iron which are probably the WW95 metallicity-dependent ones in the model of Travaglio et al. (1999), whereas we use the WW95 yields for the solar chemical composition, which produce a faster rise of iron and generally a better agreement with the [X/Fe] vs [Fe/H] plots.

To better fit the new data we have to extend the mass range for the production of the r-processed barium toward higher mass in order to reproduce [Ba/Fe] at lower metallicity.

In Fig. 2.6, where we have plotted the predictions of model 1 and model 2 for [Ba/Fe] versus [Fe/H]; it is clear that these models better fit the trend of the data. In these models the upper mass limit for the production of the r-processed Ba is $30M_{\odot}$ in the case of model 1, and $25M_{\odot}$ in the case of model 2. However, model 2 does not fit the trend of the data as well as model 1. In model 2 there is no dependence on stellar mass for a given metallicity in the yields of Ba and Eu. This prescription is clearly an oversimplification but shows how a model with yields only dependent on metallicity works, allowing us to estimate whether it is

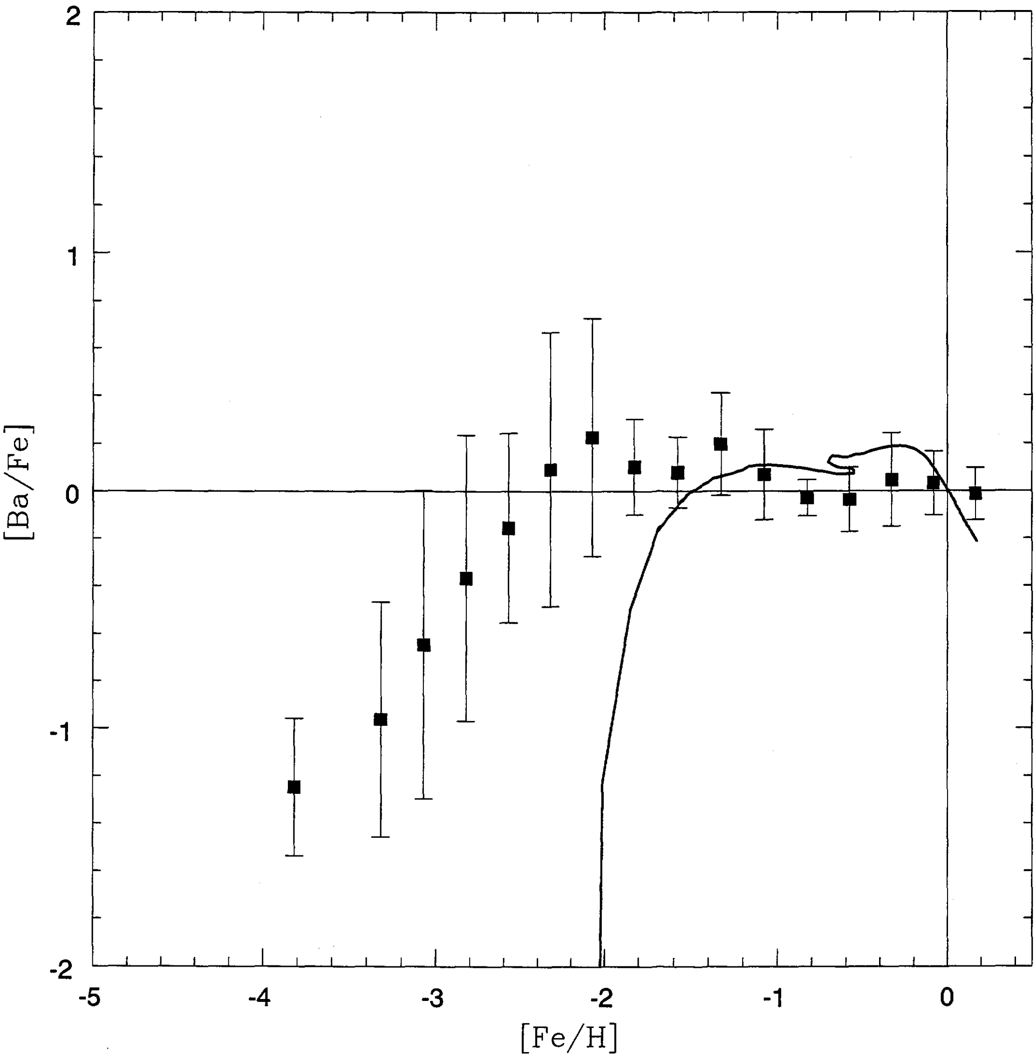

Figure 2.5. The ratio [Ba/Fe] versus [Fe/H]. The squares are the mean values of the data bins described in Table 2.5. For error bars we use the standard deviation (see Table 2.5). Solid line: the results of model 3 (Models are described in Table 2.2).

appropriate or not.

We have obtained similar results comparing the trend of the abundances of [Eu/Fe] versus [Fe/H] with the three models of Ishimaru et al. (2004) (Model 4, 5 and 6 in Table 2.2). The chemical evolution of this r-process element is shown in Fig. 2.7. Note that that these authors used a different chemical model. Again model 4 does not explain the low metallicity

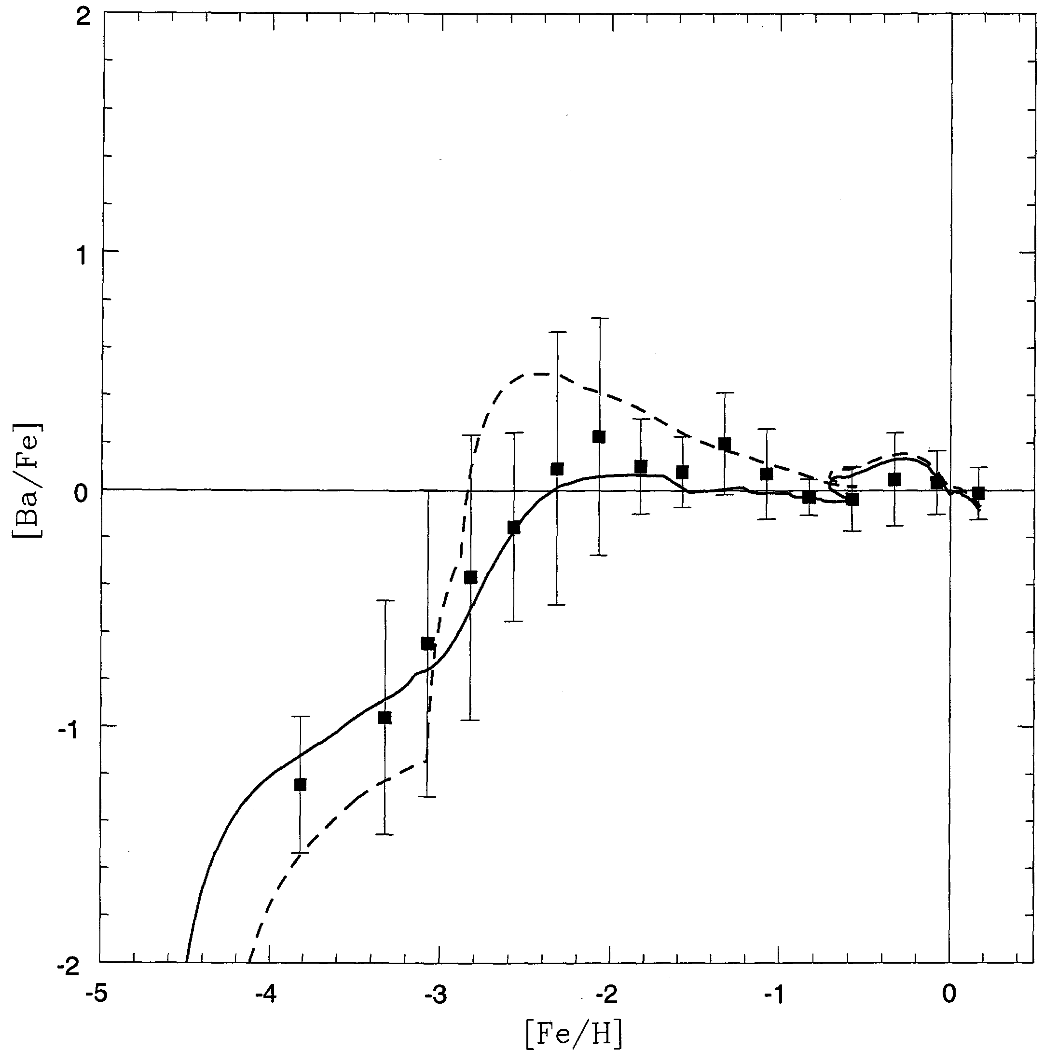

Figure 2.6. The data are the same as in Fig. 2.5. Solid line: the model 1; dashed line: the model 2 (Models are described in Table 2.2).

abundances and model 5 and 6 do not fit the trend of the data well.

In Fig. 2.8 we show the results of models 1 and 2 in this case for [Eu/Fe] versus [Fe/H]. The trend of the data is followed well by both models from low metallicity to solar metallicity.

In Table 2.8 we show the predicted solar abundances of Eu and Ba for all our models compared to the solar abundances by Grevesse & Sauval (1998). We also give the predicted s-process fraction in the barium solar abundance. The results of almost all our models are in

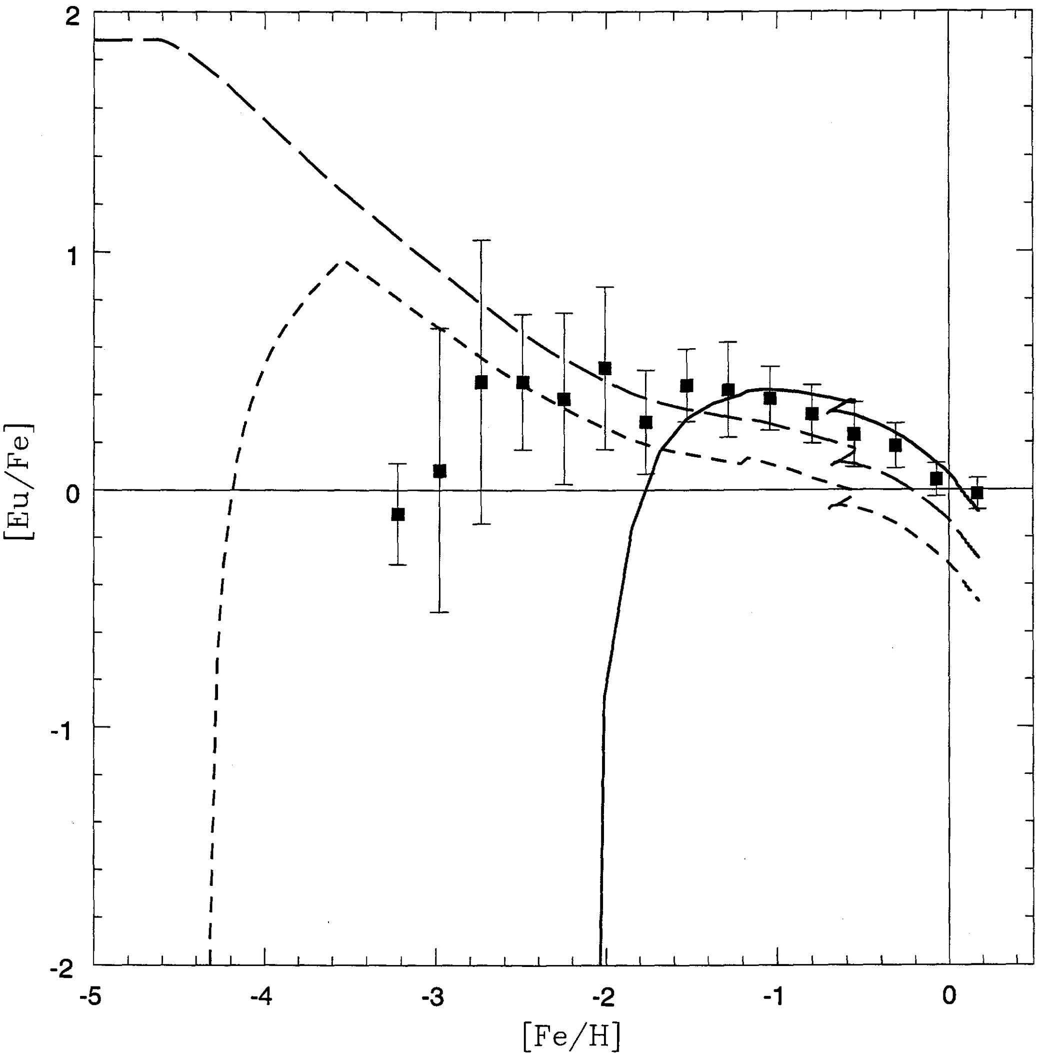

Figure 2.7. [Eu/Fe] versus [Fe/H]. The squares are the mean values of the data bins described in the Table 2.6. For error bars we use the standard deviation (see Table 2.6). Solid line: the results of model 4, short dashed line the results of model 5, long dashed line the results of model 6 (Models are described in Table 2.2).

good agreement with the solar abundances with the exception of model 5 which underpredicts the Eu abundance by a factor of ~ 2. Note that we predict a different s-process fraction in the solar mixture (nearly 60% instead of 80%) as compared to the s-process fraction obtained by other authors with different chemical evolution codes as Travaglio et al. (1999) and Raiteri

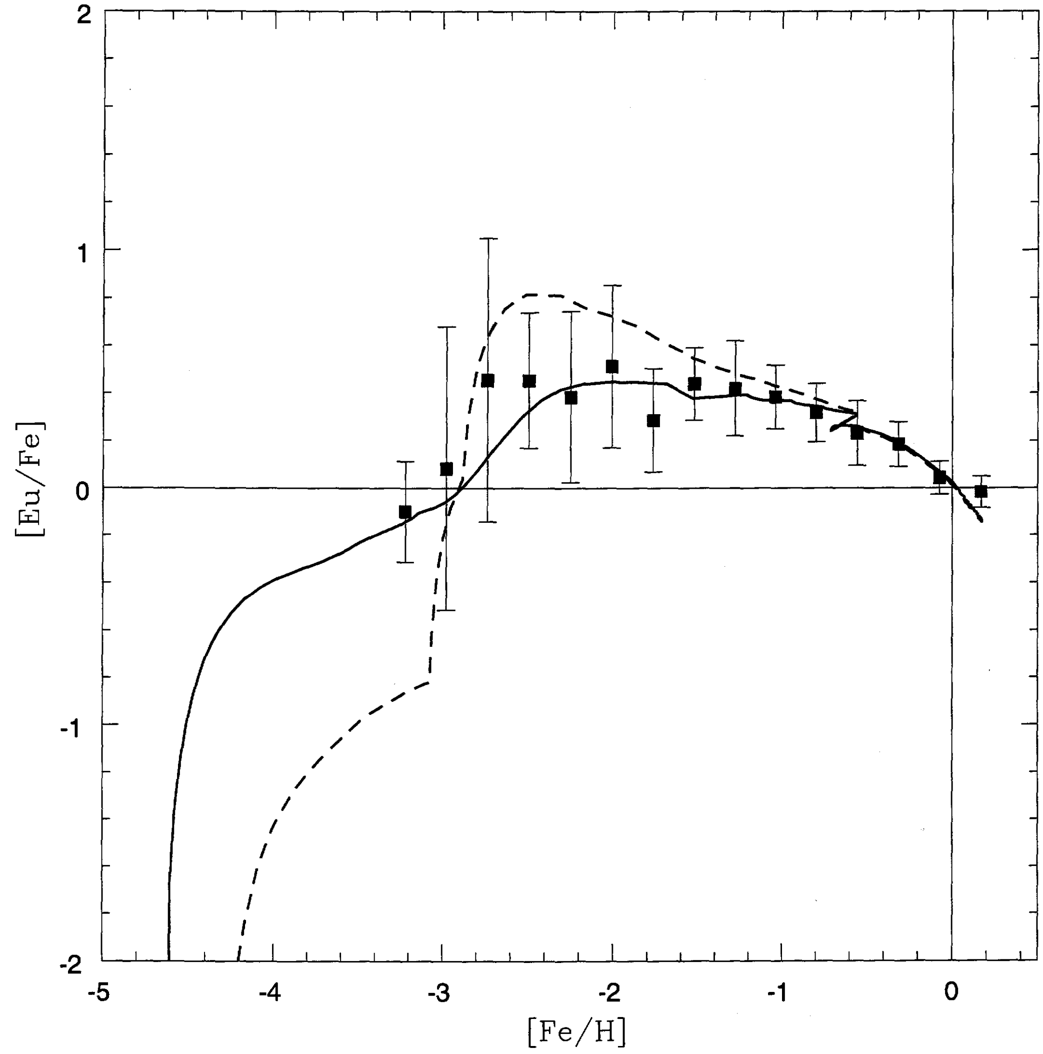

Figure 2.8. Data as in Fig. 2.7. Solid line: the results of model 1, dashed line the results of model 2 (Models are described in Table 2.2).

et al. (1999). In fact, although we use the same yields as Travaglio et al. (1999) for the production of Ba in low-intermediate mass stars, we obtain different results. This is due to the adopted chemical evolution model, which produces a different age-[Fe/H] relation which in turn affects the Ba production. This fraction of s-process Ba is also lower than the results obtained by means of stellar evolution models (e.g. Arlandini et al. 1999), although different s-process Ba fractions are possible in these models.

Table 2.8. Solar abundances of Ba and Eu, as predicted by our models, compared to the observed ones from Grevesse & Sauval (1998).

Mod	$(X_{Ba})_{pr}$	$\% Ba_s/Ba$	$X_{Ba_\odot}$	$(X_{Eu})_{pr}$	$X_{Eu_\odot}$
1	$1.55 \cdot 10^{-8}$	54%	$1.62 \cdot 10^{-8}$	$4.06 \cdot 10^{-10}$	$3.84 \cdot 10^{-10}$
2	$1.62 \cdot 10^{-8}$	51%		$3.96 \cdot 10^{-10}$	
3	$1.64 \cdot 10^{-8}$	44%		As model 1	
4	As model 1	As model 1		$4.48. \cdot 10^{-10}$	
5	As model 1	As model 1		$1.86 \cdot 10^{-10}$	
6	As model 1	As model 1		$2.84 \cdot 10^{-10}$	

Fig. 2.9, where we have plotted the abundances of [Ba/Eu] versus [Fe/H], and Fig. 2.10, where we plot [Ba/Eu] versus [Ba/H], have important features. The first is that the spread, that we can infer in these plots from the standard deviation of each bin, is smaller if we use the [Ba/H] ratio on the x axis; the second feature is that it is evident from the data that there is a plateau in the [Ba/Eu] ratio that is seen before the production of s-process Ba by the low-intermediate mass stars starts to be non negligible, at $[Fe/H] \sim -1$ and $[Ba/H] \sim -0.8$; finally, the timescale of the rise of the [Ba/Eu] value, due to the production of Ba by low-intermediate mass stars, is very well reproduced by our model.

The spread in the ratio of [Ba/Eu] both versus [Fe/H] and [Ba/H] is lower than the spread in [Ba/Fe] and [Eu/Fe], in particular when using as an evolutionary tracer the [Ba/H]. Considering the computed standard deviations as spread tracers, where the spread for [Ba/Fe] and [Eu/Fe] is higher ($[Fe/H] \sim -3$), their standard deviations are larger than 0.6 dex whereas the standard deviations for [Ba/Eu] is less than 0.15 dex.

For this reason we believe that the mechanism which produces the observational spread does not affect the ratio of these two elements. We propose that the explanation of the smaller spread in the ratio of [Ba/Eu] is that the site of production of these two elements is the same: the neutronized shell close to the mass cut in a SNII (see Woosley et al. 1994). What changes could be the amount of the neutronized material that each massive star expels during the SNII explosion. The mass cut and also the ejected neutronized material are still uncertain quantities and usually they are considered as parameters in the nucleosynthesis

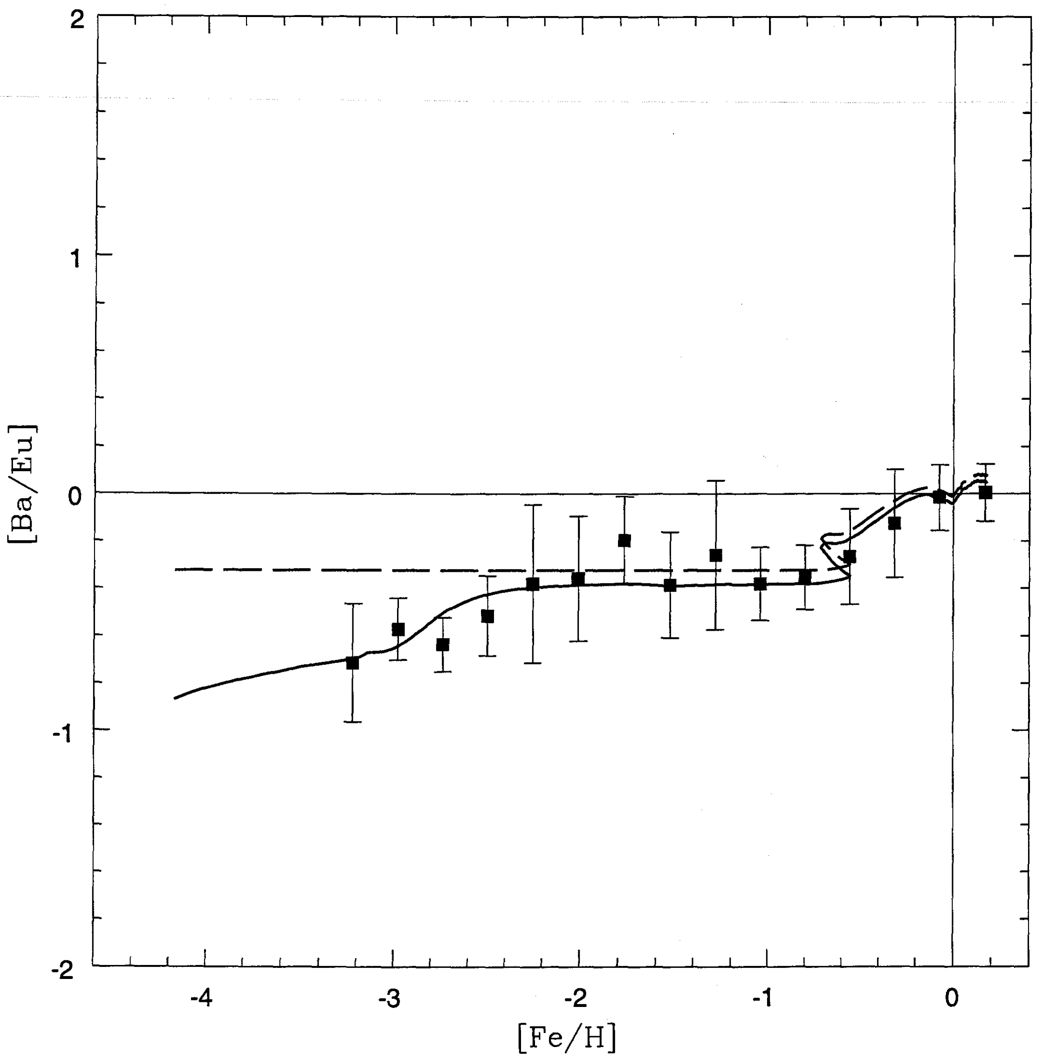

Figure 2.9. The ratio of [Ba/Eu] versus [Fe/H]. The squares are the mean values of the data bins described in Table 2.6. For error bars we use the standard deviation (see Table 2.6). Model 1: solid line, model 2: long dashed line (Models are described in Table 2.2).

codes for massive stars (see Rauscher et al. 2002, Woosley & Weaver 1995, Woosley et al. 1994).

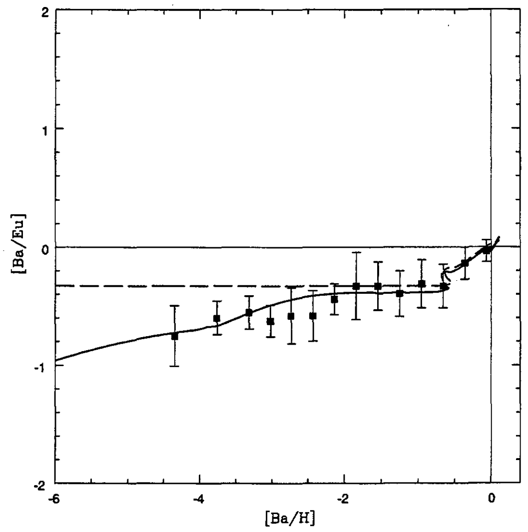

Figure 2.10. [Ba/Eu] versus [Ba/H]. The squares are the mean values of the data bins described in Table 2.7. For error bars we use the standard deviation (see Table 2.7). Model 1: solid line, model 2: long dashed line (Models are described in Table 2.2).

Upper and lower limit to the r-process production

The purpose of this section is to give upper and lower limits to the yields to reproduce the observed spread at low metallicities for Ba and Eu. An inhomogeneous model would provide better predictions about the dispersion in the [r-process/Fe] ratios if due to yield variations, but it is still useful to study the effect of the yield variations by means of our model.

First we explore the range of variations of the yields as functions of the stellar mass. To do this we have used model 1: in particular, we have modified the yields of model 1 for both elements (Ba and Eu), leaving untouched the s-process yields and changing only the yields of the r-process. Models 1Max and 1min and their characteristics are summarized in Table 2.9, where are indicated the adopted yields and the factors by which they have been modified relative to Model 1. In Fig. 2.11 and 2.12 we plot ratios [Ba/Fe] vs [Fe/H] and [Eu/Fe] vs [Fe/H] for the new models 1Max and 1min compared to the observational data; we show the same plot for the ratios [Ba/Eu] vs [Fe/H] in Fig.2.13 and and for [Ba/Eu] versus [Ba/H] in Fig. 2.14.

We can deduce from these upper and lower limit models that the large observed spread could also be due to a different production of heavy elements among massive stars ($> 15 M_\odot$).

Table 2.9. The stellar yields for model 1Max and 1Min for barium and europium in massive stars (r-process) in the case of a primary origin.

	Model 1Max		Model 1Min	
M_{star}	X_{Ba}^{new}	Factor	X_{Ba}^{new}	Factor
12.	$1.35 \cdot 10^{-6}$	1.5	$4.50 \cdot 10^{-7}$	0.5
$< 15.$	$4.50 \cdot 10^{-8}$	1.5	$1.50 \cdot 10^{-8}$	0.5
≥ 15	$3.00 \cdot 10^{-7}$	10.	$1.50 \cdot 10^{-9}$	0.05
30.	$1.00 \cdot 10^{-8}$	10.	$5.00 \cdot 10^{-11}$	0.05
M_{star}	X_{Eu}^{new}	Factor	X_{Eu}^{new}	Factor
12.	$4.50 \cdot 10^{-8}$	1.	$2.25 \cdot 10^{-8}$	0.5
$< 15.$	$3.00 \cdot 10^{-9}$	1.	$1.50 \cdot 10^{-9}$	0.5
≥ 15	$3.00 \cdot 10^{-8}$	10.	$1.50 \cdot 10^{-10}$	0.05
30.	$5.00 \cdot 10^{-9}$	10.	$2.50 \cdot 10^{-11}$	0.05

This type of stars could produce different amounts of these elements independently of the mass. As we have introduced in the previous subsect. (2.1.4), it is possible to link this fact with the problems of mass cut and the fallback during the explosion of a SNII. If these elements are produced in a shell close to the iron core of the star, differences in the explosion behaviour can give rise to a different quantity of r-process elements expelled by each star. In this way we are able to explain the presence of the spread for the heavy elements and the absence of the same spread, for example, in the α-elements. The α-elements are produced mostly during the hydrostatic burning of massive stars and then ejected by the explosion.

Another approach can be followed to derive upper and lower limits for the model by changing the yields as functions of metallicity. Model 2, which is the model with yields independent of the mass and depending only on metallicity, will be our test model. In particular, model 2 assumes for the massive stars different yields for Ba and Eu in three ranges of metallicity (see Table 2.2). The new prescriptions for both Ba and Eu are summarized in Table 2.10, where are indicated the new limits for the ranges of metallicities for the model 2min and 2Max. Note that for the model 2Max we assume only two regimes of production of r-process elements as a function of the metallicities and so we distinguish only two ranges

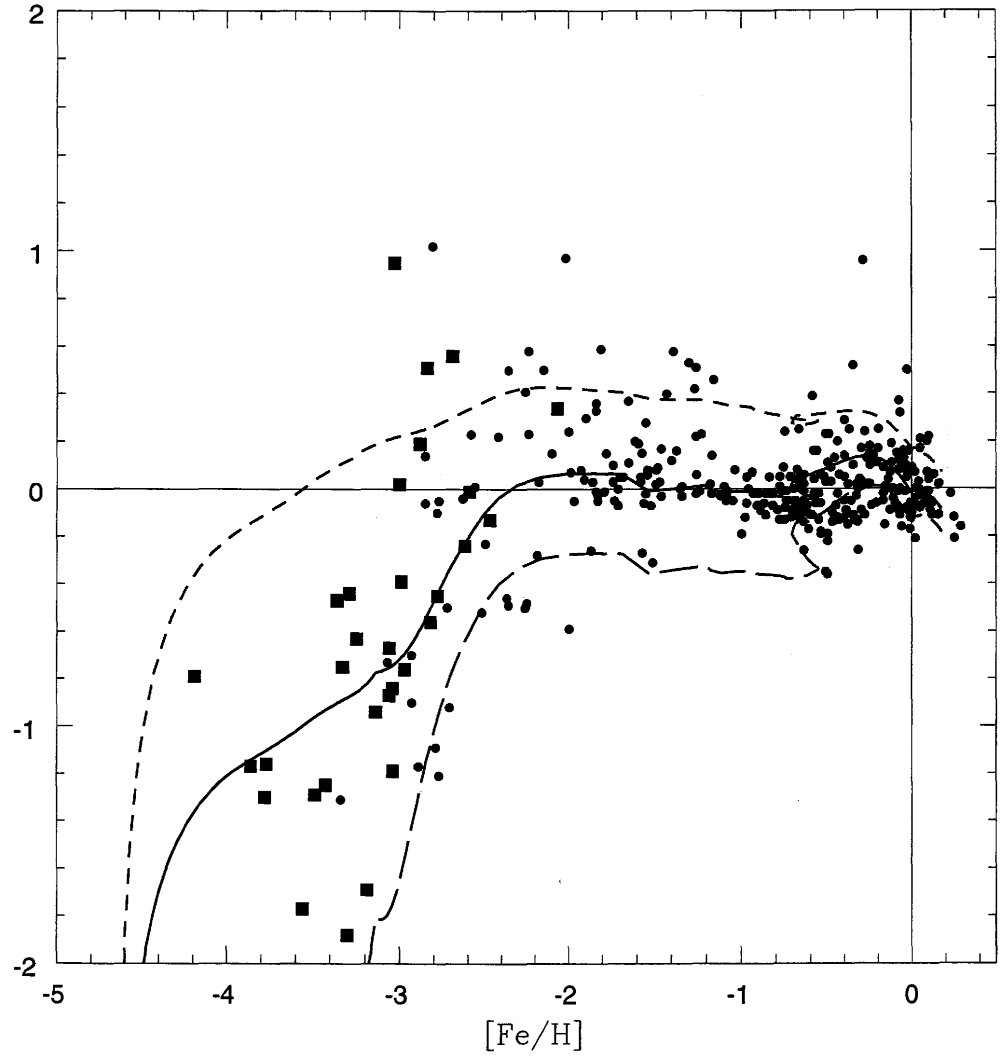

Figure 2.11. [Ba/Fe] versus [Fe/H] for the data by François et al. (2007) (filled squares) and for the other observational data (see Sect. 2 in the text, the filled circles). The solid line is the prediction of model 1, the short dashed line the prediction of model 1Max and the long dashed line the prediction of model 1min.

of metallicities.

In Fig. 2.15 and 2.16 we show the results of these two models (2Max and 2min) and of the original model 2 for [Ba/Fe] vs [Fe/H] and for [Eu/Fe] versus [Fe/H] compared to the observational data.

Changing the central range of metallicity, in which there is an enhancement of the pro-

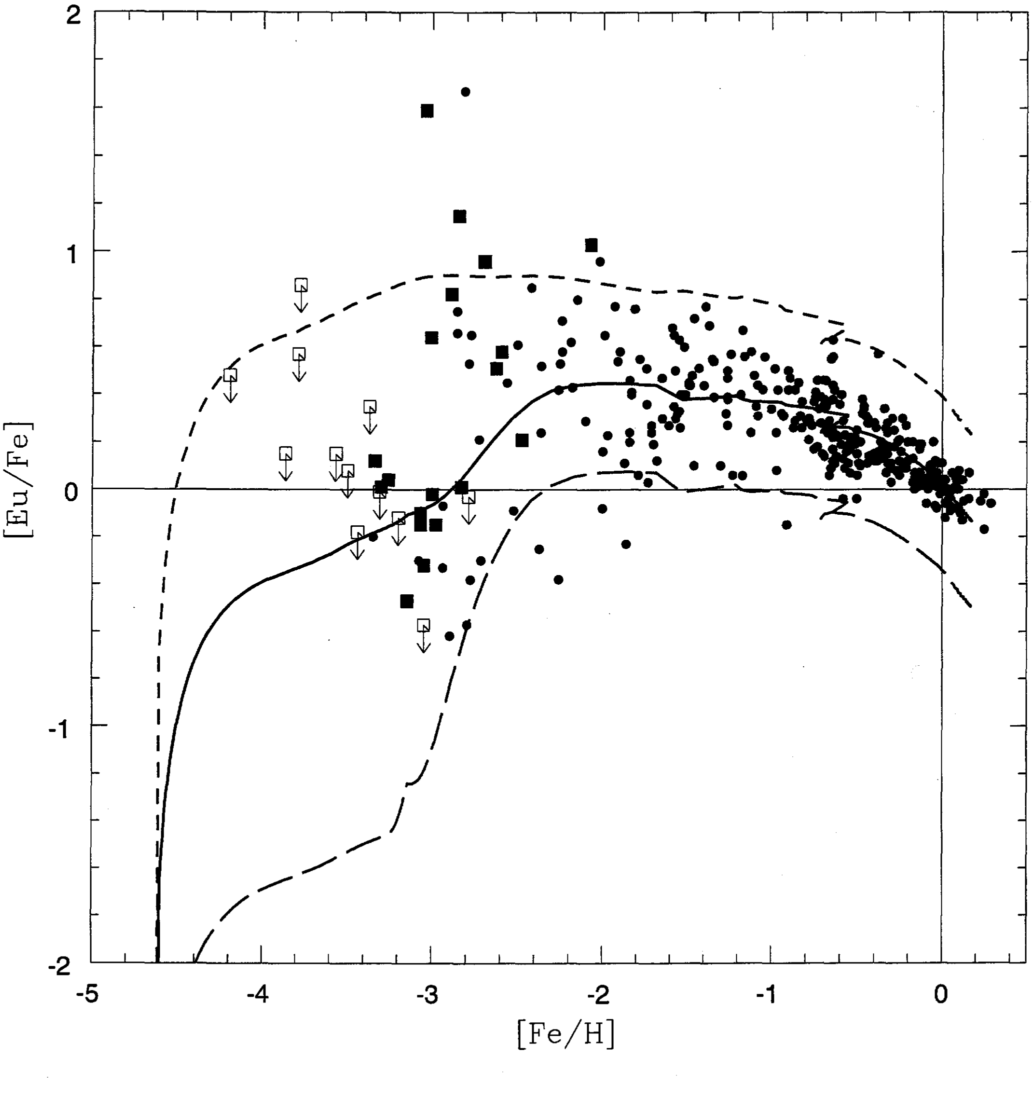

Figure 2.12. [Eu/Fe] versus [Fe/H]. The data by François et al. (2007) are filled squares, the open squares are upper limits (François et al. 2007). The filled circles are data by other observational works (see Sect. 2 in the text). The solid line is the prediction of model 1, the short dashed line the prediction of model 1Max and the long dashed line the prediction of model 1min.

duction of Ba and Eu, it is possible to produce the upper and lower limits. These two new models envelope the majority of the data at low metallicities. At higher metallicity the two models overlap the best model and so they do not contain all the spread in this part of the plot but most of them could be explained inside the typical observational error of 0.1 dex.

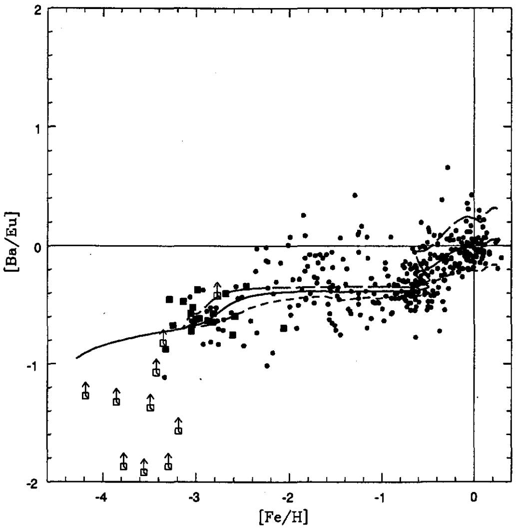

Figure 2.13. [Ba/Eu] versus [Fe/H]. The data by François et al. (2007) are filled squares, the open squares are lower limits (François et al. 2007). The filled circles are data by other observational works (see Sect. 2 in the text). The solid line is the prediction of model 1, the short dashed line the prediction of model 1Max and the long dashed line the prediction of model 1min.

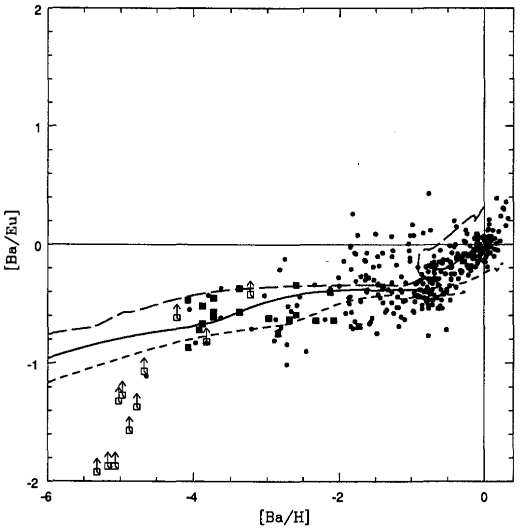

Figure 2.14. As in Fig. 2.13 but for [Ba/Eu] versus [Ba/H].

2.2 Lanthanum

In this Section we study the evolution of La. This element has a nucleosynthesis origin very similar to that of Ba. Therefore we will follow the same method of study that we adopted

Table 2.10. The stellar yields of model 2Max and model 2min for Ba and Eu in massive stars (r-process).

Z_{star} Model 2Max	Z_{star} Model 2min	X^{new}_{Ba} $10-25M_{\odot}$	X^{new}_{Eu} $10-25M_{\odot}$
–	$Z < 8\cdot10^{-6}$.	$1.00\cdot10^{-8}$	$5.00\cdot10^{-10}$
$Z < 1\cdot10^{-5}$	$8\cdot10^{-6} < Z < 1\cdot10^{-5}$	$1.00\cdot10^{-6}$	$5.00\cdot10^{-8}$
$Z > 1\cdot10^{-5}$	$Z > 1\cdot10^{-5}$	$1.60\cdot10^{-7}$	$8.00\cdot10^{-9}$

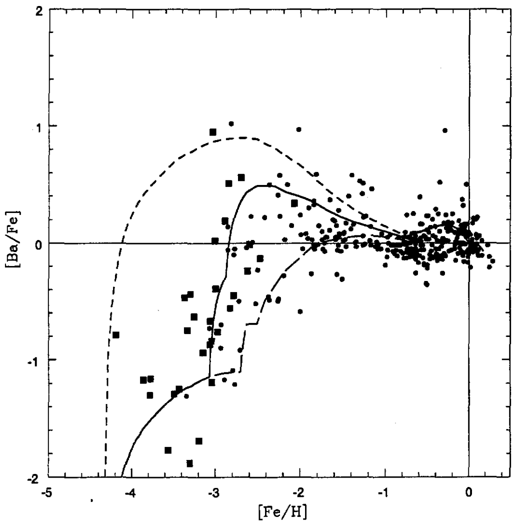

Figure 2.15. [Ba/Fe] versus [Fe/H]. The data are as in Fig. 2.11. The solid line is the prediction of model 2, the short dashed line the prediction of model 2Max and the long dashed line the prediction of model 2min.

for Ba.

2.2.1 Observational data

We adopted the very recent results by François (2007). For the abundances in the remaining range of [Fe/H], we took published high quality data in the literature from various sources: Cowan et al. (2005), Burris (2000), Johnson (2002), Pompeia et al. (2003) and McWilliam &

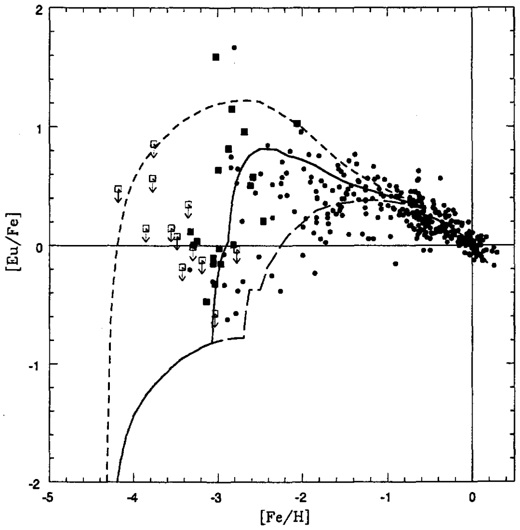

Figure 2.16. [Eu/Fe] versus [Fe/H]. The data are as in Fig. 2.12. The solid line is the prediction of model 2, the short dashed line the prediction of model 2Max and the long dashed line the prediction of model 2min.

Rich (1994). All of these data are relative to solar abundances of Grevesse & Sauval (1998).

2.2.2 Nucleosynthesis prescriptions for La

For the nucleosynthesis prescriptions of the s-process component of La we have adopted the yields of Busso et al. (2001) in the mass range 1.5-3$M_{\odot}$. We have extended the theoretical results of Busso et al. (2001) in the mass range $1.5 - 1M_{\odot}$, by simply scaling the values obtained for stars of $1.5M_{\odot}$ by the mass. We have extended the prescription to better fit the data with a [Fe/H] higher than solar. This hypothesis does not change the results of the model at [Fe/H]<0.

For the r-process contribution of La we give new prescriptions following the same method as for Ba in model 1: we assume an r-process contribution in massive stars (12 - 30 $M_{\odot}$), besides the s-process contribution from low mass stars. The yields of this r-process contribution are summarized in Table 2.11, in which the mass fraction of newly produced La is given as function of the mass.

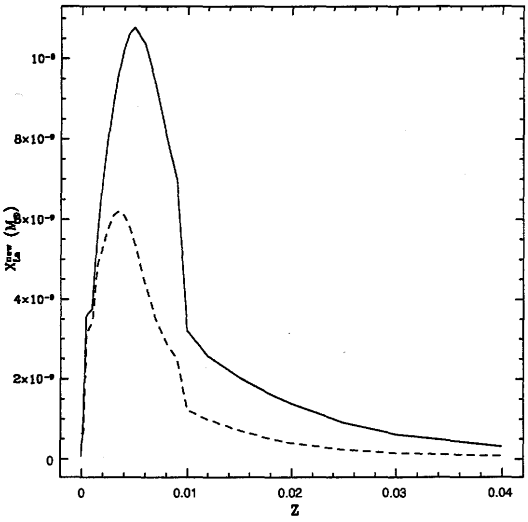

Figure 2.17. The stellar yields X_{La}^{new} from the paper of Busso et al. (2001) plotted versus stellar metallicity. The dashed line represents the prescriptions for stars of $1.5M_\odot$, the solid line those for stars of $3M_\odot$.

Table 2.11. The stellar yields for La in massive stars (r-process) in the case of primary origin.

M_{star}	X_{La}^{new}
12.	$9.00\cdot10^{-8}$
15.	$3.00\cdot10^{-9}$
30.	$1.00\cdot10^{-10}$

Table 2.12. The mean and the standard deviations for the abundance of [La/Fe] for the stars inside each bin along the [Fe/H] axis.

bin center [Fe/H]	bin dim.[Fe/H]	mean [La/Fe]	SD [La/Fe]	N. of data in the bin
-2.97	1.20	-0.13	0.48	29
-2.17	0.40	0.04	0.26	15
-1.78	0.40	0.06	0.17	7
-1.38	0.40	0.18	0.17	5
-0.99	0.40	-0.04	0.29	4
-0.59	0.40	0.19	0.32	5
-0.19	0.40	0.09	0.14	13
0.20	0.40	-0.08	0.09	7

2.2.3 Results

We divide the [Fe/H] axis in several bins and we compute the mean and the standard deviations from the mean of the ratios [La/Fe] for all the data inside each bin. These results are shown in Table 2.12, where we also summarize the center and the dimension of each bin and the number of data points contained in each of them. In Fig.2.18 we show the predictions of the chemical evolution model for La in the solar neighborhood using our prescriptions for the yields in massive stars and the prescriptions of Busso et al. (2001) for low mass stars, as described in the previous section. These results are new and the model well reproduces the trend of the stellar abundances at different [Fe/H] as well as the solar abundance of lanthanum. We obtain a La solar mass fraction of $1.35 \cdot 10^{-9}$ very close to the solar value of Asplund et al. (2005) of $1.38 \cdot 10^{-9}$.

Unfortunately, for this element there are not so many data. Only recently, even if its solar abundance is about a tenth of the Ba solar abundance, it has been measured because with only one stable isotope, La has more favorable atomic properties than Ba does, making the abundance analysis more straightforward. The predicted trend of La, with the new adopted yields well fits the observational data in the solar neighborhood.

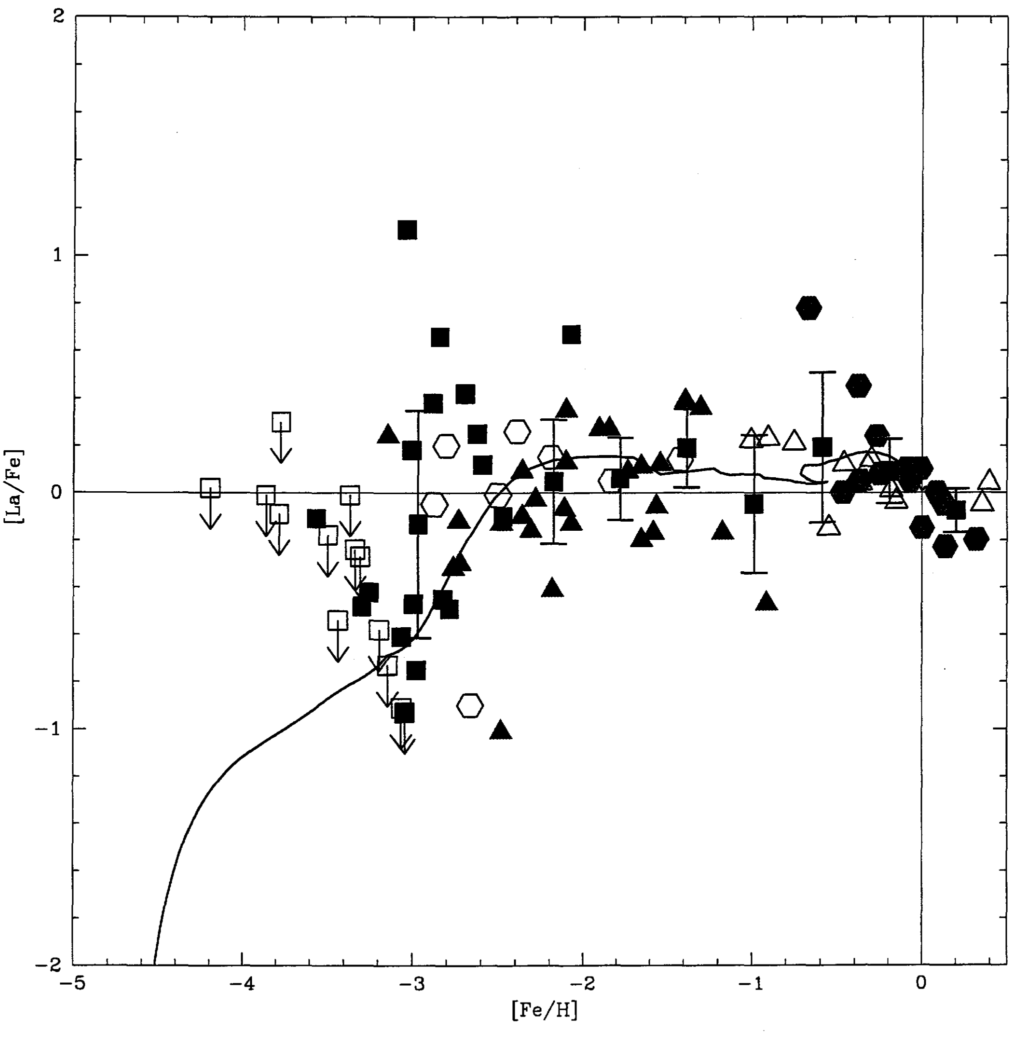

Figure 2.18. [La/Fe] versus [Fe/H]. The data are taken from François et al. (2007), (filled red squares, whereas the pink open squares are only upper limits), Cowan et al. (2005) (blue open hexagons), Johnson (2002) and Burris (2000) (blue solid triangles), Pompeia et al. (2003) (green filled hexagons) and McWilliam & Rich (1994) (open red triangles). The black squares are the mean values of the data bins described in the Table 2.12. As error bars we consider the standard deviation (see Table 2.12). The solid line is the result of our model for La (see Table 2.11), normalized to the solar abundance as measured by Asplund et al. (2005).

2.3 Strontium, zirconium and yttrium

In this Section we use the same methodology used for heavy neutron capture elements to constrain the yields in massive stars for light neutron capture elements, Sr, Zr and Y. Light elements are produced also by weak s-process in massive stars (see 1.2). In this work we do not distinguish between r-process production and weak s-process production and we rather set a nucleosynthesis related to the whole production in the massive stars. Nevertheless, as Travaglio et al. (2004) have shown, the fraction of solar Zr and Y, produced by the weak s-process, is marginal and the fraction of solar Sr is less than 10%. Moreover, we do not distinguish, as Travaglio et al. (2004) do, between a r-process contribution and another primary source, called in their work LEPP (lighter element primary process). We do not distinguish these two contributions because, from a theoretical point of view, it is not clear the difference between the two process.

2.3.1 Observational data

We adopted the new and accurate results by François et al. (2007). For the abundances in the remaining range of [Fe/H], we took published high quality data in the literature from various sources: Burris et al. (2000), McWilliam et al. (1995), Fulbright (2000, 2002), Mashonkina & Geheren (2001), Johnson (2002), Nissen & Schuster (1997), Prochaska et al. (2000) Gratton & Sneden (1994), Edvardsson et al. (1993), Stephens & Boesgaard (2002) Honda et al. (2004). All of these data are relative to solar abundances of Grevesse & Sauval (1998).

2.3.2 Nucleosynthesis prescriptions for Sr, Y and Zr

For the nucleosynthesis prescriptions of s-process we have adopted the yields by Travaglio et al. (2004) (see Fig.2.19. We have extended the theoretical results in the mass range $1-3M_{\odot}$, by simply scaling the values obtained for stars of $1.5M_{\odot}$ by the mass.

For the r-process, we give new prescriptions following the same method adopted for Ba in model 1: we assume an r-process contribution in massive stars (12 - 30 $M_{\odot}$), besides the s-process contribution from low mass stars. The yields are summarized in Table 2.13, in which the mass fraction of newly produced of Sr, Y, Zr is given as function of the mass.

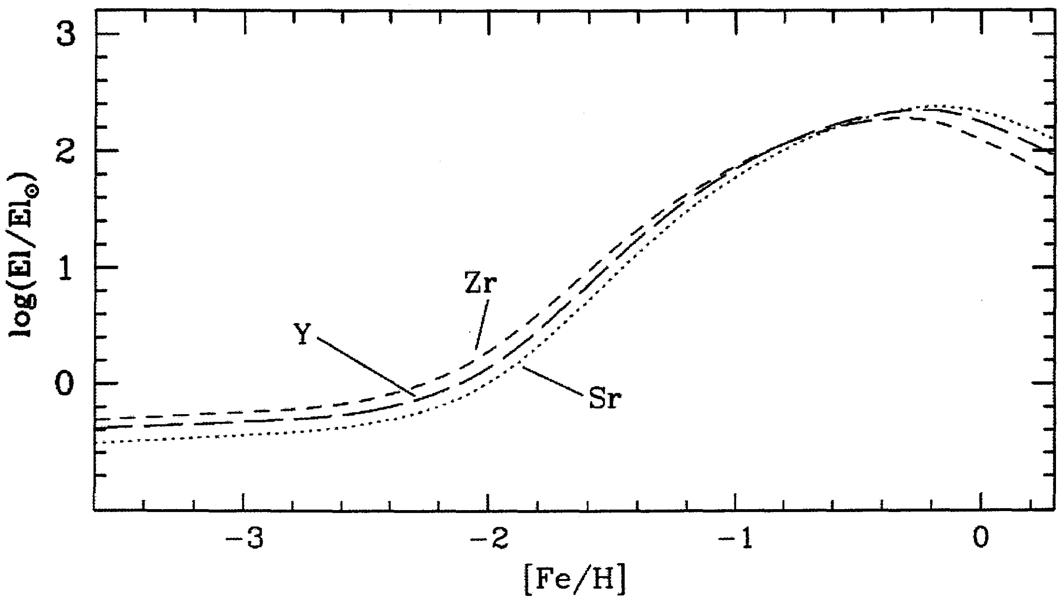

Figure 2.19. Production factors of Sr, Y, Zr respect to the solar value for 1.5 $M_\odot$ star at different metallicities.

Table 2.13. The stellar yields for Sr, Y and Zr in massive stars.

M_{star}	X_{Sr}^{new}	X_{Y}^{new}	X_{Zr}^{new}
12.	$1.80 \cdot 10^{-6}$	$3.60 \cdot 10^{-7}$	$1.80 \cdot 10^{-6}$
15.	$7.50 \cdot 10^{-8}$	$2.10 \cdot 10^{-8}$	$1.65 \cdot 10^{-7}$
30.	$3.25 \cdot 10^{-9}$	$1.00 \cdot 10^{-9}$	$5.00 \cdot 10^{-9}$

Table 2.14. The mean and the standard deviations for the abundance of [Sr/Fe] for the stars inside each bin along the [Fe/H] axis.

bin center [Fe/H]	bin dim.[Fe/H]	mean [Sr/Fe]	SD [Sr/Fe]	N. of data in the bin
-3.78	0.80	-0.86	0.68	9
-3.18	0.40	-0.41	0.66	28
-2.77	0.40	-0.14	0.38	29
-2.37	0.40	-0.43	0.42	12
-1.97	0.40	-0.28	0.35	17
-1.57	0.40	-0.14	0.23	8
-1.16	0.40	-0.06	0.15	9
-0.76	0.40	0.00	0.06	11
-0.36	0.40	-0.10	0.09	21
0.05	0.40	-0.04	0.10	11

2.3.3 Results

We divide the [Fe/H] axis in several bins and we compute the mean and the standard deviations from the mean of the ratios [Sr/Fe],[Y/Fe] and [Zr/Fe] for all the data inside each bin. These results are shown in Tables 2.14,2.15 and 2.16, where we also summarize the center and the dimension of each bin and the number of data points contained in each of them. In Fig.2.20, 2.22 and 2.21 we show the predictions of the chemical evolution model for Sr, Y and Zr in the solar neighborhood using our prescriptions for the yields in massive stars and the prescriptions by Travaglio et al. (2004) for low mass stars, as described in the previous section. The model well reproduces the trend of the stellar abundances at different [Fe/H] as well as the solar abundances. In Table 2.17 we show the solar mass fractions for Sr, Y and Zr compared to the solar values by Asplund et al. (2005) and Grevesse & Sauval (1998), measured in meteorites and the resulting fraction produced by the main s-process in low mass stars, for our model. The Zr has a larger contribution by r-process than Sr and Y. These have almost the same contribution by s-process. These results are quite different from other chemical evolution models (see Travaglio et al. 2004), and this is probably due to the

Table 2.15. The mean and the standard deviations for the abundance of [Y/Fe] for the stars inside each bin along the [Fe/H] axis.

bin center [Fe/H]	bin dim.[Fe/H]	mean [Y/Fe]	SD [Y/Fe]	N. of data in the bin
-3.82	0.74	-0.75	0.22	3
-3.27	0.37	-0.31	0.36	13
-2.90	0.37	-0.18	0.34	47
-2.53	0.37	-0.17	0.27	35
-2.16	0.37	-0.17	0.16	26
-1.79	0.37	-0.11	0.22	44
-1.42	0.37	-0.05	0.18	35
-1.05	0.37	-0.04	0.15	32
-0.68	0.37	-0.03	0.10	81
-0.31	0.37	0.01	0.17	74
0.06	0.37	-0.01	0.14	61

different treatment of the coupling between halo phase and disc phase.

Sr is the element which presents the larger spread in the data at low metallicities, whereas Y and Zr seem to have rather smaller and similar spread. The mean ratio of [Zr/Fe] is super-solar in the range $-2.5 < [Fe/H] < 0$, whereas the [Sr/Fe] and [Y/Fe] have mean abundances slightly smaller than solar in the same range. This difference is due to different contributions of the s-process production to the solar abundances. For values of $[Fe/H] < -2.5$ the ratios of [Sr/Fe], [Y/Fe] and [Zr/Fe] start to decrease. The yields adopted in this work for Sr, Y and Zr show to well fit the trends of the observational data in the solar neighborhood over the whole range of metallicities.

Table 2.16. The mean and the standard deviations for the abundance of [Zr/Fe] for the stars inside each bin along the [Fe/H] axis.

bin center [Fe/H]	bin dim.[Fe/H]	mean [Zr/Fe]	SD [Zr/Fe]	N. of data in the bin
-3.44	0.66	-0.05	0.34	10
-2.94	0.34	0.17	0.31	30
-2.60	0.34	0.22	0.27	27
-2.27	0.34	0.20	0.21	23
-1.94	0.34	0.26	0.26	23
-1.60	0.34	0.19	0.18	29
-1.27	0.34	0.29	0.18	19
-0.93	0.34	0.13	0.15	25
-0.60	0.34	0.07	0.15	44
-0.26	0.34	0.14	0.20	41
0.07	0.34	0.02	0.09	36

Table 2.17. Solar abundances of Sr, Y and Zr, as predicted by our model, compared to the observed ones from Grevesse & Sauval (1998) and the ones by Asplund et al. (2005). In the last column, the resulting fraction of each element produced by the main s-process in the solar abundance

	Elem.	Meteorites Asplund et al.	Meteorites Grevesse & Sauval	Model	s-process solar fraction
38	Sr	2.88 ± 0.04	2.92 ± 0.05	2.84	68%
39	Y	2.17 ± 0.04	2.23 ± 0.02	2.12	63%
40	Zr	2.57 ± 0.02	2.61 ± 0.04	2.58	33%

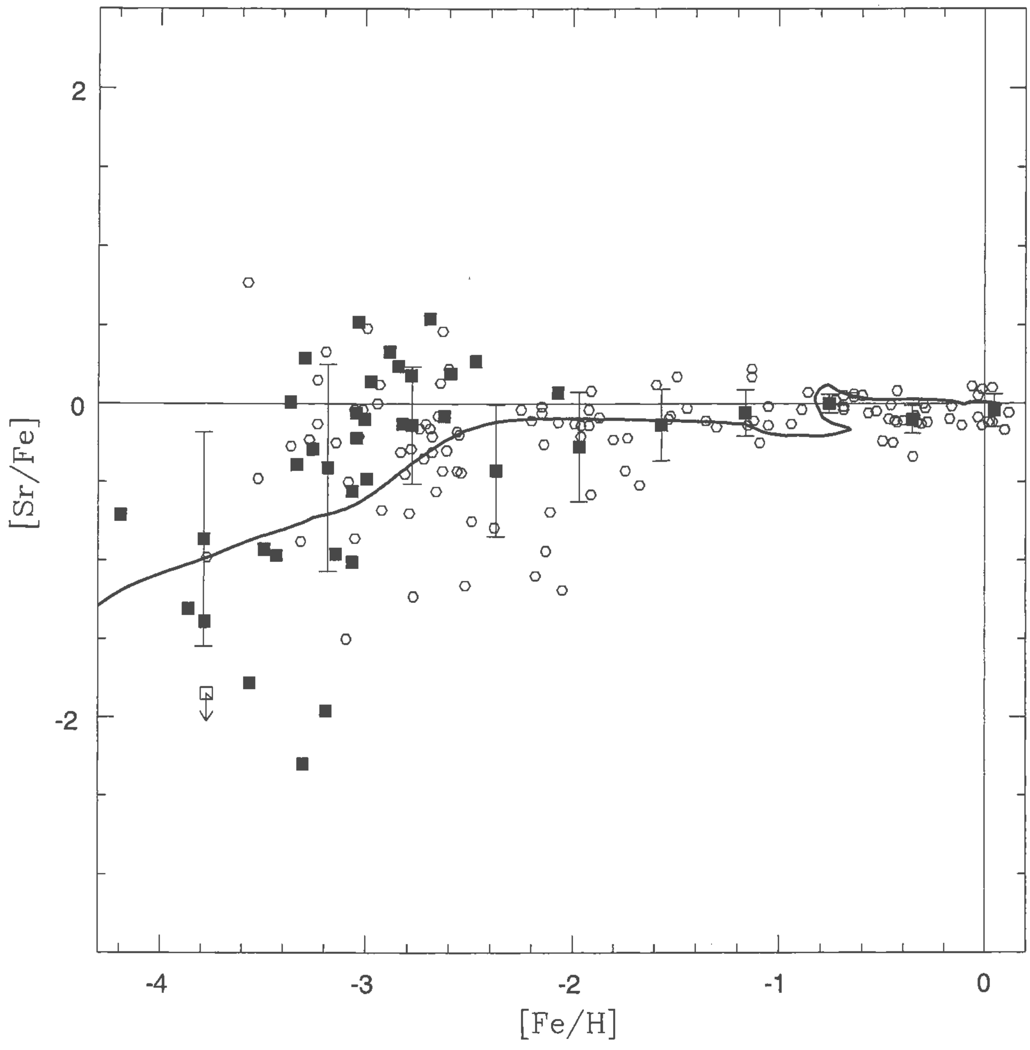

Figure 2.20. [Sr/Fe] versus [Fe/H]. The data are taken from François et al. (2007), (filled red squares, whereas the pink open squares are only upper limits) and other authors (blue dots). The black squares are the mean values of the data bins described in the Table 2.14. As error bars we consider the standard deviation (see Table 2.14). The solid line is the result of our model for Sr (see Table 2.13), normalized to the solar abundance as measured by Asplund et al. (2005).

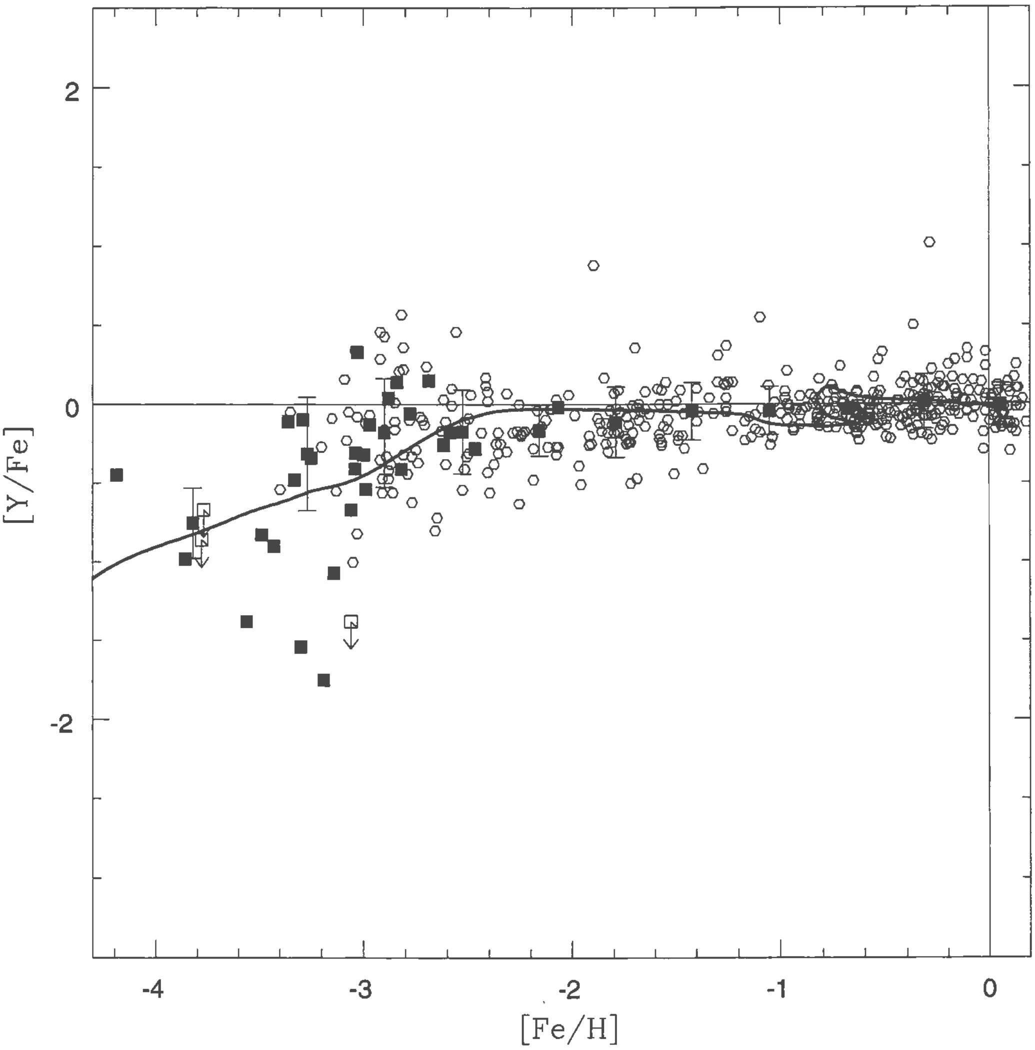

Figure 2.21. [Y/Fe] versus [Fe/H]. The data are taken from François et al. (2007), (filled red squares, whereas the pink open squares are only upper limits) and other authors (blue dots). The black squares are the mean values of the data bins described in the Table 2.15. As error bars we consider the standard deviation (see Table 2.15). The solid line is the result of our model for Y (see Table 2.13), normalized to the solar abundance as measured by Asplund et al. (2005).

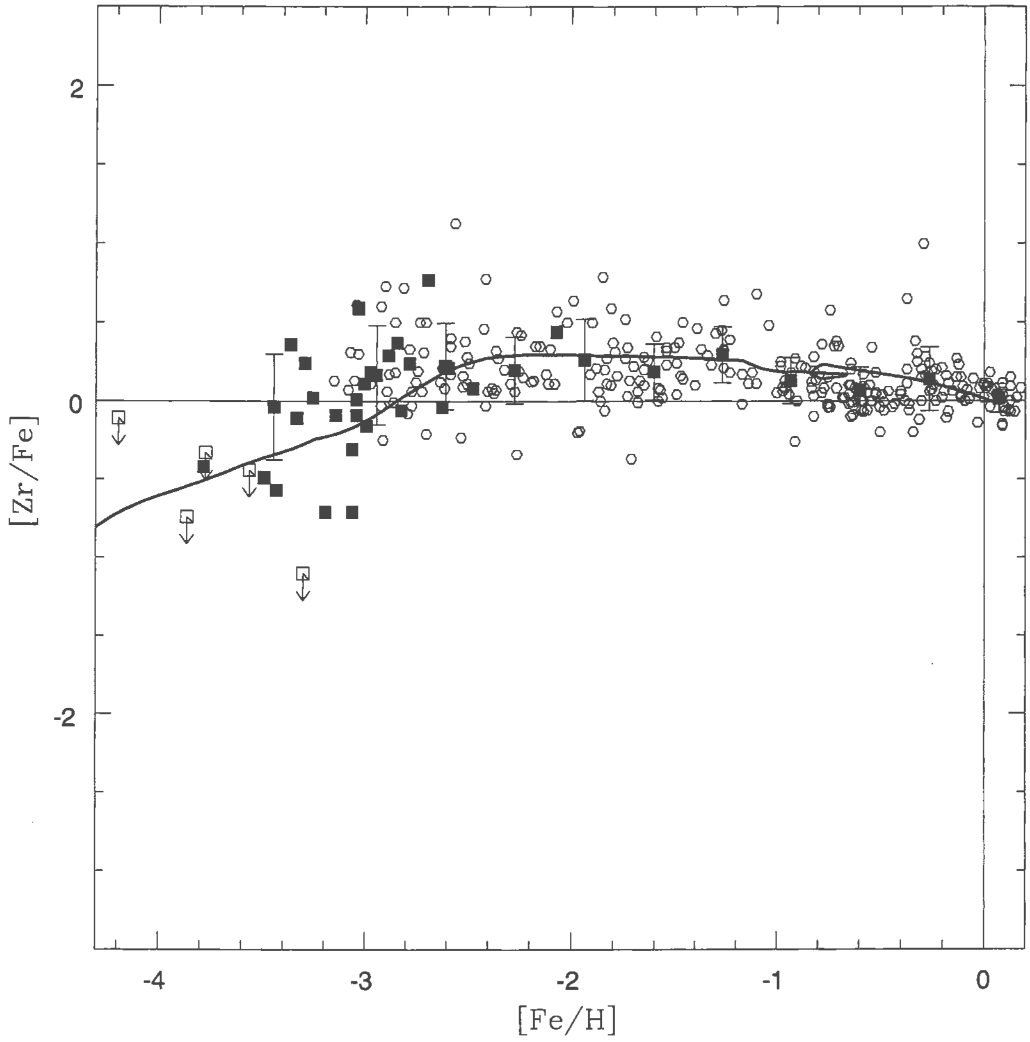

Figure 2.22. [Zr/Fe] versus [Fe/H]. The data are taken from François et al. (2007), (filled red squares, whereas the pink open squares are only upper limits) and other authors (blue dots). The black squares are the mean values of the data bins described in the Table 2.16. As error bars we consider the standard deviation (see Table 2.16). The solid line is the result of our model for Zr (see Table 2.13), normalized to the solar abundance as measured by Asplund et al. (2005).

Chapter 3

Abundance gradients in the Milky Way for α-elements, iron peak elements, barium, lanthanum and europium

"The sky was clear – remarkably clear –
and the twinkling of all the stars seemed
to be but throbs of one body, timed by a common pulse."
by Thomas Hardy

We calculate here the behaviour of the abundance gradients of the largest number of heavy elements (O, Mg, Si, S, Ca, Sc, Ti, Co, V, Fe, Ni, Zn, Cu, Mn, Cr, Sr, Y, Zr, Ba, La and Eu) ever considered in this kind of models. We are also able to test the the recent nucleosynthesis prescriptions described in François et al. (2004) for the α- and iron peak elements and in the previous chapter for neutron capture elements;

Chemical evolution models adopting the above nucleosynthesis prescriptions have been shown to reproduce the evolution of the abundances in the solar neighborhood. Here we extend our predictions to the whole disk to check whether these prescriptions can also reproduce the abundance gradients. We compare our model predictions to new observational data collected by Andrievsky et al. (2002abc, 2004) and Luck et al. (2003) (hereafter 4AL).

They measured the abundances of all the selected elements (except Ba) in a sample of 130 galactic Cepheids found in the galactocentric distance range from 5 to 17 kpc. In addition to the data by 4AL we compare our theoretical predictions with abundance measurements in giants and open cluster located at even larger galactocentric distances.

3.1 Observational data

In this work we use the data by 4AL for all the studied elemental gradients. These accurate data have been derived for a large sample of galactic Cepheids. Cepheids variables have a distinct role in the determination of radial abundance gradients for a number of reasons. First, they are usually bright enough that they can be observed at large distances, providing accurate abundances; second, their distances are generally well determined, as these objects are often used as distance calibrators (see Feast & Walker 1987); third, their ages are also well determined, on the basis of relations involving their periods, luminosities, masses and ages (see Bono et al. 2005). They generally have ages close to a few hundred million years. We can thus safely assume that they are representative of the present day gradients. The 4AL sample contains abundance measurements for 130 Cepheid stars located between 5 and 17 kpc from the Galactic center, for all the elements we want to study but Ba. The advantage of this data is that it constitutes homogeneous sample for a large number of stars and measured elements. Therefore, the abundance gradients can be more closely traced with better statistics. Moreover, only for Cepheids it is possible to obtain abundances for so many elements, as well as a good estimate of the distance, necessary to compute the gradients. 4AL obtained multiphase observations for the majority of stars. For the distant Cepheids they used 3-4 spectra to derive the abundances, while for nearby stars 2-3 spectra were used. We also adopt the data by Yong et al. (2006), who computed the chemical abundances of Fe, Mg, Si, Ca, Ti, La and Eu for 30 Cepheids stars. Among these 30 stars, we choose only the 20 which are not in common with the sample of 4AL. We apply the off-set found by Yong et al. (2006) with respect to the work of 4AL, in order to homogenize the two samples.

We use the data of Daflon & Cuhna (2004) to compare the results on Cepheids with another class of young objects. Their database contains abundances of C, N, O, Mg, Al, Si, S for 69 late O- to early B-type star members of 25 OB associations, open clusters and HII regions. They determine the mean abundances of the different clusters or associations of young objects. These objects all have ages less than 50 Myr. Therefore, we assume that they also represent the present day gradients.

To extend the comparison between our model and the observational data toward the outer disk, we also include the datasets of Carraro et al. (2004) and Yong et al. (2005); these authors observed distant open clusters up to 22 kpc. We also show the average values of individual stars belonging to a cluster. These stars are red giants with an estimated age ranging from 2 Gyr to 5 Gyr. We compare these data with the results of our model at the sun formation epoch, i.e. 4.5 Gyr before the present time. Yong et al. (2005) measured the surface abundances of O, Mg, Si, Ca, Ti, Mn, Co, Ni, Fe La, Eu and Ba for 5 clusters, whereas Carraro et al. (2004) computed the surface abundances of O, Mg, Si,Ca, Ti, Ni, Fe in 2 clusters. One of the clusters of Carraro et al. (2004), Berkeley 29, is in common with the sample of Yong et al. (2005) and we show both measurements. The galactocentric distance of this object is 22 kpc and hence is the most distant open cluster ever observed.

We show the abundances of three field red giants, which have been identified in the direction of the southern warp of the Galaxy by Carney et al. (2005). In their work, they measure the abundances of O, Mg, Si, Ca, Ti, Mn, Co, Ni, Fe, La, Eu and Ba for the three red giants. The galactocentric distance of these object ranges from 10 kpc to 15 kpc. The age of these three stars is unknown but it is likely that it is similar to the age of the red giants measured in the old open clusters. Therefore, we may compare them with the abundances at the solar system formation time.

3.2 Chemical evolution model for the Milky Way

In our model, the Galaxy is assumed to have formed by means of two main infall episodes: the first forms the halo and the thick disk, the second the thin disk. The galactic thin disk is approximated by several independent rings, 2 kpc wide, without exchange of matter between them. We assume that the thin disk forms inside-out as first suggested by Matteucci & François (1989) and then by Chiappini et al. (2001). In particular, the time scale τ_D, expressed in Gyr, for the formation of the thin disk at different galactocentric distances is:

$$\tau_D(r) = 1.033r - 1.267. \tag{3.1}$$

where r is expressed in kpc. Chiappini et al. (2001) have shown that the chemical evolution of the halo can have an impact on the abundance gradients in the outer parts of the disk. They analyzed the influence of the halo surface mass density on the formation of the abundance gradients of O, S, Fe and N at large galactocentric distances. In their model A, the halo surface mass density is assumed to be constant and equal to $17 M_{\odot} pc^{-2}$ for $R \leq 8 kpc$ and decreases as R^{-1} outwards. A threshold gas density is assumed also for the halo and set to $4 M_{\odot} pc^{-2}$. Then model B has a constant surface mass density equal to $17 M_{\odot} pc^{-2}$ for all galactocentric distances and the threshold in the halo phase is the same as in model A. In their model C the halo surface mass density is assumed as in model A but it does not have a threshold in the halo phase. In their model D, both the halo surface mass density and the threshold are as in model A but the time scale for the halo formation at galactocentric distances greater than 10 kpc is set to 2 Gyr and to 0.8 Gyr for distances less than 10 kpc. In all the other models, the halo timescale is constant for all the galactocentric distances and equal to 0.8 Gyr. Here we will show our model predictions for model B. The differences among model A,B,C and D arise primarily in the predicted steepness of the gradients for the outermost disc regions of the galactic disc. In this zone, the model B predicts the flattest gradients among the models of Chiappini et al. (2001), and provides the best fit according to observed flatness in the recent data by 4AL and in the distant open clusters. Model A is also in good agreement with the abundance gradients traced by Cepheids up to ~ 12 kpc, whereas for larger galactocentric distances this model tends to be systematically below observations. We will show the predictions of this model only for the α-elements. Model C shows a trend similar to model A, whereas model D tends to be below the observations for galactocentric distances greater than $10 kpc$, so we chose to not show their predictions. We recall that below a critical threshold for the gas surface density ($7 M_{\odot} pc^{-2}$ for the thin disk and $4 M_{\odot} pc^{-2}$ for the halo phase) we assume no star formation. In Fig. (2.1) we show the predicted star formation rate for three different galactocentric distances: 4, 8 and 12 kpc; the SFR is the same for all galactocentric distances during the halo phase, due to the fact that the assumed halo mass density in the selected model B is not a function of galactocentric distance; the critical threshold of the gas surface density naturally produces a bursting star formation history in the outer part of the disk, whereas at the solar neighborhood, it happens only toward the end of the evolution. We note that at the solar galactocentric distance, which is assumed to be 8 kpc, the threshold also produces a hiatus between the halo phase and the thin disk phase.

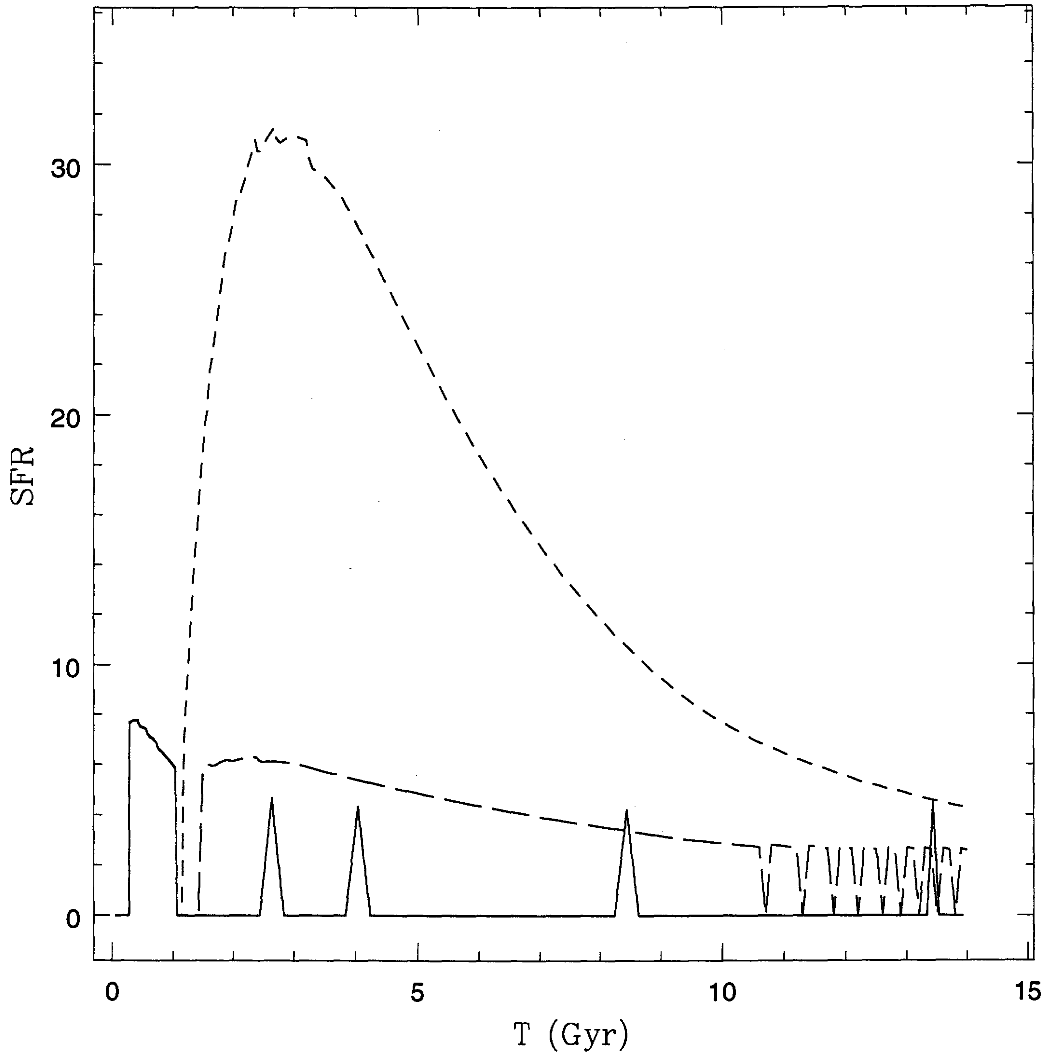

Figure 3.1. The SFR expressed in $M_{\odot} pc^{-2} Gyr^{-1}$, as predicted by the two infall model for different galactocentric distances: 4 kpc (short dashed line), 8 kpc (long dashed line) and 12 kpc (solid line). The SFR in the halo phase (indicated by the solid line) up to 0.8 Gyr, is the same for all the galactocentric distances, whereas in the disk the SFR changes according to the different infall rates. Note that at 4 kpc distance the SFR in the disk is much higher than at larger galactocentric distances. The gap in the SFR at the end of the halo-thick disk phase is evident in the solar neighborhood. The oscillations are due to to the threshold density.

3.3 Nucleosynthesis prescriptions

For the nucleosynthesis prescriptions of the Fe and the others elements (O, S, Si, Ca, Mg, Sc, Ti, V, Cr, Zn, Cu, Ni, Co and Mn), we adopted those suggested in François et al. (2004). They compared theoretical predictions of the [el/Fe] vs. [Fe/H] trends in the solar neighborhood for the mentioned above elements and they selected the best sets of yields to fit the data. For the yields of SNe II they found that the Woosley & Weaver (1995) ones provide the best fit. No modifications are required for the yields of Ca, Fe, Zn and Ni as computed for solar chemical composition. For oxygen the best results are given by the Woosley & Weaver (1995) yields computed as functions of the metallicity. For the other elements, variations in the predicted yields are required to best fit the data (see François et al. 2004 for details). For yields from type Ia SNe, revisions in the theoretical yields by Iwamoto et al. (1999) are needed for Mg, Ti, Sc, K, Co, Ni and Zn to best fit the data. The prescriptions for single low-intermediate mass stars are by van den Hoek & Groenewegen (1997), for the case of the mass loss parameter which varies with metallicity (see Chiappini et al. 2003a, model5). For neutron capture elements we adopt the nucleosynthesis prescriptions described in the previous chapter. For Ba and Eu the reference model used is model 1. In Table 3.1 the predicted and observed solar abundances are compared. In the next sections we check whether with the same nucleosynthesis prescriptions our model can explain the data in the other parts of the galactic disk.

3.4 Abundance gradients compared with the 4AL data

We used the model described in Sect.3.2 to predict the variation of the abundances of the studied elements along the galactic disk in the galactocentric range 5 - 17 kpc, at the present time. We then compared the abundances predicted by our model at the present time for all the elements with the observational data. To better understand the trend of the data, we divide the data in 6 bins as functions of the galactocentric distance. In each bin we compute the mean value and the standard deviations for all the elements. The results are shown in Table 3.2: in the first column we show the galactocentric distance range chosen for each bin, in the second column the mean galactocentric distance for the stars inside the considered bin, in the other columns the mean and the standard deviation computed for the abundances of every chemical elements, inside the considered bin. For some stars it has not been possible to

Table 3.1. Element abundances by Asplund et al. (2005) in the present-day solar photosphere and in meteorites (C1 chondrites) compared to the results of our model at the solar formation epoch.

	Elem.	Photosphere	Meteorites	Model
8	O	8.66 ± 0.05	8.39 ± 0.02	8.67
12	Mg	7.53 ± 0.09	7.53 ± 0.03	7.57
14	Si	7.51 ± 0.04	7.51 ± 0.02	7.58
16	S	7.14 ± 0.05	7.16 ± 0.04	7.20
20	Ca	6.31 ± 0.04	6.29 ± 0.03	6.25
21	Sc	3.05 ± 0.08	3.04 ± 0.04	3.05
22	Ti	4.90 ± 0.06	4.89 ± 0.03	4.90
23	V	4.00 ± 0.02	3.97 ± 0.03	3.59
24	Cr	5.64 ± 0.10	5.63 ± 0.05	5.59
25	Mn	5.39 ± 0.03	5.47 ± 0.03	5.44
26	Fe	7.45 ± 0.05	7.45 ± 0.03	7.41
27	Co	4.92 ± 0.08	4.86 ± 0.03	4.88
28	Ni	6.23 ± 0.04	6.19 ± 0.03	6.23
29	Cu	4.21 ± 0.04	4.23 ± 0.06	4.13
30	Zn	4.60 ± 0.03	4.61 ± 0.04	4.53
38	Sr	2.92 ± 0.05	2.88 ± 0.04	2.84
39	Y	2.21 ± 0.02	2.17 ± 0.04	2.12
40	Zr	2.59 ± 0.04	2.57 ± 0.02	2.58
56	Ba	2.17 ± 0.07	2.16 ± 0.03	2.19
57	La	1.13 ± 0.05	1.15 ± 0.06	1.11
63	Eu	0.52 ± 0.06	0.49 ± 0.04	0.56

measure all the abundances. We plot the results of our model at the present day normalized to both the solar observed abundances by Asplund et al. (2005) and to the mean value of the abundance data by 4AL at the solar distance. We adopt the solar abundances by Asplund et al. (2005) because they are more recent. These solar abundances have important differences for what concern elements as O and S, compared to the ones by Grevesse & Sauval (1998), whereas the differences are negligible for the neutron capture elements.

3.4.1 α-elements (O-Mg-Si-S-Ca)

We plot the results for these elements in Fig. 3.2 and 3.3. There is a discrepancy between our predictions normalized to the solar abundances by Asplund et al. (2005) and the mean abundance of these elements for Cepheids at the solar galactocentric distance. The predictions of our model for these elements at the present time at 8 kpc are supersolar, whereas the mean abundances of Cepheids for Mg, Ca and O are subsolar and this difference is particularly evident for Mg. This means that either our model predicts a too steep increase of metallicity in the last 4.5 Gyr or that the absolute abundances of Cepheids are underestimated. Some uncertainties in the absolute abundances could exist, but the slope of the abundance distributions should not be affected. If these subsolar abundances were real, then one might think that they are the effect of some additional infall episode, occurring in the last 4.5 Gyr. However, the goal of this work is to reproduce the trend of the gradients, so here this problem can be neglected and we can compare the data with the model results normalized to the mean abundances of the Cepheids at 8 kpc. These results well reproduce the trend of the data for all the five elements. Moreover, in the case of Si we note that the data show very little spread (as the small standard deviation values indicate) and our model (the one normalized to the mean abundance at 8 kpc) perfectly lies over the mean value in each bin. For S the values predicted by the model for small galactocentric distances are slightly low but inside the error bar of the data. The trend for Ca is nicely followed by our model and the data for Ca show very little spread. On the other hand, the trend of Mg shows a shallower slope toward the galactic center than the other α-elements. This is probably due to the lack of Mg data for the stars located from 4 to 6.5 kpc, which determines the steep slope for the other α-elements. The results of the model, if we use the prescriptions for the halo gas density of model A by Chiappini et al. (2001) well reproduce the data up to 10 kpc but model B

Table 3.2. The mean value and the standard deviation inside each bin for all the elements.

galactocentric distance range	mean GC distance(kpc)	mean [O/H]	SD [O/H]	mean [Mg/H]	SD [Mg/H]	mean [Si/H]	SD [Si/H]	mean [S/H]	SD [S/H
<6.5kpc	5.76	0.16	0.17	-0.19	0.17	0.21	0.13	0.37	0.19
6.5<–<7.5kpc	7.10	-0.08	0.13	-0.19	0.10	0.07	0.06	0.17	0.08
7.5<–<8.5kpc	8.00	-0.06	0.13	-0.19	0.13	0.06	0.06	0.09	0.10
8.5<–<9.5kpc	8.96	-0.12	0.16	-0.21	0.11	0.04	0.04	0.08	0.17
9.5<–<11 kpc	10.09	-0.16	0.19	-0.22	0.18	-0.07	0.07	-0.11	0.20
>11 kpc	12.33	-0.19	0.21	-0.32	0.13	-0.16	0.08	-0.23	0.15

galactocentric distance range	mean GC distance(kpc)	mean [Ca/H]	SD [Ca/H]	mean [Sc/H]	SD [Sc/H]	mean [Ti/H]	SD [Ti/H]	mean [V/H]	SD [V/H
<6.5kpc	5.76	0.11	0.19	0.15	0.18	0.19	0.13	0.14	0.14
6.5<–<7.5kpc	7.10	0.00	0.10	-0.05	0.18	0.05	0.08	0.04	0.05
7.5<–<8.5kpc	8.00	-0.04	0.07	-0.06	0.13	0.05	0.07	0.03	0.09
8.5<–<9.5kpc	8.96	-0.04	0.11	-0.09	0.13	0.04	0.06	-0.01	0.09
9.5<–<11 kpc	10.09	-0.13	0.09	-0.12	0.09	-0.05	0.14	-0.08	0.15
>11 kpc	12.33	-0.19	0.11	-0.21	0.11	-0.15	0.08	-0.21	0.11

galactocentric distance range	mean GC distance(kpc)	mean [Cr/H]	SD [Cr/H]	mean [Mn/H]	SD [Mn/H]	mean [Fe/H]	SD [Fe/H]	mean [Co/H]	SD [Co/
<6.5kpc	5.76	0.11	0.11	0.09	0.14	0.17	0.13	0.06	0.13
6.5<–<7.5kpc	7.10	0.05	0.08	0.05	0.12	0.05	0.07	-0.10	0.07
7.5<–<8.5kpc	8.00	0.04	0.11	0.01	0.11	0.01	0.06	-0.10	0.11
8.5<–<9.5kpc	8.96	0.03	0.12	0.00	0.09	-0.01	0.08	-0.06	0.11
9.5<–<11 kpc	10.09	-0.06	0.12	-0.18	0.13	-0.09	0.09	-0.17	0.18
>11 kpc	12.33	-0.20	0.10	-0.31	0.18	-0.22	0.09	-0.14	0.17

galactocentric distance range	mean GC distance(kpc)	mean [Ni/H]	SD [Ni/H]	mean [Cu/H]	SD [Cu/H]	mean [Zn/H]	SD [Zn/H]	mean [Y/H]
<6.5kpc	5.76	0.18	0.16	0.15	0.18	0.51	0.20	0.22
6.5<–<7.5kpc	7.10	0.02	0.07	0.07	0.12	0.28	0.10	0.20
7.5<–<8.5kpc	8.00	-0.02	0.08	0.08	0.30	0.26	0.12	0.18
8.5<–<9.5kpc	8.96	-0.04	0.09	0.12	0.19	0.28	0.14	0.17
9.5<–<11 kpc	10.09	-0.14	0.10	-0.35	0.29	0.16	0.09	0.05
>11 kpc	12.33	-0.23	0.12	-0.09	0.17	0.10	0.11	-0.05

galactocentric distance range	mean GC distance(kpc)	mean [Zr/H]	SD [Zr/H]	mean [La/H]	SD [La/H]	mean [Eu/H]	SD [Eu/H]
<6.5kpc	5.76	-0.01	0.13	0.21	0.10	0.17	0.14
6.5<–<7.5kpc	7.10	-0.05	0.09	0.19	0.07	0.05	0.06
7.5<–<8.5kpc	8.00	-0.08	0.10	0.22	0.06	0.08	0.08
8.5<–<9.5kpc	8.96	-0.04	0.10	0.26	0.08	0.08	0.10
9.5<–<11 kpc	10.09	-0.10	0.12	0.23	0.09	0.04	0.13
>11 kpc	12.33	-0.23	0.12	0.12	0.11	0.00	0.14

better reproduces the data for larger galactocentric distances. For this reason in the next sections we will show only the results of model B. In Table 3.3 we show the slopes of the gradients for all the studied elements, as predicted by model B at the present time. The gradients become flatter towards the outermost disk regions, in agreement with the Cepheid data. Each element has a slightly different slope, due to the different production timescales and nucleosynthesis processes. In particular, α-elements (O, Mg, Si, Ca etc..) generally have flatter slopes than the Fe-peak-elements. In addition, there are differences even among the α-elements such as Si and Ca relative to Mg and O: the slightly steeper slope of Si and Ca is due to the fact that these elements are produced also by Type Ia SNe, whereas O and Mg are not. In general, elements produced on longer timescales have steeper gradients. This is confirmed by the observations not only of Cepheids but also of open clusters and HII regions. However, the predicted gradients for s- and r- process elements seem flatter than all the others. The reason for this is that they are produced in very restricted stellar mass ranges producing an increase of their abundances at low metallicities until they reach a constant value for [Fe/H] > -3.0 (see Fig. 2.18). The variations between gradients are small but they

Table 3.3. Model results for present time gradients for each element. We show the gradients computed as a single slope, for all the range of galactocentric distance considered, and as two slopes: from 4 to 14 kpc and from 16 to 22 kpc.

	Fe	O	Mg	Si	S	Ca	Cu
$\frac{\Delta[el/H]}{\Delta R}(dex/kpc)$from 4 to 22 kpc	-0.036	-0.028	-0.031	-0.033	-0.034	-0.034	-0.050
$\frac{\Delta[el/H]}{\Delta R}(dex/kpc)$from 4 to 14 kpc	-0.052	-0.035	-0.039	-0.045	-0.047	-0.047	-0.070
$\frac{\Delta[el/H]}{\Delta R}(dex/kpc)$from 16 to 22 kpc	-0.012	-0.011	-0.012	-0.012	-0.012	-0.012	-0.014
	Zn	Ni	Sc	Ti	V	Cr	Mn
$\frac{\Delta[el/H]}{\Delta R}(dex/kpc)$from 4 to 22 kpc	-0.038	-0.034	-0.036	-0.032	-0.038	-0.036	-0.038
$\frac{\Delta[el/H]}{\Delta R}(dex/kpc)$from 4 to 14 kpc	-0.054	-0.047	-0.051	-0.043	-0.056	-0.052	-0.057
$\frac{\Delta[el/H]}{\Delta R}(dex/kpc)$from 16 to 22 kpc	-0.012	-0.012	-0.012	-0.012	-0.011	-0.012	-0.011
	Co	Sr	Y	Zr	Ba	Eu	La
$\frac{\Delta[el/H]}{\Delta R}(dex/kpc)$from 4 to 22 kpc	-0.037	-0.020	-0.020	-0.022	-0.021	-0.030	-0.021
$\frac{\Delta[el/H]}{\Delta R}(dex/kpc)$from 4 to 14 kpc	-0.055	-0.016	-0.016	-0.019	-0.032	-0.036	-0.032
$\frac{\Delta[el/H]}{\Delta R}(dex/kpc)$from 16 to 22 kpc	-0.011	-0.010	-0.010	-0.013	-0.009	-0.013	-0.008

may be statistically significant, in particular those derived from Cepheids: all the Cepheids have similar atmospheric parameters (atmospheric temperature, surface gravity); their relative abundances are much less affected than the absolute abundances by the effect of using LTE models instead of recent NLTE, 3D models. Therefore the gradients from Cepheids seem to be well established.

3.4.2 Iron peak elements (Sc-Ti-Co-V-Fe-Ni-Zn-Cu-Mn-Cr)

The ten elements of the so-called iron peak are plotted in Figs. 3.4, 3.5, 3.6 and 3.8 (for Cr). The present time predictions of our model for iron peak abundances are super-solar at 8 kpc, as for the α-elements. On the other hand, the mean values for iron peak elements in Cepheids in the bin at 8 kpc are in general solar, except Zn, which is super-solar and Sc and Co, which are sub-solar. Nevertheless the model gives a prediction for the trends of the gradients for these elements which is very good, in particular in the cases of V, Fe, Ni, Mn and Cr, as

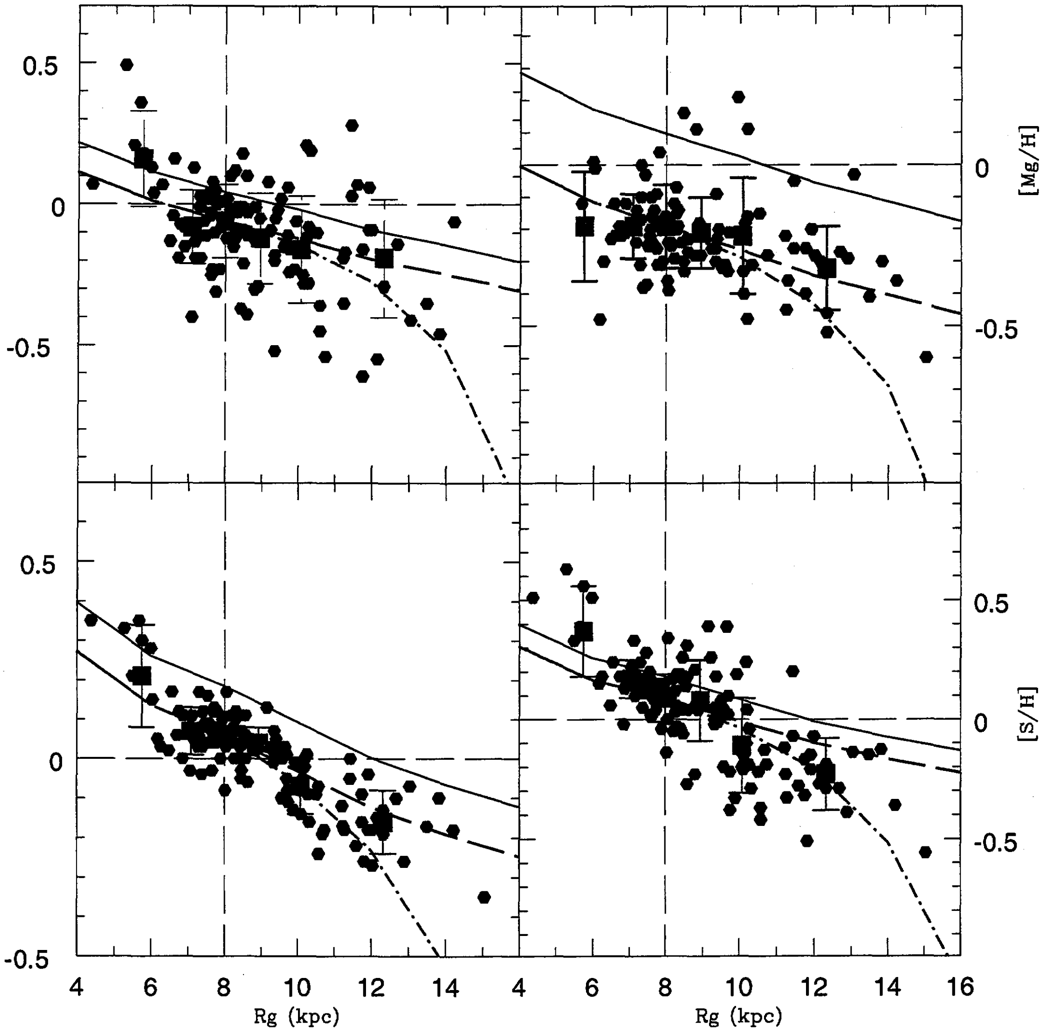

Figure 3.2. Abundances for O, Mg, Si and S as functions of the galactocentric distance. The blue dots are the data by 4AL, the red squares are the mean values inside each bin only for the data by 4AL and the error bars are the standard deviations (see Table 3.2). The thin solid line is our model normalized to the observed solar abundances by Asplund et al. (2005), whereas the thick dashed line is normalized to the mean value at the bin centered in 8 kpc (the galactocentric distance of the Sun). The dash-dotted line is the result of the model with the prescriptions for the halo gas density of model A by Chiappini et al. (2001) normalized to the mean value of the bin centered in 8 kpc (cfr. Sect.3).

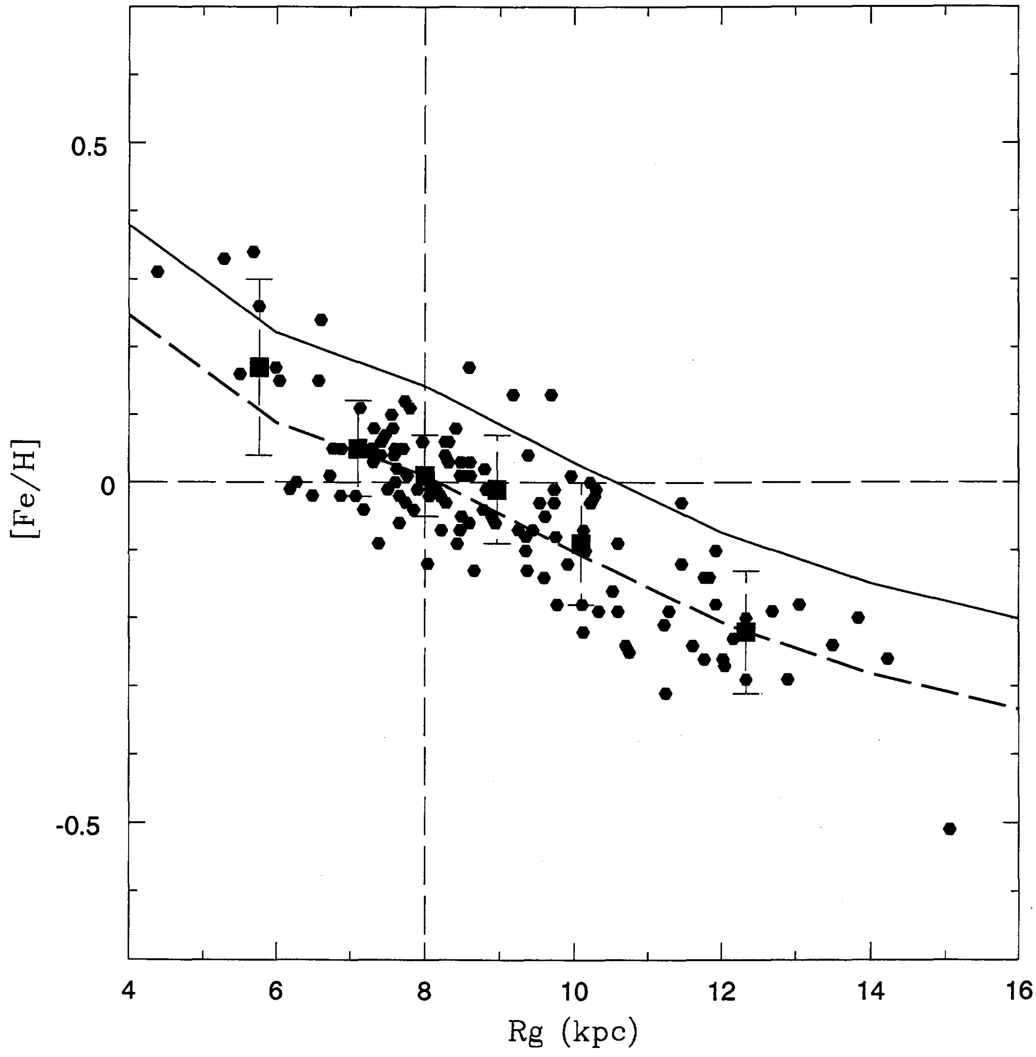

Figure 3.3. The gradient of [Ca/H]. The models and the symbols are the same as in Fig. 3.5.

shown by the results of the model normalized to the mean value of the bin centered at 8kpc. A problem is present for Co, for which a too low abundance is predicted by the model at galactocentric distances > 12 kpc.

3.4.3 Neutron capture elements (Sr-Y-Zr-Ba-La-Eu)

As we have seen, neutron capture elements present a large spread at low metallicities. However, since the Cepheids are young metal-rich stars, this problem is not important. As shown in Fig. 3.7 and 3.8, the spread in the data as a function of galactocentric distance is small. In the case of Eu our model well reproduces both the observed gradient and the mean value for the Cepheid abundance at 8 kpc. On the other hand, the mean value of the La abundance in the data by 4AL at the solar galactocentric distance is about a factor of 1.5 higher than the predicted abundance by our model and the predictions for La show slightly steeper gradients than the data. The model well reproduces the gradient for Y and its mean value for the Cepheids abundance at 8 kpc, as well as the gradient for Zr whereas the present predicted abundance at the solar distance for Zr is slightly higher. In Fig. 3.7 and 3.8, we show the predicted trend of the neutron capture elements Ba and Sr. For these elements there are no data by 4AL; therefore, we just show our predictions, which have to be confirmed by future observations.

3.5 Predicted abundance gradients compared with other sets of data

We compare the results of our models with different sets of observational data, as described in Sect. 2.1.1 Only the data by Yong et al. (2006) refer to Cepheids. However, these data and 4AL data are not homogeneous because of the different way in which the abundances are derived. As a consequence of this, we apply the offsets calculated by Yong et al. (2006), on the basis of a representative sample of stars analyzed and measured by both authors, to compare the two sets of data. We compare the Cepheids and the Daflon & Cunha (2004) data for OB stars with the model predictions at the present time, normalized to the mean value at 8 kpc for the data by 4AL, whereas we compare observational data of red giants and open clusters with the model predictions at the solar formation time, normalized at the observed solar abundances by Asplund et al. (2005). In Table 3.4 we show the slopes of the

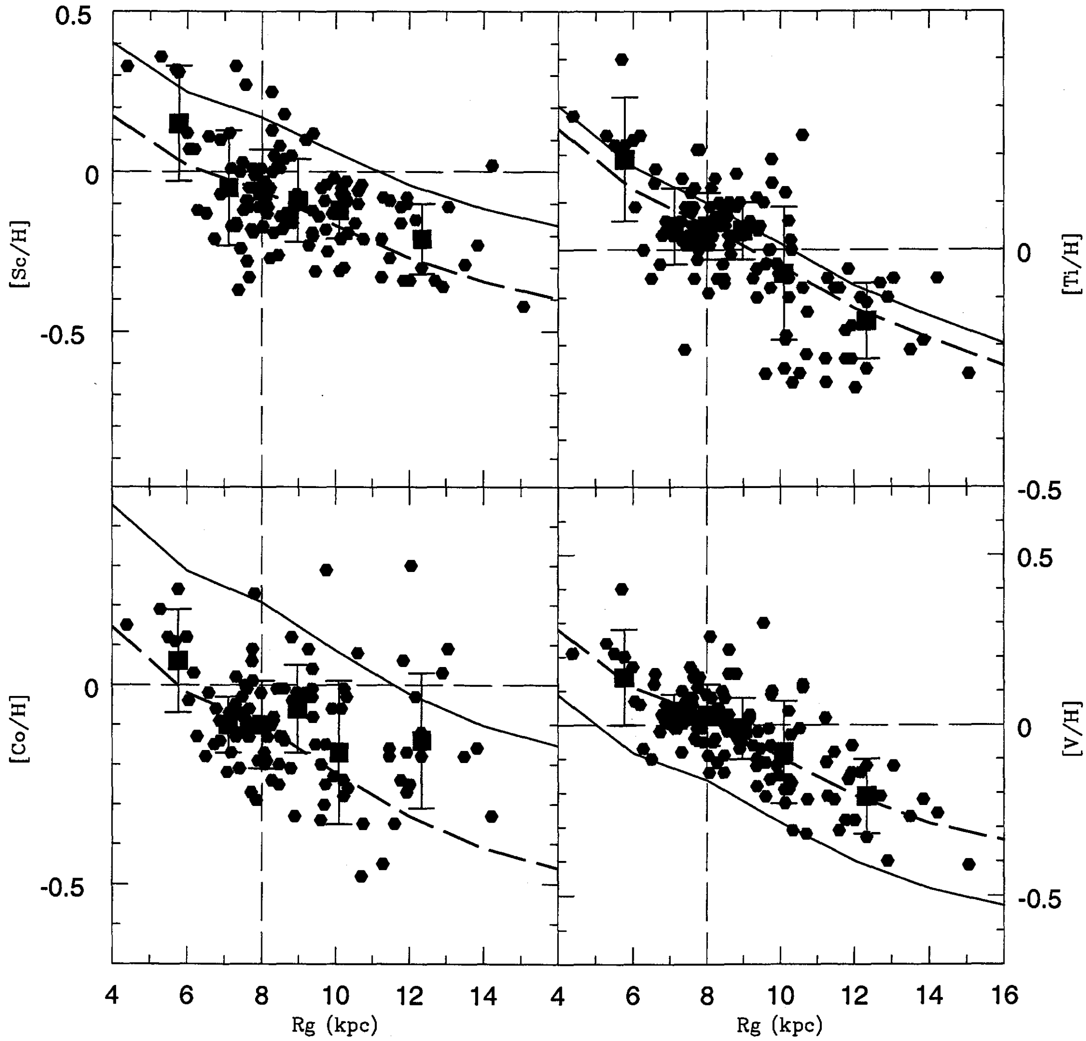

Figure 3.4. Gradients for [Sc/H], [Ti/H], [Co/H] and [V/H]. The models and the symbols are the same as in Fig. 3.2.

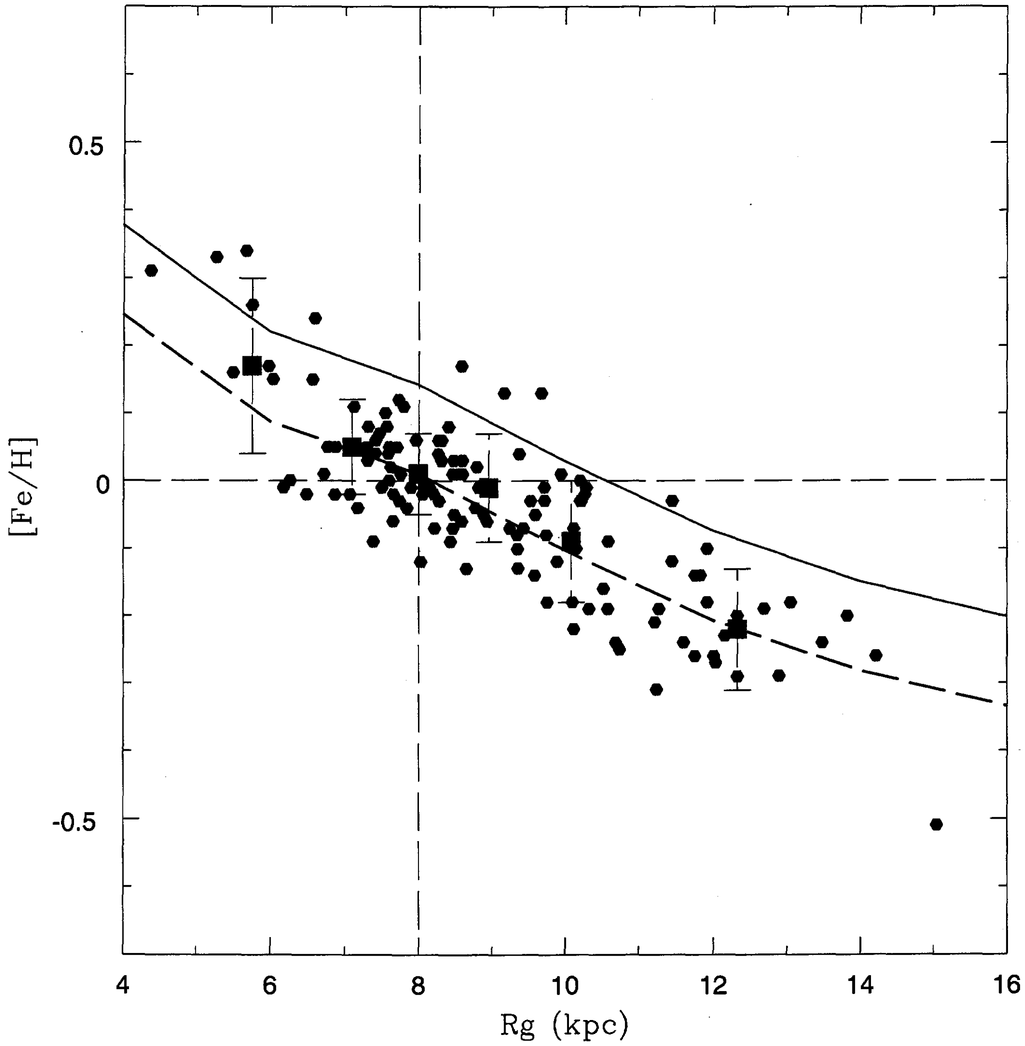

Figure 3.5. The gradient of [Fe/H]. The models and the symbols are the same as in Fig. 3.5.

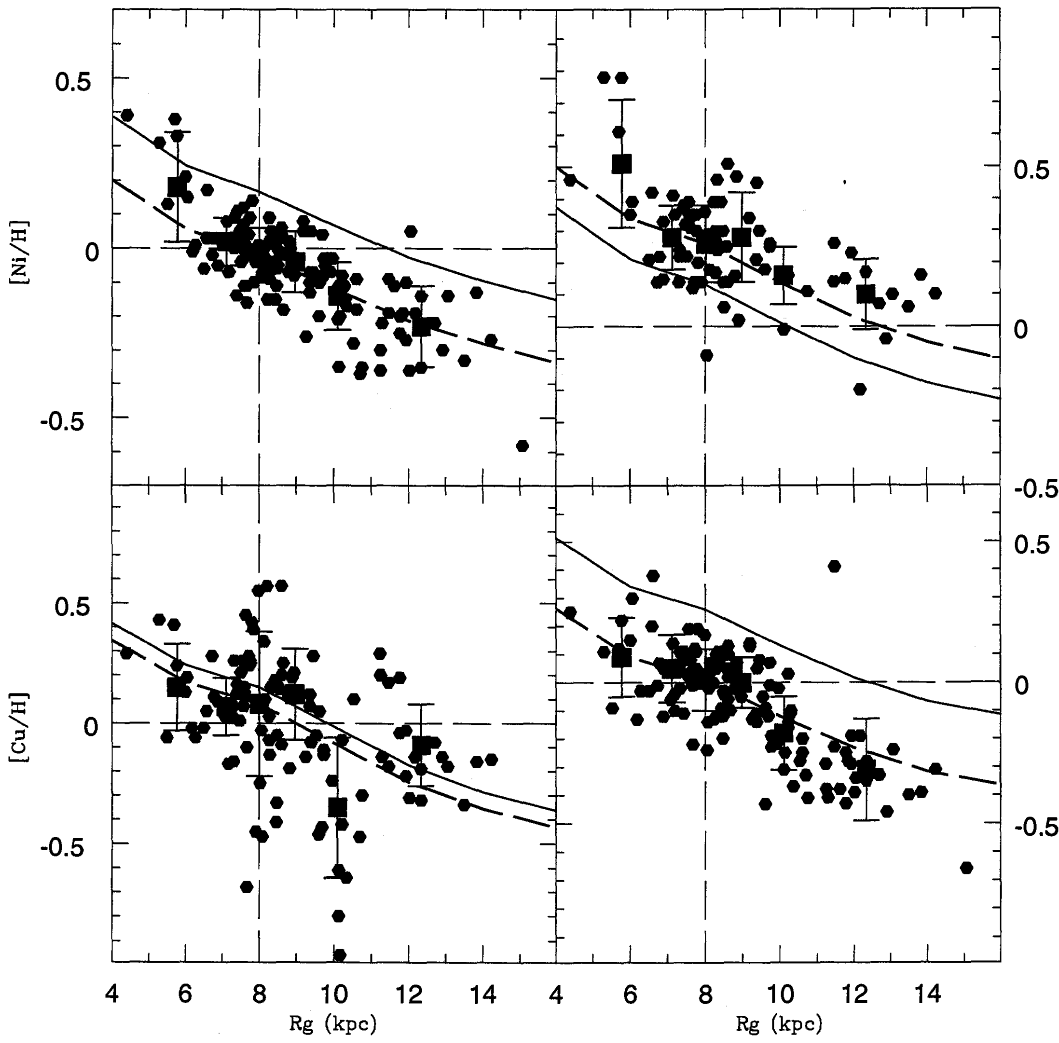

Figure 3.6. Gradients for [Ni/H], [Zn/H], [Cu/H]and [Mn/H]. The models and the symbols are the same as in Fig. 3.2.

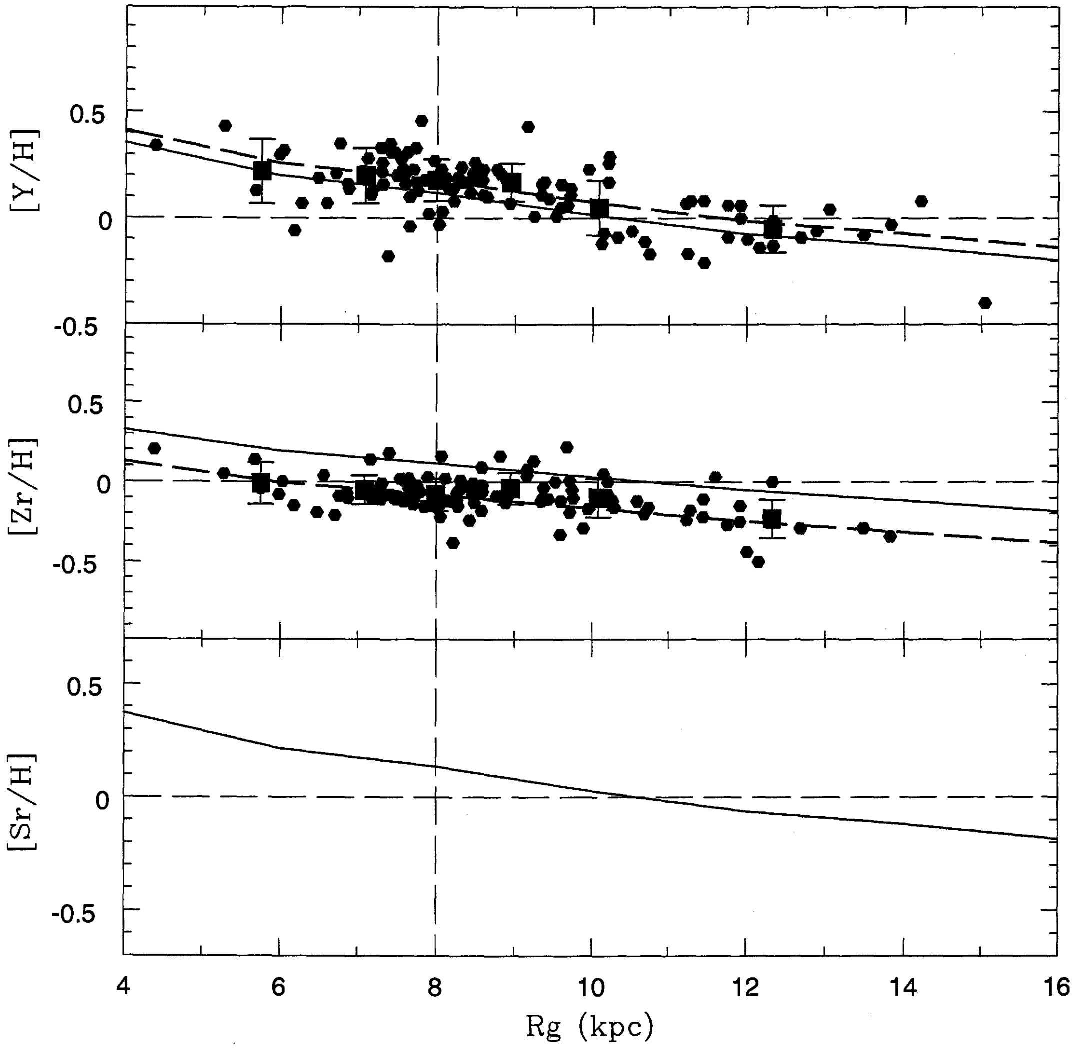

Figure 3.7. Gradients for [Sr/H], [Y/H], and [Zr/H]. The models and the symbols are the same as in Fig. 3.2. Note that for Sr we show only the model predictions.

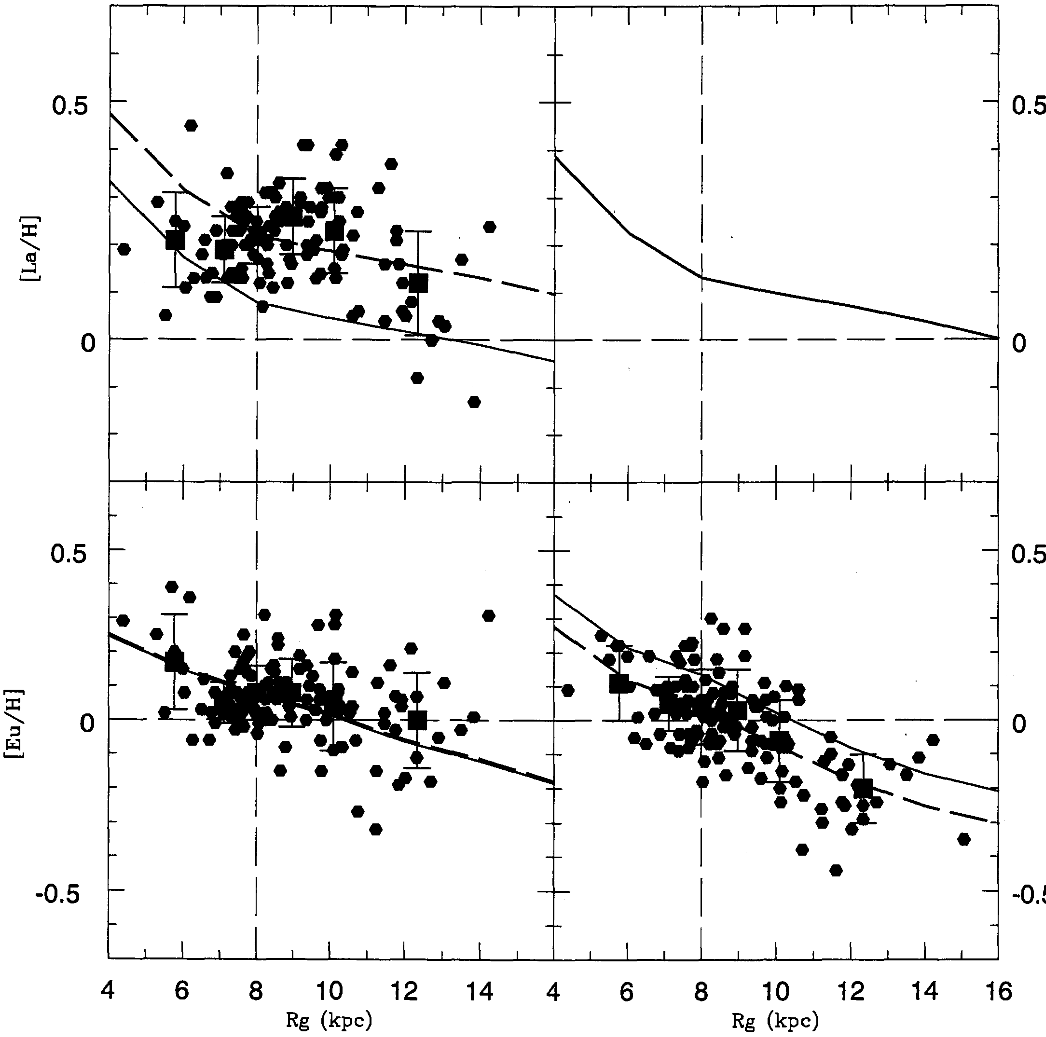

Figure 3.8. Gradients for [La/H], [Ba/H], [Cr/H] and [Eu/H]. The models and the symbols are the same as in Fig. 3.2. Note that for Ba we show only the model predictions.

Table 3.4. Model results for gradients at the solar formation time for each element. We show the gradients computed as a single slope, for all the range of galactocentric distance considered, and as two slopes: from 4 to 14 kpc and from 16 to 22 kpc.

	Fe	O	Mg	Si	S	Ca	Cu
$\frac{\Delta[el/H]}{\Delta R}(dex/kpc)$from 4 to 22 kpc	-0.027	-0.024	-0.026	-0.026	-0.026	-0.026	-0.038
$\frac{\Delta[el/H]}{\Delta R}(dex/kpc)$from 4 to 14 kpc	-0.036	-0.032	-0.033	-0.035	-0.035	-0.035	-0.052
$\frac{\Delta[el/H]}{\Delta R}(dex/kpc)$from 16 to 22 kpc	-0.016	-0.019	-0.019	-0.017	-0.017	-0.017	-0.018
	Zn	Ni	Sc	Ti	V	Cr	Mn
$\frac{\Delta[el/H]}{\Delta R}(dex/kpc)$from 4 to 22 kpc	-0.027	-0.026	-0.027	-0.026	-0.027	-0.027	-0.027
$\frac{\Delta[el/H]}{\Delta R}(dex/kpc)$from 4 to 14 kpc	-0.037	-0.035	-0.036	-0.034	-0.037	-0.036	-0.038
$\frac{\Delta[el/H]}{\Delta R}(dex/kpc)$from 16 to 22 kpc	-0.015	-0.018	-0.016	-0.018	-0.014	-0.016	-0.013
	Co	Sr	Y	Zr	Ba	Eu	La
$\frac{\Delta[el/H]}{\Delta R}(dex/kpc)$from 4 to 22 kpc	-0.027	-0.016	-0.026	-0.016	-0.020	-0.020	-0.022
$\frac{\Delta[el/H]}{\Delta R}(dex/kpc)$from 4 to 14 kpc	-0.037	-0.020	-0.033	-0.020	-0.016	-0.016	-0.019
$\frac{\Delta[el/H]}{\Delta R}(dex/kpc)$from 16 to 22 kpc	-0.014	-0.014	-0.021	-0.014	-0.010	-0.010	-0.013

gradients at the solar formation time for all the studied elements, as predicted by model B. The gradients generally tend to steepen with time (see Table 3.5). This behavior is expected in the model taking into account the inside-out formation of the disk, where the external disk regions are still forming now and the abundance gradient is still building up. In fact, at early epochs, the efficiency in the chemical enrichment of the inner Galactic regions is low (owing to the large amount of primordial infalling gas) leading to a flat initial abundance gradient. Then, at late epochs, while the SFR is still much higher in the central than in the external regions, the infall of metal poor gas is stronger in the outer than in the inner regions, thus steepening the gradients. An important role in this scenario is also played by the gas density threshold. In fact, the gas density threshold, stopping the SFR, tends to slow the chemical enrichment in the outskirts which have a lower gas density compare to the central regions.

Table 3.5. Model results for gradients for each element at three different time: 4.5 Gyr, 9.5 Gyr (solar formation time) and 14 Gyr (present time). We show the gradients computed as a single slope, for all the range of galactocentric distance considered.

	Fe	O	Mg	Si	S	Ca	Cu
4.5 Gyr	-0.012	-0.014	-0.014	-0.013	-0.013	-0.013	-0.015
9.5 Gyr	-0.027	-0.024	-0.026	-0.026	-0.026	-0.026	-0.038
14 Gyr	-0.036	-0.028	-0.031	-0.033	-0.034	-0.034	-0.050
	Zn	Ni	Sc	Ti	V	Cr	Mn
4.5 Gyr	-0.011	-0.013	-0.012	-0.014	-0.010	-0.012	-0.009
9.5 Gyr	-0.027	-0.026	-0.027	-0.026	-0.027	-0.027	-0.027
14 Gyr	-0.038	-0.034	-0.036	-0.032	-0.038	-0.036	-0.038
	Co	Sr	Y	Zr	Ba	Eu	La
4.5 Gyr	-0.010	-0.007	-0.015	-0.007	-0.005	-0.006	-0.011
9.5 Gyr	-0.027	-0.016	-0.026	-0.016	-0.020	-0.020	-0.022
14 Gyr	-0.037	-0.021	-0.030	-0.021	-0.032	-0.032	-0.031

3.5.1 α-elements (O-Mg-Si-S-Ca)

In Fig. 3.9 and 3.10, we show the comparison for O, Mg, Si, S and Ca data with our model. Although the observations are from completely different types of astronomical objects (OB stars, red giants, open clusters and Cepheids), they are in agreement with each other and with our model. Nevertheless, the data by Yong et al. (2006) and the data by Daflon & Cunha (2004) show a larger spread than the data by 4AL, in particular for Ca. The data by Carraro et al. (2004) for the open cluster Saurer 1 at the galactocentric distance of 18.7 kpc for all the considered elements, except Mg, are slightly above the predictions of our model.

3.5.2 The iron peak elements (Ti-Mn-Co-Ni-Fe)

We show the iron peak elements in Fig. 3.11 and 3.12. The data by Yong et al. (2005) seem to have a gradient in agreement with our model if we take into account some possible offset in the data, as considered by Yong et al. (2006). In particular, the abundances of Mn

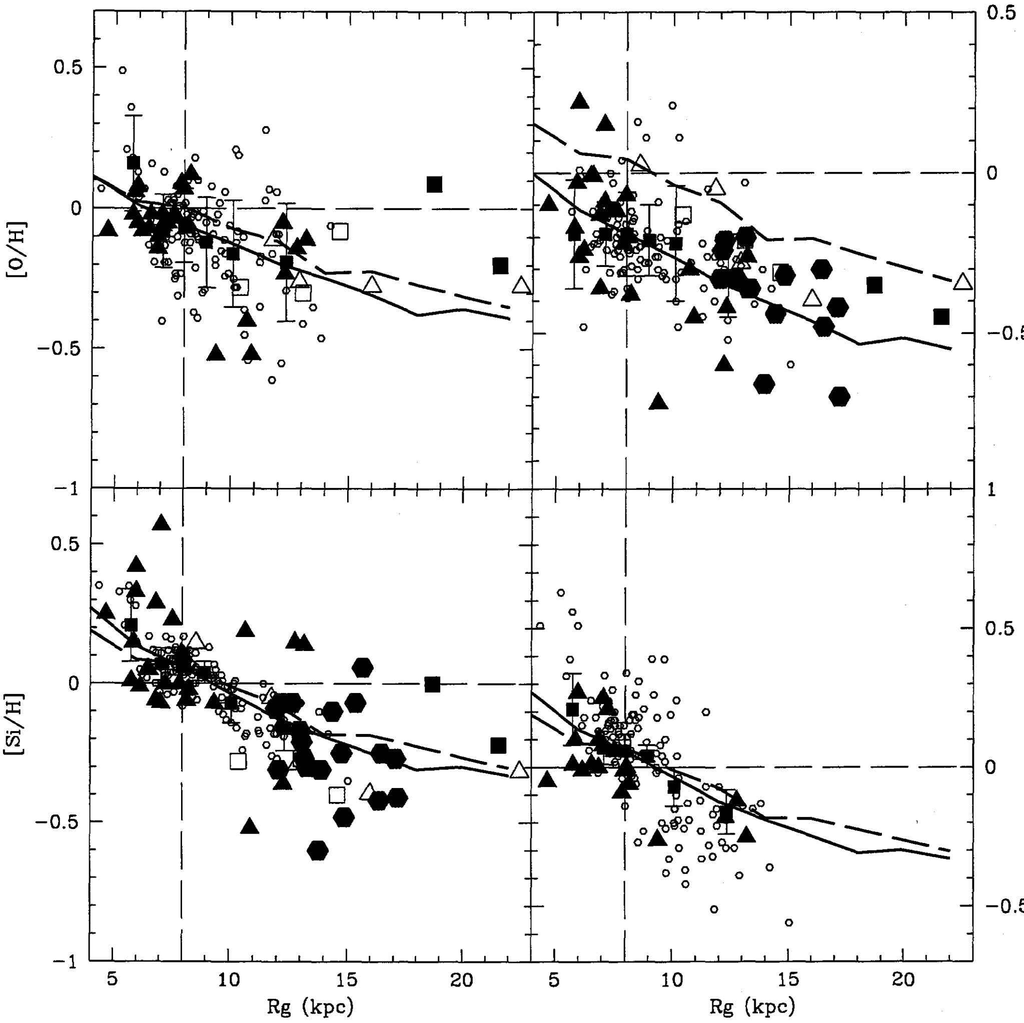

Figure 3.9. The gradients for O, Mg, Si and, S compared with different sets of data. The small open circles are the data by 4AL, the black squares are the mean values inside each bin for the data by 4AL and the error bars are the standard deviations (see table 3.2). The red solid triangles are the data by Daflon & Cunha (2004) (OB stars), the open blue squares are the data by Carney et al. (2005) (red giants), the blue solid hexagons are the data by Yong et al. (2006) (Cepheids), the blue open triangles are the data by Yong et al. (2005) (open clusters)and the magenta solid squares are the data by Carraro et al. (2004) (open clusters). The most distant value for Carraro et al. (2004) and Yong et al. (2005) refers to the same object: the open cluster Berkeley 29. The thin solid line is our model at the present time normalized to the mean value of the bin centered at 8 kpc for Cepheids stars by 4AL; the dashed line represents the predictions of our model at the epoch of the formation of the solar system normalized to the observed solar abundances by Asplund et al. (2005). This prediction should be compared with the data for red giant stars and open clusters (Carraro et al. 2004; Carney et al. 2005; Yong et al. 2005).

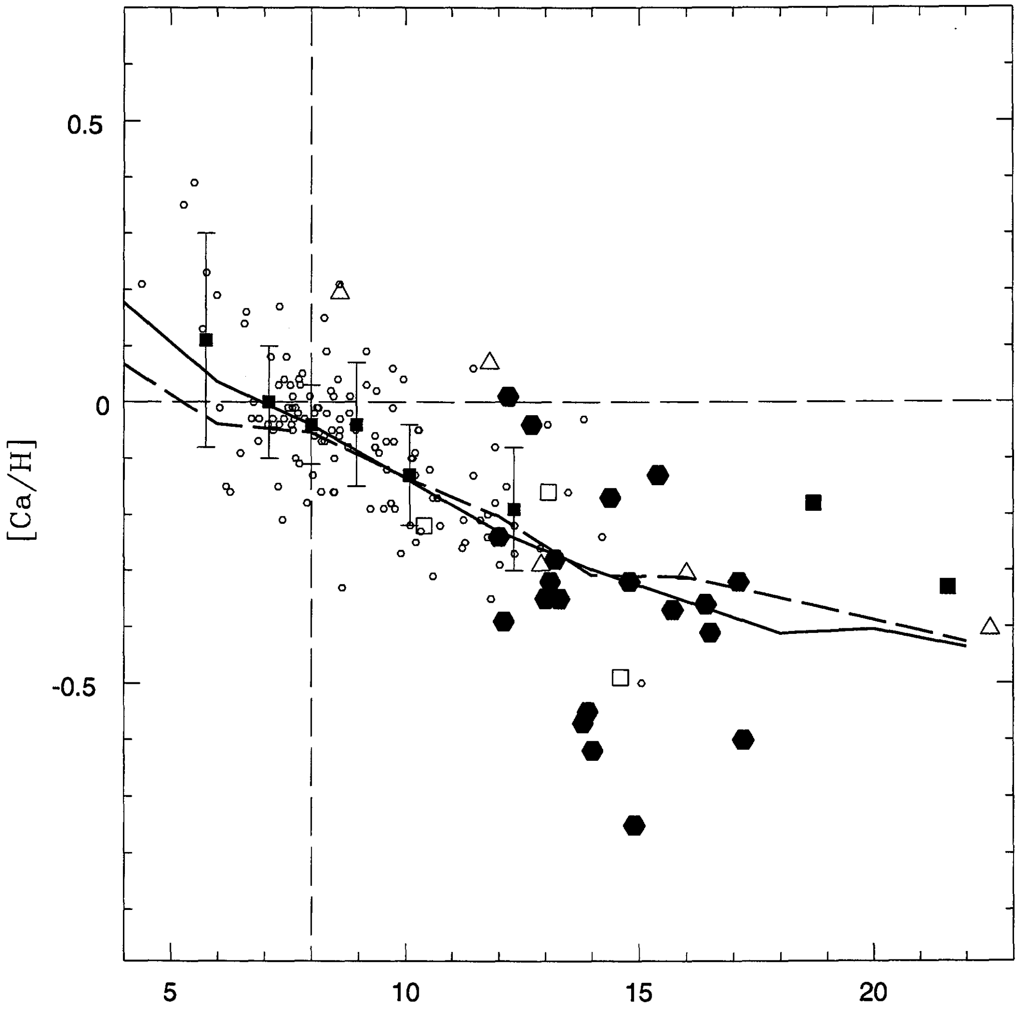

Figure 3.10. The gradient of Ca. The models and the symbols are the same as in Fig. 3.9.

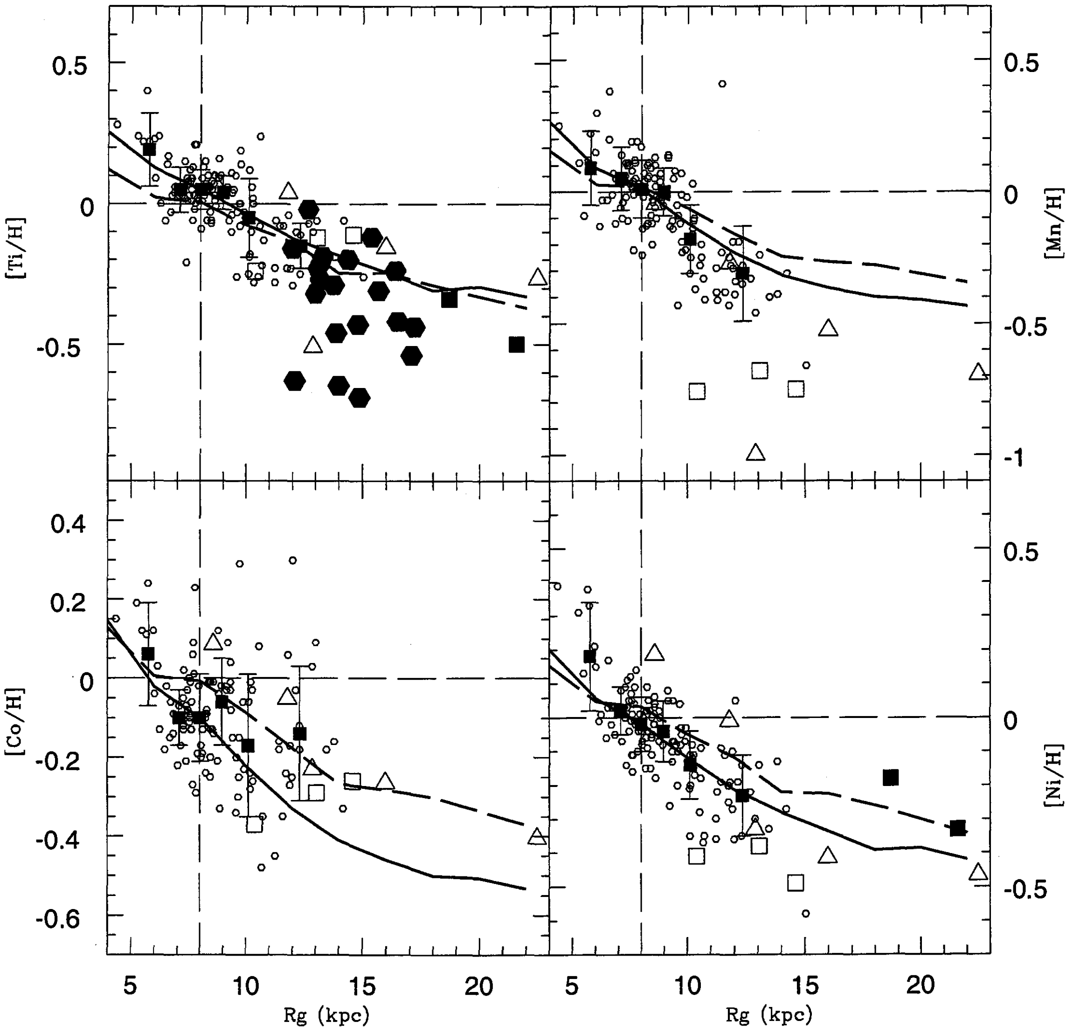

Figure 3.11. Gradients for Ti, Mn, Co and Ni. The model and the symbols are the same as in Fig. 3.9.

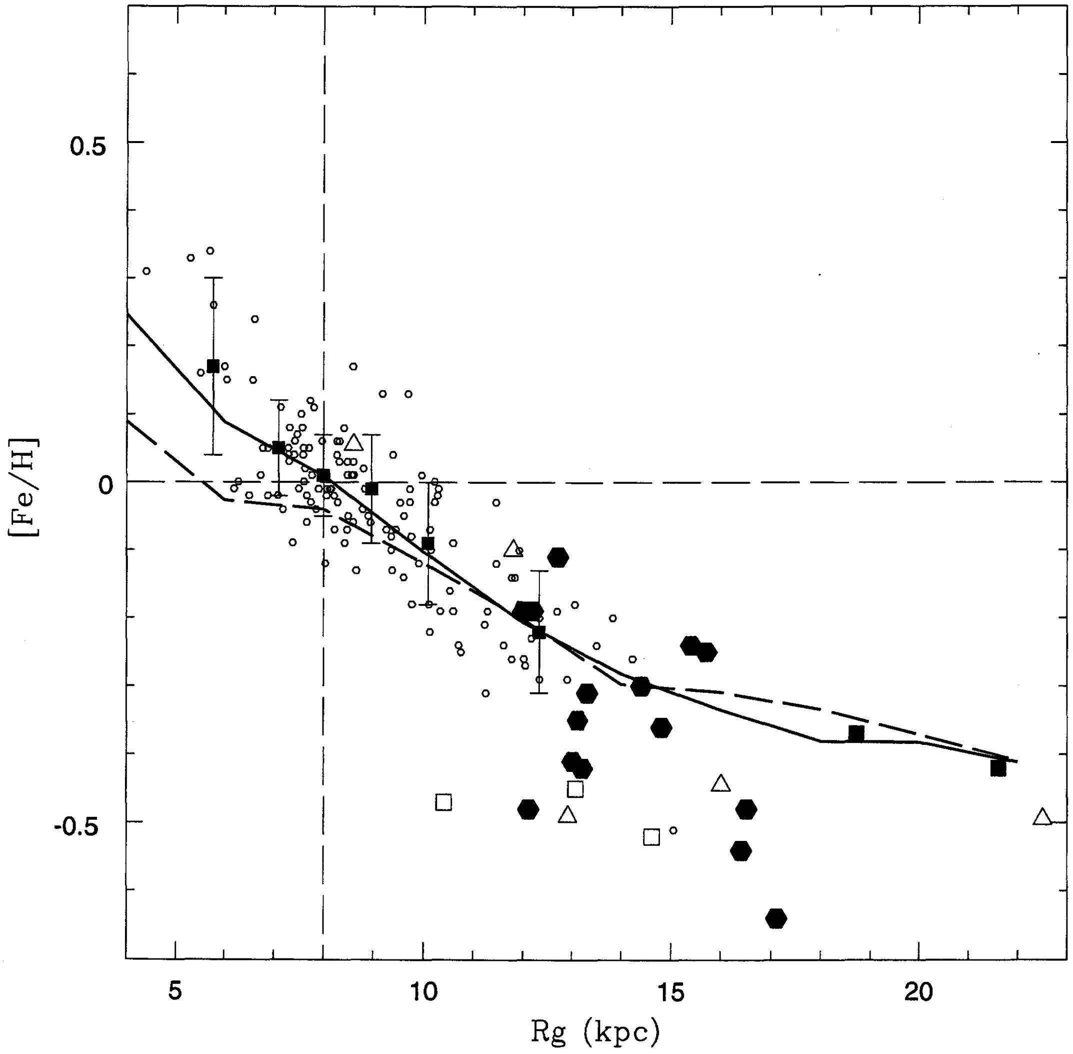

Figure 3.12. The gradient of Fe. The models and the symbols are the same as in Fig. 3.9.

in this data set are below our model predictions and the 4AL data. In the data by Yong et al. (2005), the open cluster Berkeley 31, which is at about 13 kpc, shows abundances lower than those predicted by our model and the set of data by 4AL for all the iron peak elements, with the exception of Co. On the other hand, the set of data by Carney et al. (2005) shows an almost flat trend and again lower abundances for the iron peak elements than the abundances of the data by 4AL and those predicted by the model. This is probably due to the fact that the data are from old and evolved objects, as giant stars are, with a not well estimated age. The data by Yong et al. (2006), which includes the abundances of Ti and Fe, are in agreement with our model and the data by 4AL, even if they seem to present slightly steeper gradients. The open cluster abundances as measured by Carraro et al. (2004) are in agreement with our model, in particular for Fe, whereas for Ti and Ni the model fits both open cluster abundances inside the error bars, which is about 0.2 dex.

3.5.3 The neutron capture elements (Zr-Ba-La-Eu)

We show the neutron capture elements in Fig. 3.13. The data for Eu are taken from the set of data by Yong et al. (2006, Cepheids), Yong et al. (2005, open clusters) and Carney et al. (2005, red giants), and they are in agreement with our model with the exception of a large spread in the data by Yong et al. (2006). Some problems arise for La. The trend of the gradients is similar for the sets of data but the absolute values of the La abundances in the sets of data by Yong et al. (2006), Yong et al. (2005) and Carney et al. (2005) are systematically lower od *sim* 0.3 dex than the ones of 4AL and, without the offset, it is impossible to make a comparison. Therefore, we apply an offset of +0.3 dex to all observational data (with the exception of the 4AL data) to better show all the sets of data. This can also be the consequence of the different way of calculating the abundances, as explained in Yong et al. (2006). The most important results are the slopes of the gradients rather than the absolute abundances. With this offset applied to the data, the two open clusters (Berkeley 31 and NGC 2141), measured by Yong et al. (2005), still present an abundance of La larger than the one predicted by our model and the mean abundance of the data by 4AL; finally, the data of Yong et al. (2006) again have a large spread. Nevertheless, the comparison is acceptable and the abundance of the most distant cluster is well fitted.

The results for Zr gradient at the solar time is in reasonable agreement with most of the open clusters data measured by Yong et al. (2005). The absolute abundances of the the data

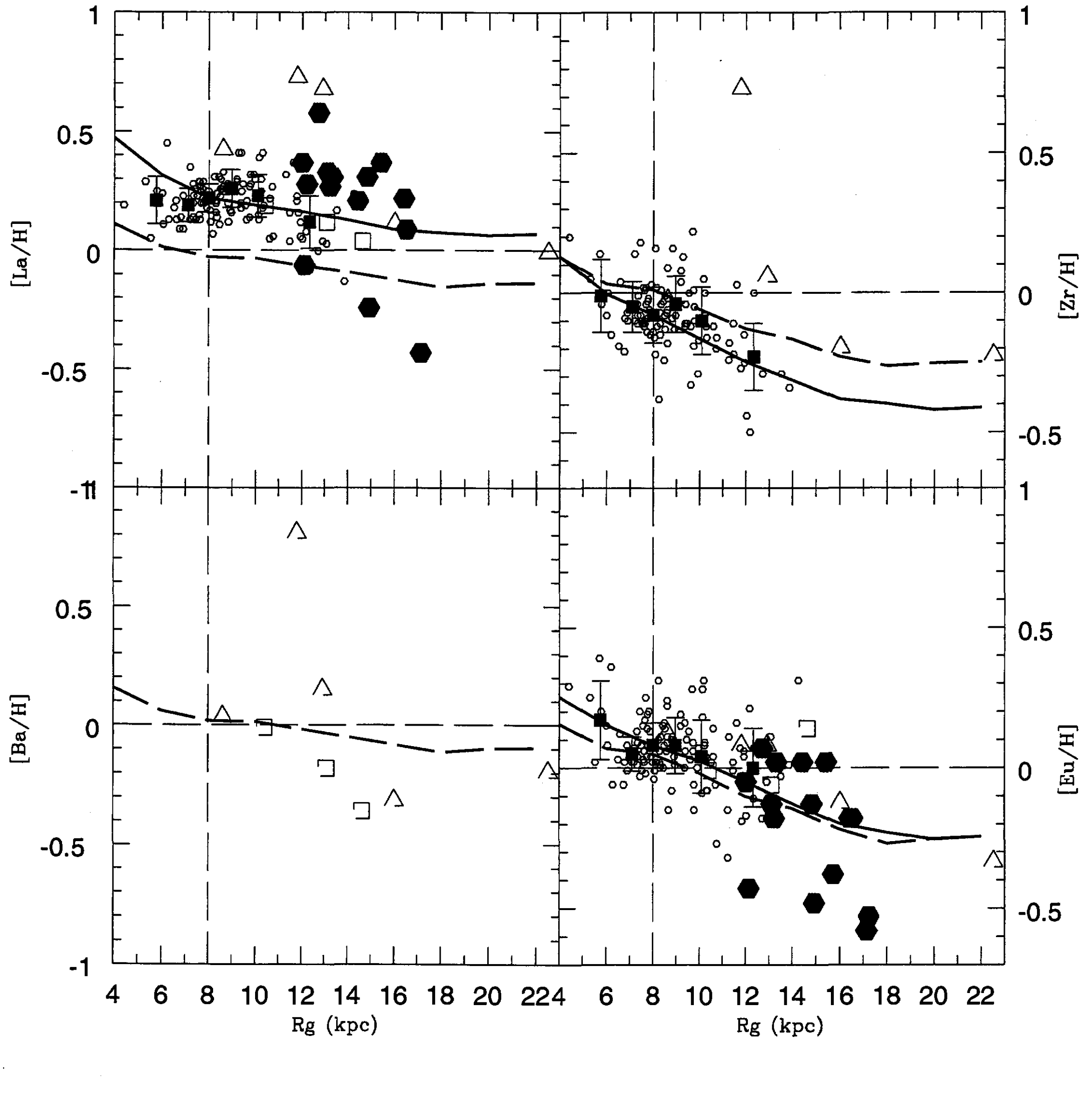

Figure 3.13. Gradients for La, Zr Ba and Eu. The model and the symbols are the same as in Fig. 3.9.

are just slightly larger than the model results for three clusters, whereas Berkeley 31 and NGC 2141 present again an abundance of Zr larger than the one predicted by our model. The results for Ba are similar to those for La. We have to apply an offset of +0.3 dex to the data by Carney et al. (2005), for the reasons explained above. The results are also quite good with the exceptions of the two open clusters mentioned before, which show a larger Ba abundance when compared to the results of our model. For both these open clusters there is only one measured star and it is possible that the stars chosen to be analyzed could be peculiar in terms of chemical abundances of s-process elements and so they should not be considered in deriving the gradients.

The data in the outer parts of the disk are still insufficient to completely constrain our models. Moreover, the existing samples show scatter. Two factors can affect the abundance gradients in the outer parts: observational uncertainties in both abundances and distance, and the fact that the outer parts could reflect a more complex chemical evolution. Moreover, there are some suggestions that the open clusters and giants in the outer part of the disk could have been accreted. However, despite these uncertainties, our chemical evolution model, where the halo density is assumed constant with radius out to $\sim$ 20 kpc, predicts abundance gradients in agreement with those measured in the outer disk.

Chapter 4

Inhomogeneous model for the Galactic halo: a possible explanation for the spread observed in s- and r-process elements

> *"There are mysteries which men can only guess at,*
> *which age by age they may solve only in part."*
> *by Bram Stoker*

The neutron capture elements observed in low metallicity stars in the solar vicinity show a large spread, compared to the small star to star scatter observed for the α-elements. In chapter 2 we have tried to explain this spread by means of different stellar yields for stars with the same mass, in the framework of a homogeneous model. In this chapter we show the results of a stochastic chemical evolution model that we have developed in order to explain the spread, following the suggestion of McWilliam et al. (1995).

4.1 Observational data

In this section we consider also the $\alpha - elements$ and not only the r-s process elements. For the extremely metal poor stars (-4<[Fe/H]< -3), we adopted the recent results from UVES

Large Program "First Star" (Cayrel et al. 2004, François et al. 2007). For the abundances in the remaining range of [Fe/H], we took published high quality data in the literature from various sources: Beers et al. (1999), Burris (2000), Carney et al. (1997), Carretta et al. (2002), Cowan et al. (2005), Edvardsson et al. (1993), Fulbright (2000, 2002), Gilroy et al. (1998), Gratton and Sneden (1988, 1994), Honda et al. (2004), Ishimaru et al. (2004), Johnson (2002), Koch & Edvardsson (2002), Mashonkina & Gehren (2000, 2001), McWilliam et al. (1995), McWilliam & Rich (1994), Nissen and Schuster (1997), Pompeia et al. (2003), Prochaska et al. (2000), Ryan et al. (1991, 1996), Stephens (1999) and Stephens & Boesgaard (2002).

4.2 Inhomogeneous chemical evolution model for the Milky Way halo

We model the chemical evolution of the halo of the Milky Way for the duration of 1 Gyr. We consider that the halo has formed by means of the assembly of many independent regions each with a typical volume of $10^6 pc^3$. Each region does not interact with the others. Inside each region the mixing is assumed to be instantaneous. In each region we assume an infall episode with a timescale of 1Gyr and a threshold in the gas density for the star formation. We assume a timestep of 1 Myr. When the threshold density is reached, the mass of gas which is transformed at each timestep in to stars, M^{new}_{stars}, is assumed to be proportional to $\rho^{1.5}_{gas}$. We stop the star formation in each region when the total mass of the newly formed stars exceeds M^{new}_{stars}. The mass of each star is assigned with a random function in the range between 0.1 and 80 $M_{\odot}$, weighted according to the IMF of Scalo (1986). In this way, in each region, at each timestep, the M^{new}_{stars} is the same but the total number and the masses of the stars are different. At the end of its life, each star enriches the gas with newly produced elements (see the next section), as a function of its mass and metallicity. We calculate the cooling timescale for SN bubbles in our environment at different times. We found that the cooling timescale is always smaller than the typical timestep of our simulation, so we decided to neglect this delay time and the mixing in each simulated box is instantaneous. The stellar lifetime is calculated as a function of the stellar mass, as described in the previous chapters. The model does not take in account the pollution produced by stars with mass $< 3M_{\odot}$ because their lifetimes exceed the time considered in the model.

The existence of SNeIa is also taken into account, according to the prescriptions of Matteucci & Greggio (1986) In figure 4.1, the SNeIa rate is compared to the SNeII rate. Due to the threshold in the gas density that we impose, the star formation starts only after 250 Myr and at this stage the first SNeII start to explode. With a time delay of about 30Myr the first SNeIa take place. In our model we consider the single degenerate scenario and 30Myr is the shortest timescale for a SNIa to explode, being the lifetime of the most massive progenitor leading to the formation of a C-O white dwarf. We stop the star formation at 1 Gyr and the SNeII rate fall abruptly to zero, correctly, being the longest lifetime of a SNII 30Myr, whereas the SNeIa continue to explode, being the lifetime of the progenitors of a SNIa as long as 10 Gyr.

The model follows the chemical evolution of more than 20 elements in each region. The model parameters of the chemical evolution (SFR, IMF, stellar lifetime, nucleosynthesis, gas threshold), are the same as those used in chapter 2 for the homogeneous model. If the model is correct, our predictions will approximate the results of the homogeneous model as the number of stars increases. On the other hand, our model shows the spread that can be produced by different nucleosynthesis sites on the chemical enrichment at low metallicity, where the number of stars is low and the random effects in the birth of stellar masses can be important.

4.3 Nucleosynthesis Prescriptions

For the nucleosynthesis prescriptions of the Fe and the others elements (namely O, S, Si, Ca, Mg, Sc, Ti, V, Cr, Zn, Cu, Ni, Co and Mn), we adopted those suggested by François et al. (2004) both for single stars and SNeIa, as we did in chapter 2. We underline that the site of production of α-elements and of Fe is the whole range of massive stars. For the nucleosynthesis prescriptions of the r-process contribution we used those of model 1 for Ba and Eu (see chapter 2.1), the results of chapter 2.2 for La and the results of the chapter 2.3 for Sr, Y and Zr. These empirical yields have been chosen in order to reproduce the surface abundances for all these neutron capture elements in low metallicity stars as well as the Sr, Y, Zr, Ba, Eu and La solar abundances, taking in account the s-process contribution at high metallicities by means of the yields of Busso et al. (2001) for lanthanum and barium and those of Travaglio et al. (2004) for strontium, yttrium and zirconium in the mass range

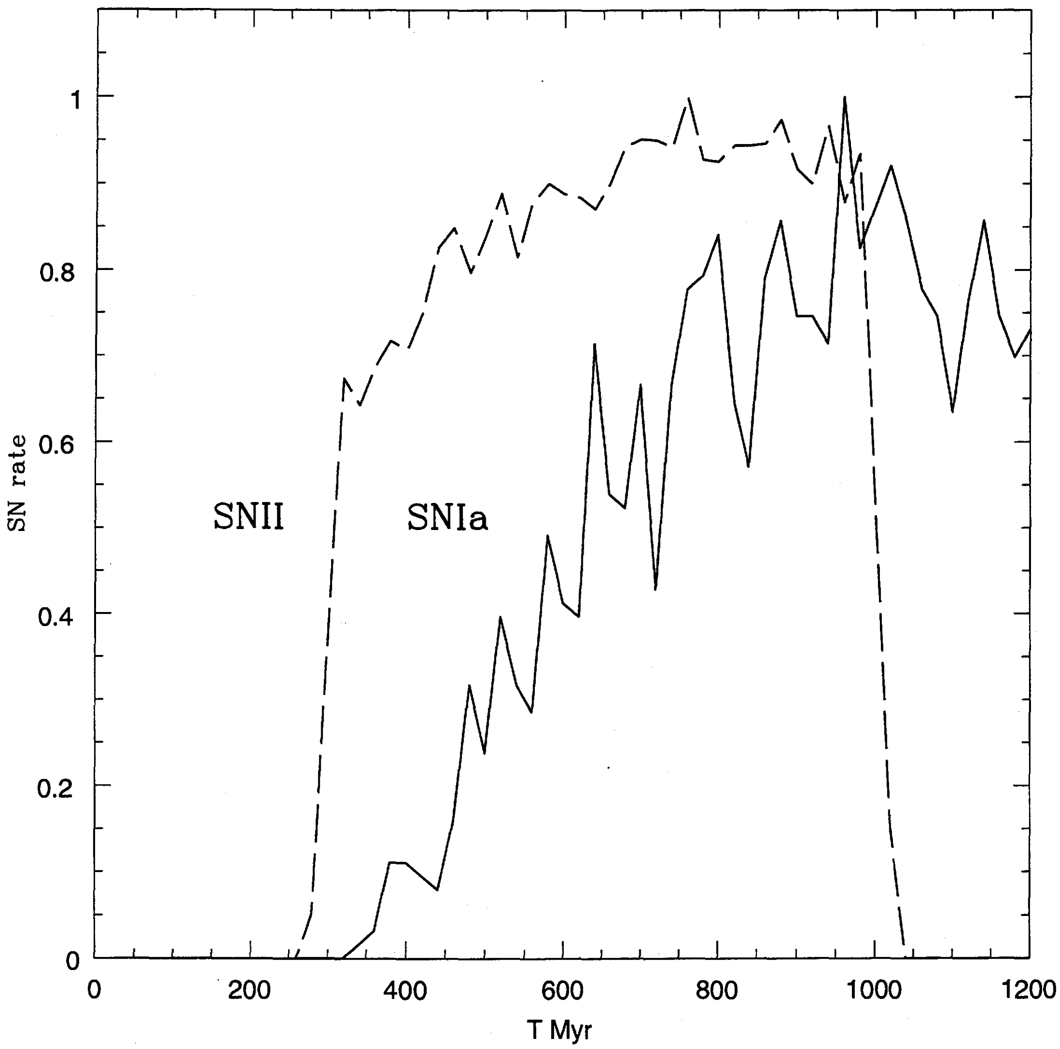

Figure 4.1. The SNIa rate (red line) and SNII rate (blue line) in the halo. They are normalized to their maximum values.

1.5-3$M_\odot$. We have assumed that Sr, Y, Zr Ba and La are produced as r-process elements by massive stars but only up to 30 $M_\odot$ and Eu is also considered to be a purely r-process element produced in the same range of masses.

4.4 Results

4.4.1 The ratios of α-elements and neutron capture elements to Fe

We discuss here the results of our simulations compared to the observational data and to the prediction of the homogeneous model. We show the [Eu/Fe], [Ba/Fe], [La/Fe], [Sr/Fe], [Y/Fe] and [Zr/Fe] ratios as a function of [Fe/H] in the figures 4.2, 4.3, 4.4, 4.5, 4.6, 4.7, respectively; for α-elements we show [Si/Fe], [Ca/Fe] and [Mg/Fe] as a function of [Fe/H] in figures 4.8, 4.9, 4.10, respectively.

Our aims is to explain how this model reproduces the large spread in the abundances of metal poor stars for the neutron capture elements and, at the same time, the small spread for the α-elements. The chemical enrichment observed in metal poor stars is due to nucleosynthesis in the massive stars. The sites of production in massive stars for the α-elements and neutron capture elements are different (as described in the previous section): the α-elements and Fe are produced in the whole range of massive stars; the neutron capture elements are produced only up to 30 $M_\odot$. Therefore, in regions with many stars less massive than 30 $M_\odot$, the ratio of neutron capture elements over Fe is high. The opposite happens in regions where most of the stars are more massive than 30 $M_\odot$. This fact produces, in our inhomogeneous model, a large spread for the rates of neutron capture elements to Fe, but not for the ratio of the α-elements to Fe, since the α-elements and Fe are produced in the same range.

In the figures 4.11, 4.12, we show the relative frequency of stars at a given [El/Fe] ratio for different enrichment phases. To calculate these frequencies, we have used only the stars which still exist nowadays in the halo, those with a mass $< 0.8M_\odot$. The different enrichment phases: $[Fe/H] < -3$, $-3 < [Fe/H] < -2$ and $-2 < [Fe/H] < -1$ are given in the panels from top to bottom for Si and Eu. In these figures the black lines are the predictions of the model and the red lines are the observational data. At intermediate metallicity, the model predicts for the Si already a quite narrow distribution, whereas for Eu the distribution of the stars is broad, in agreement with the observations. At higher metallicities both elements have predicted distributions narrower than the observed ones and this could be explained

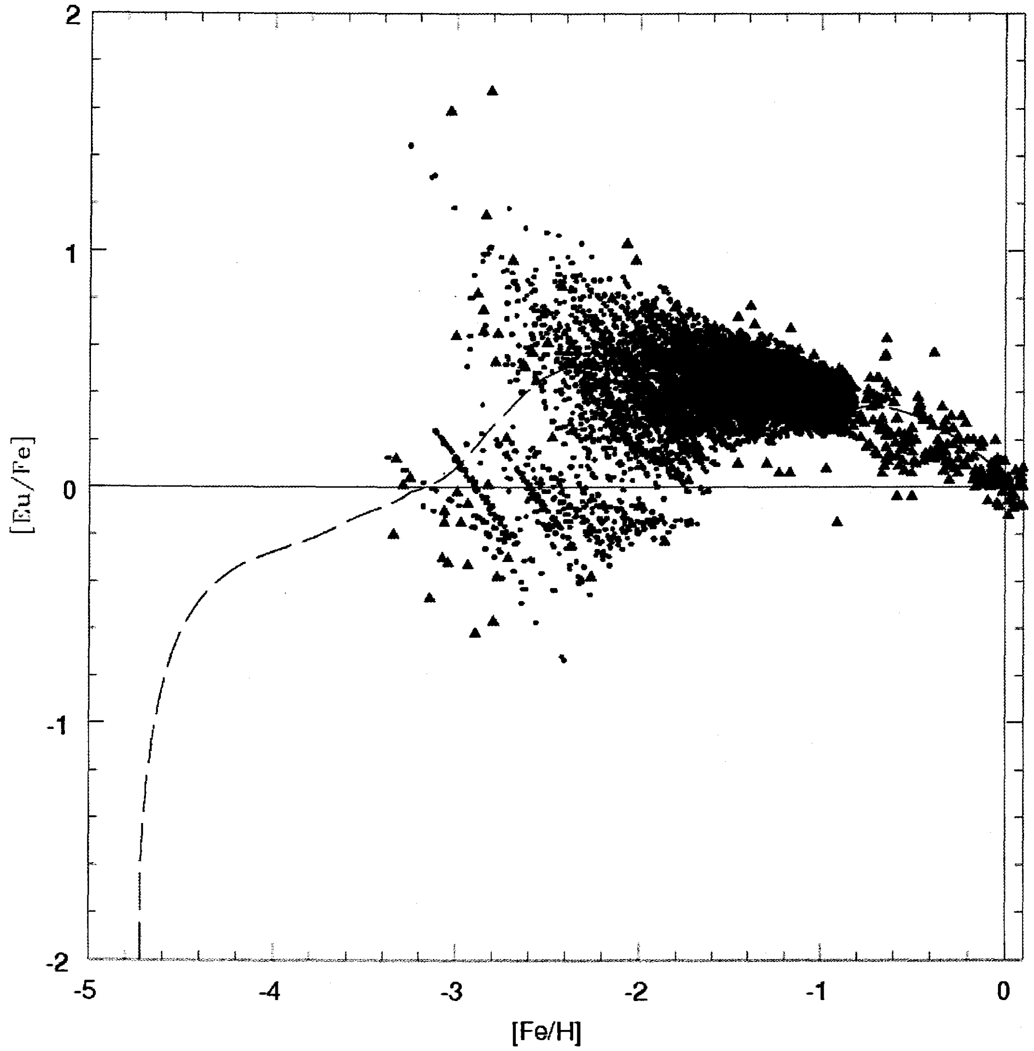

Figure 4.2. [Eu/Fe] vs [Fe/H]. The abundances of simulated stars are indicated by the blue dots, the observational data by the red triangles. The black line is the prediction of the homogeneous model.

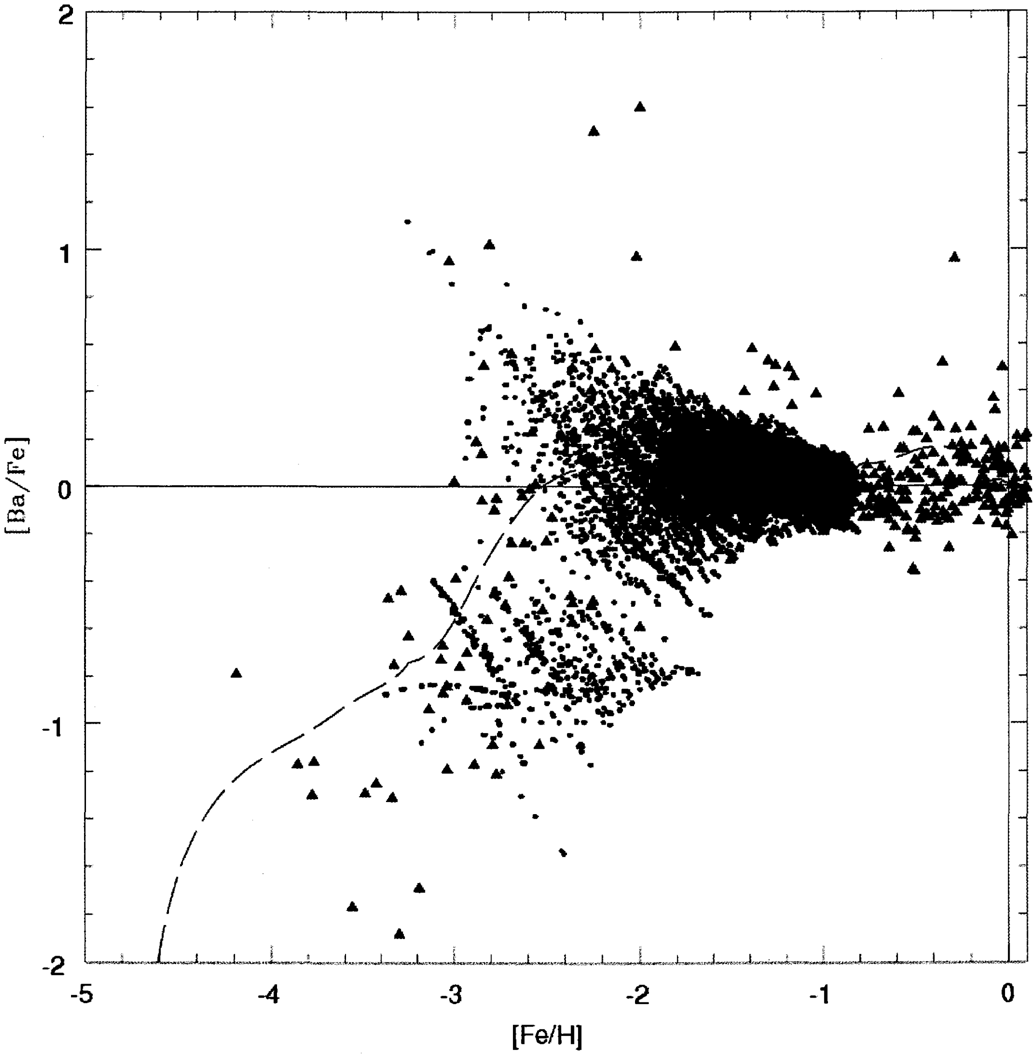

Figure 4.3. As in figure 4.2 but for [Ba/Fe].

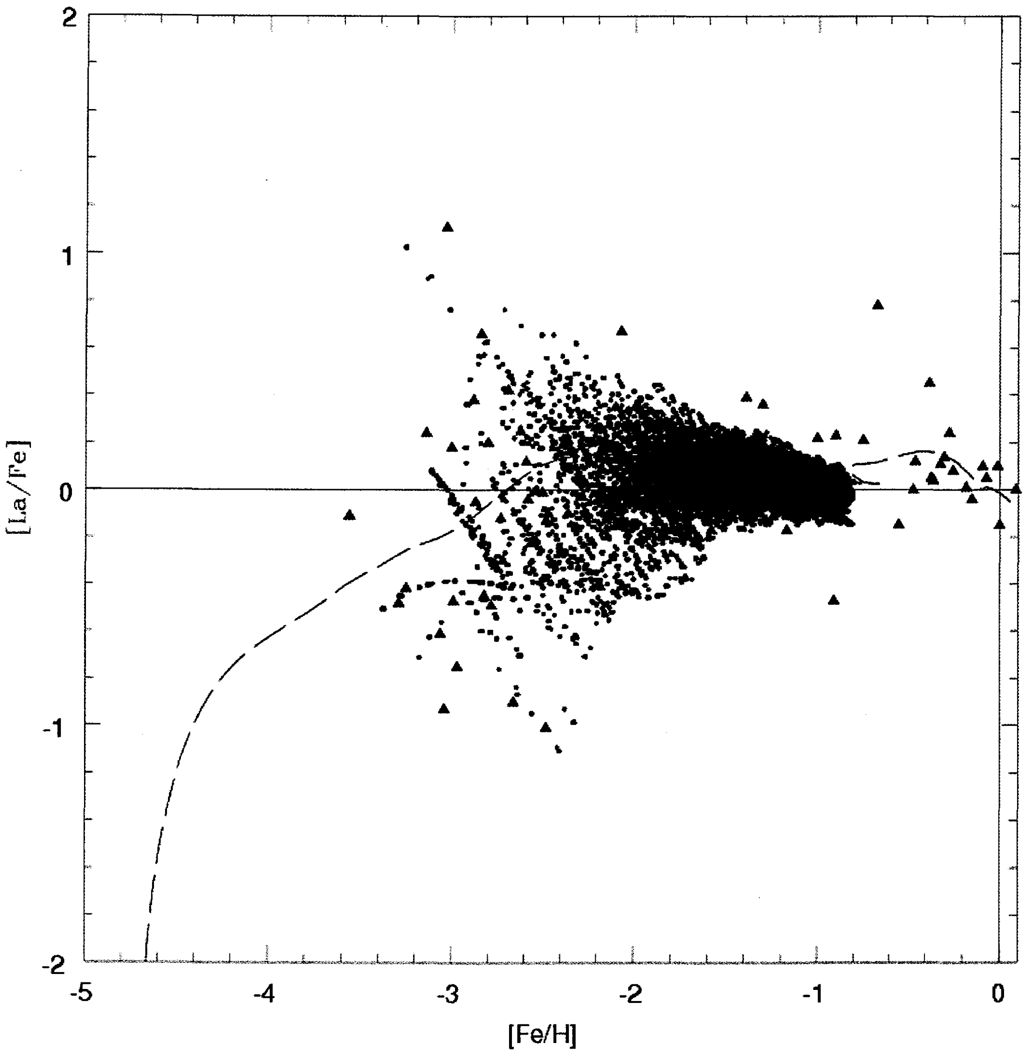

Figure 4.4. As in figure 4.2 but for [La/Fe].

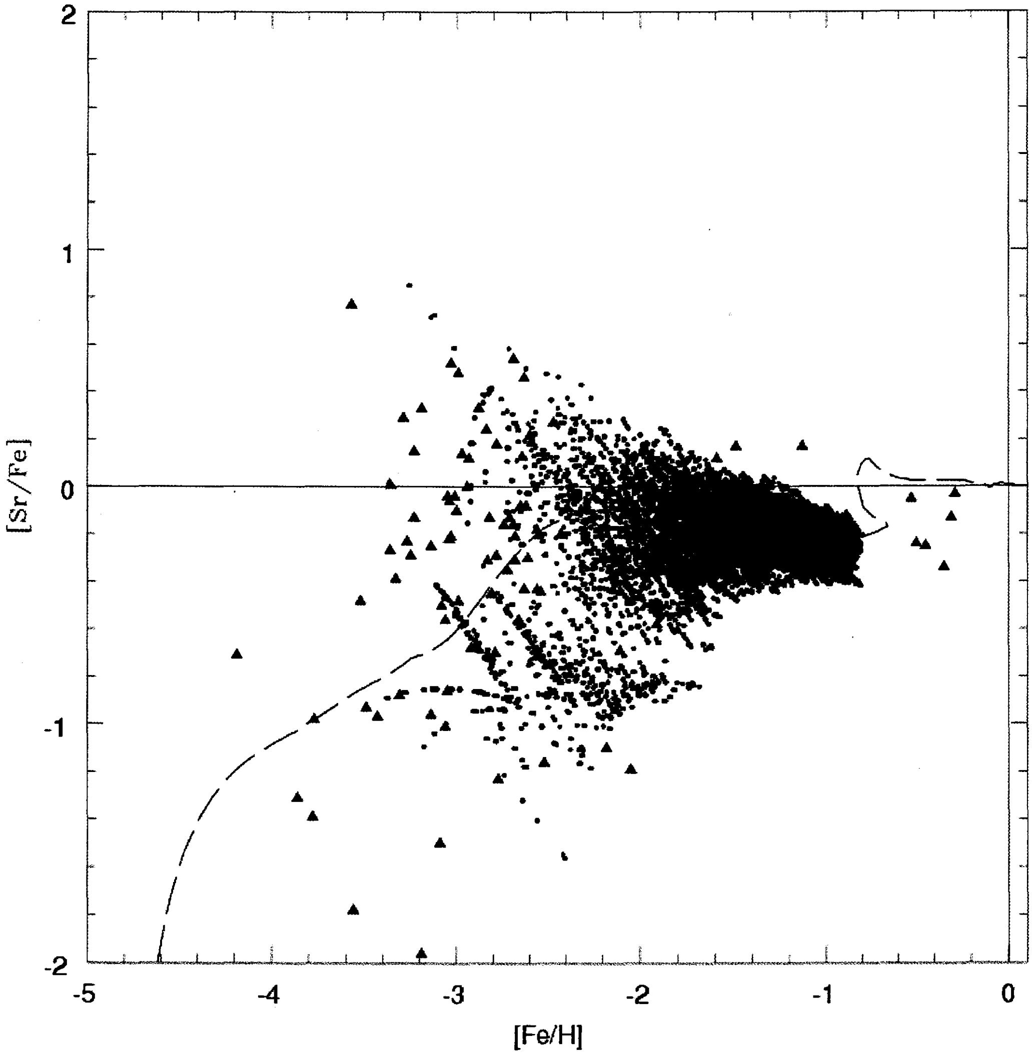

Figure 4.5. As in figure 4.2 but for [Sr/Fe].

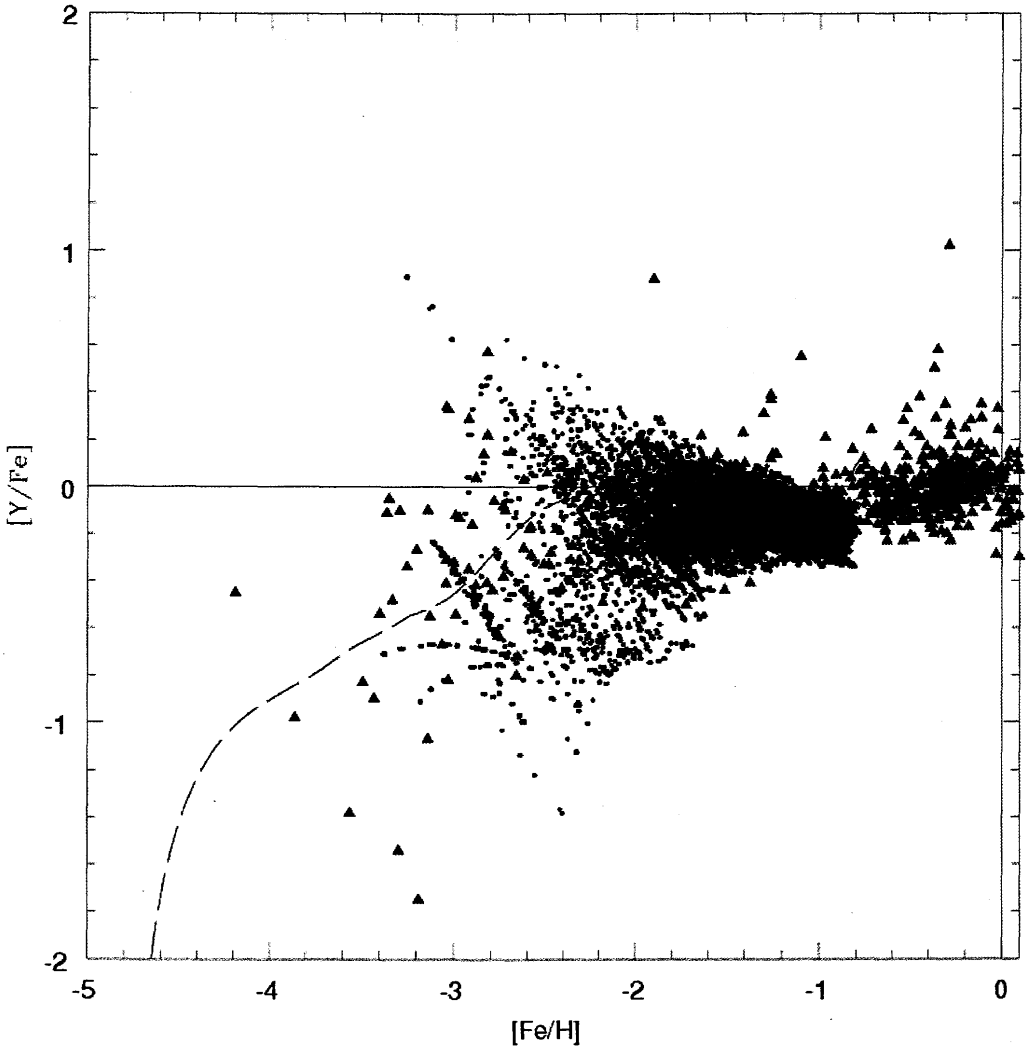

Figure 4.6. As in figure 4.2 but for [Y/Fe].

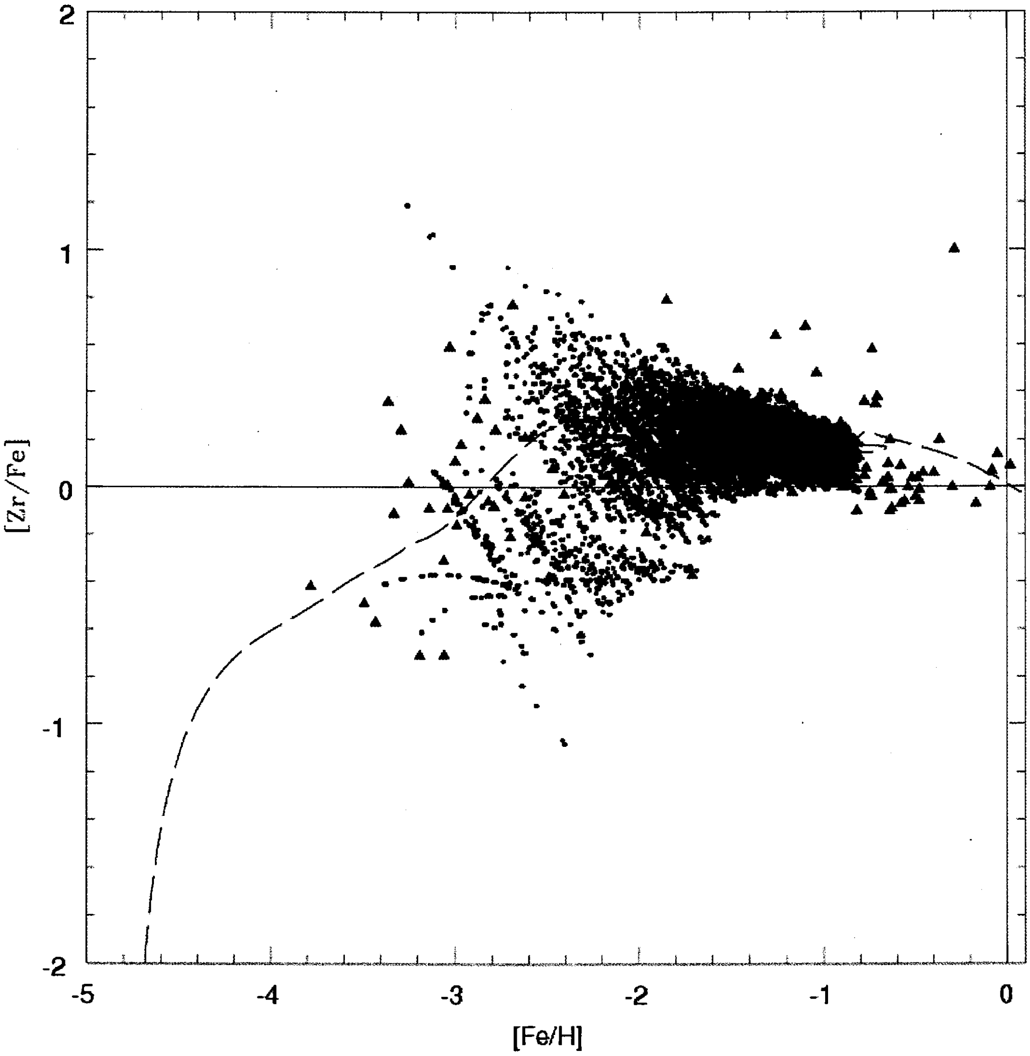

Figure 4.7. As in figure 4.2 but for [Zr/Fe].

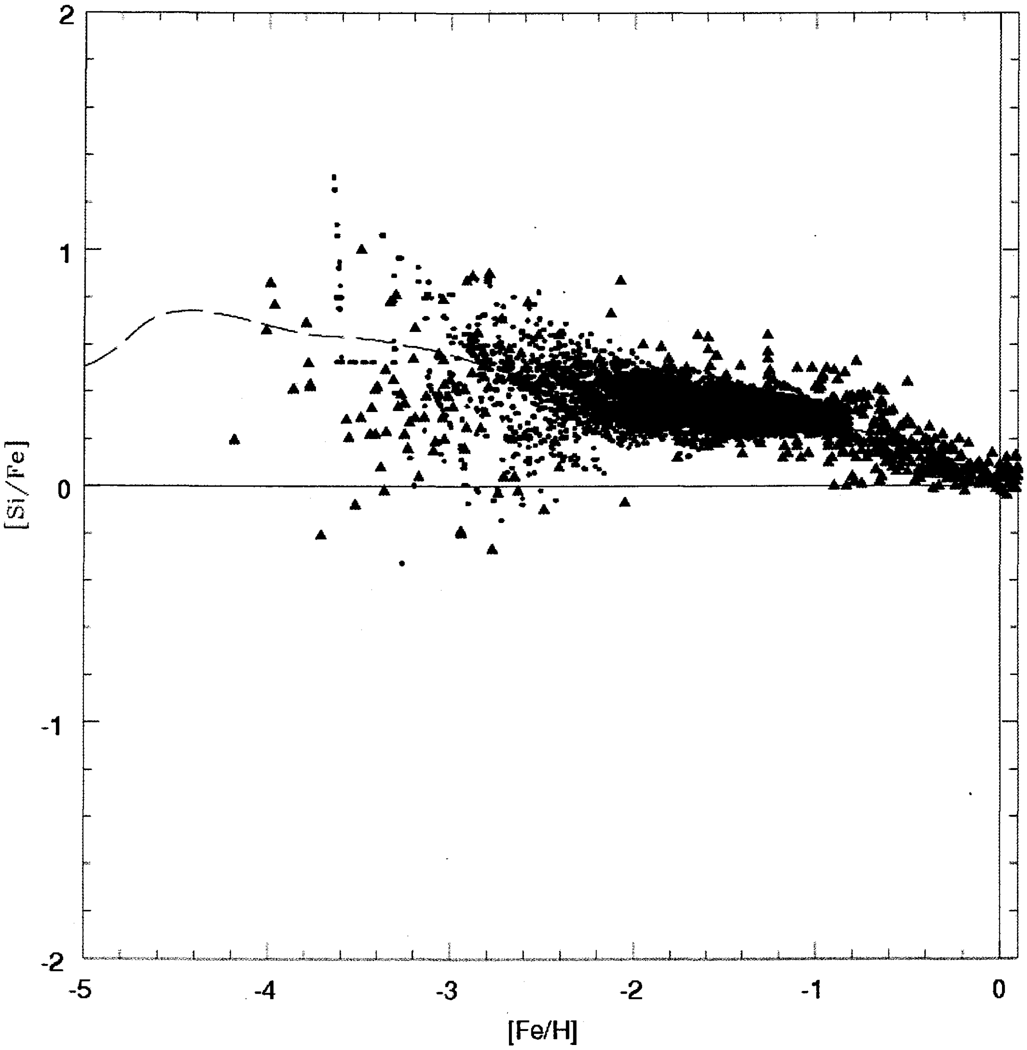

Figure 4.8. As in figure 4.2 but for [Si/Fe].

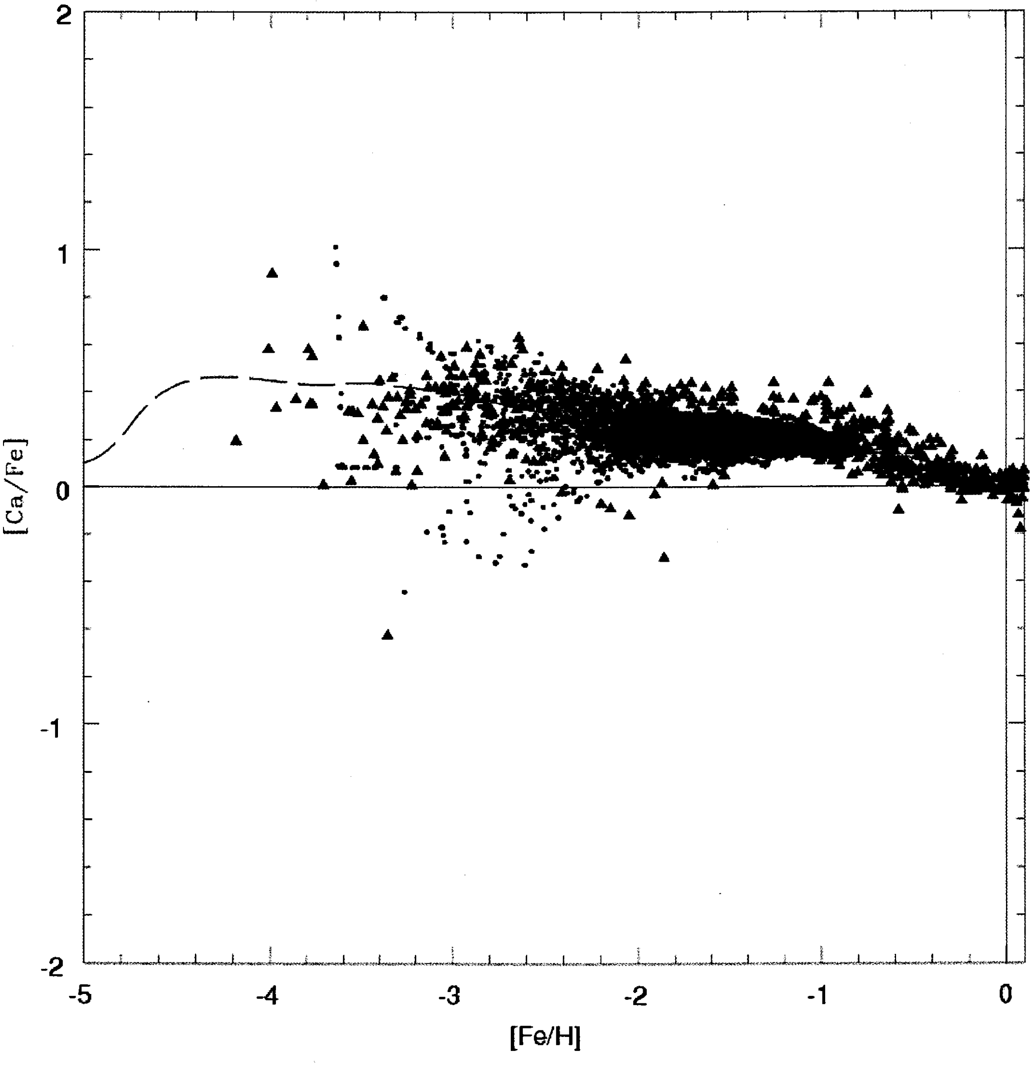

Figure 4.9. As in figure 4.2 but for [Ca/Fe].

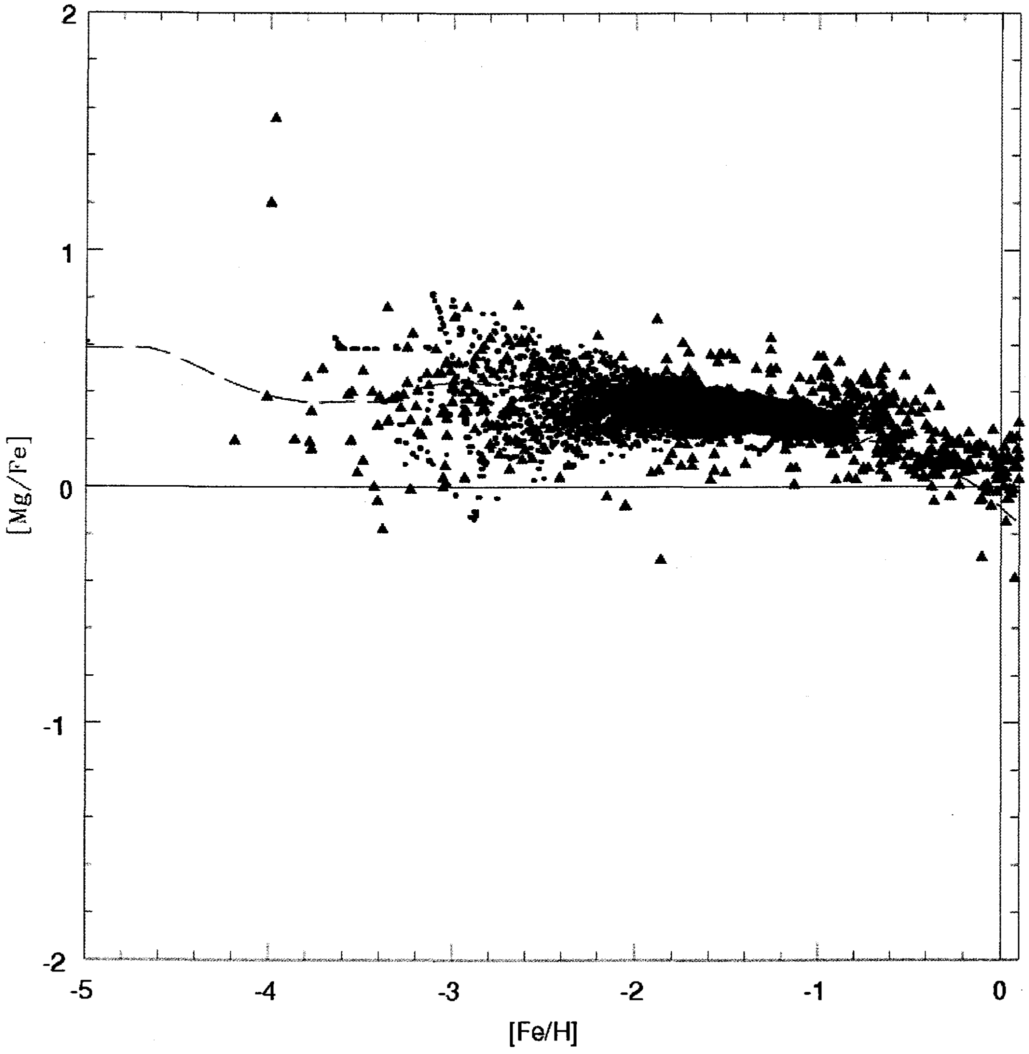

Figure 4.10. As in figure 4.2 but for [Mg/Fe].

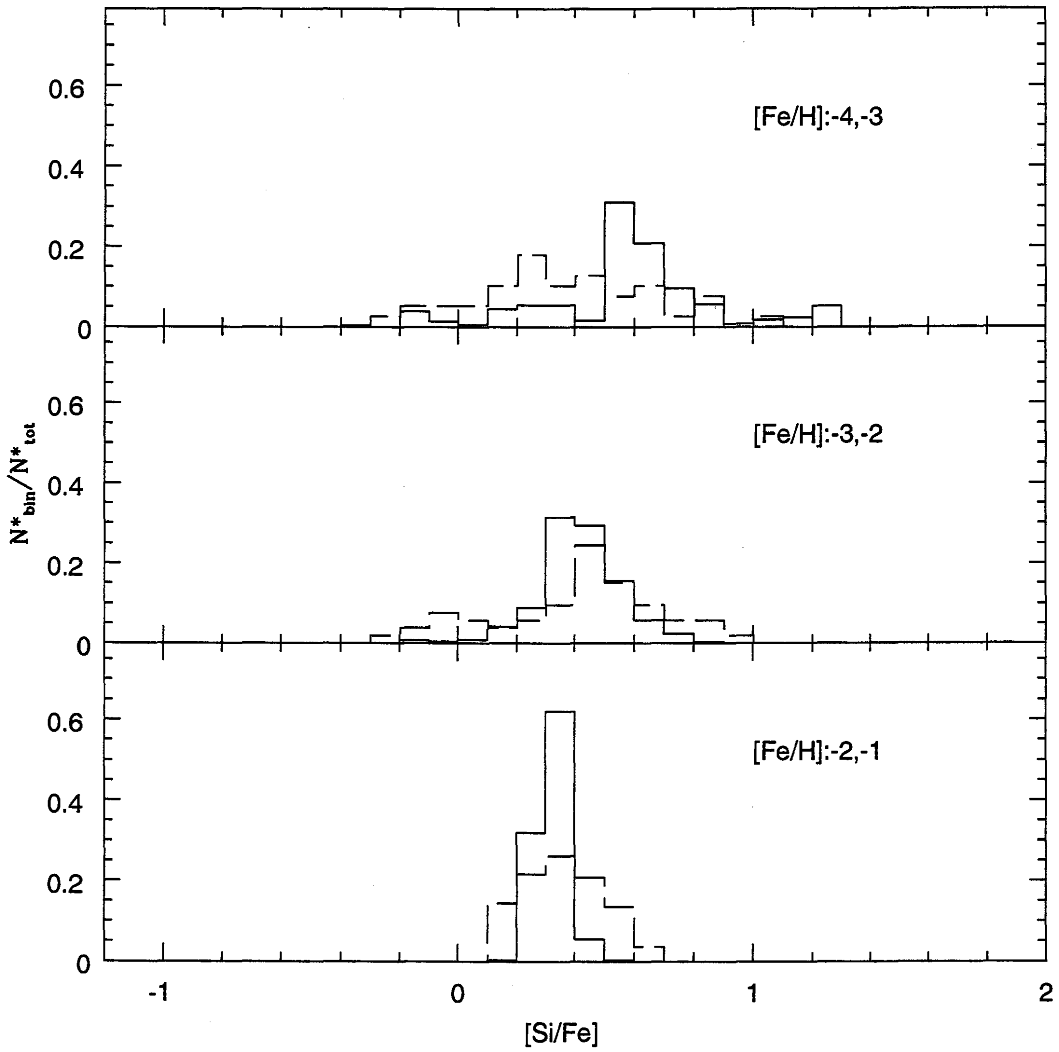

Figure 4.11. The relative frequency of stars at a given [Si/Fe] ratio for different enrichment phase. In black line the predictions of the model, in red line the observational data

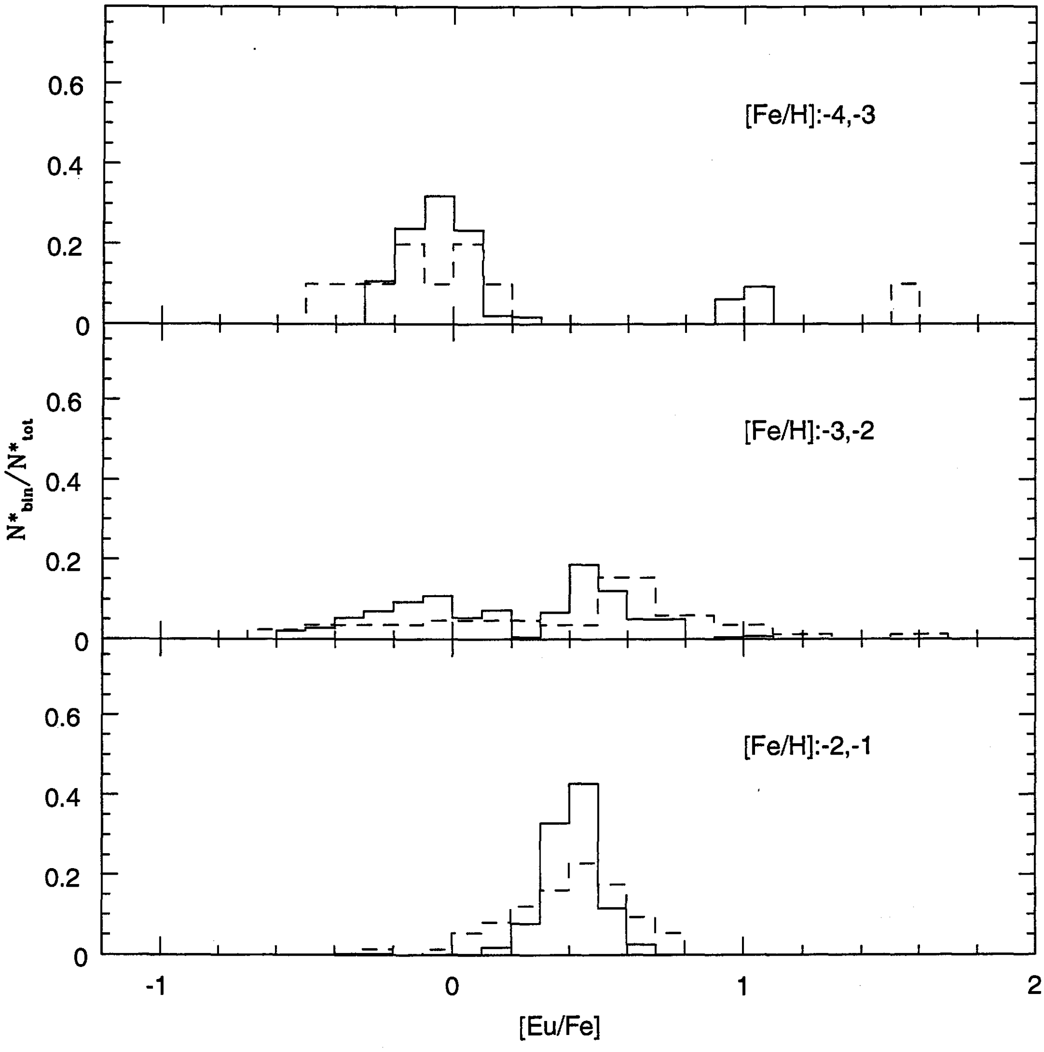

Figure 4.12. The relative frequency of stars at a given [Eu/Fe] ratio for different enrichment phase. In black line the predictions of the model, in red line the observational data

by the observational errors. In the low metallicity range some discrepancies can be noticed. For instance, the predicted [Si/Fe] distribution is slightly shifted toward higher metallicity ratios compared to observations. Therefore a more careful analysis of nucleosynthesis yields is required (for instance using metallicity dependent Si yields). For what concerns Eu, the results at low [Fe/H] cannot predict the r-process rich stars, being the highest ratio of [Eu/Fe] predicted by the model $\sim 0.4 dex$ lower than the observed one in these stars

The model does not reproduce well the total number of stars present in the range $-4 < [Fe/H] < -3$: the number of simulated stars is too low. This is due to a too fast rise of [Fe/H]. Moreover, the model predicts that ~ 5% of the simulated stars are metal free. This is the fraction of stars formed in the first 5 Myr, in which no SN has yet exploded and enriched the ISM. We underline that the star formation can be slowed down by a different infall rate which would modulate a different star formation and this can solve these two problems. The problem of the metal free stars can be also solved by adopting a different IMF. The results of many works (see Larson 1998, Abel, Bryan & Norman 2000, Hernandez & Ferrara 2001, Nakamura & Umemura 2001, Mackey, Bromm, & Hernquist 2003) predict that the star formed in a metal free gas must be massive stars. So the long living stars which are low mass stars, start to born when the ISM has been already enriched by these massive and metal free stars, the so-called Population III. The effect of the Pop III on the global chemical evolution should be negligible (see Matteucci & Pipino 2005, Matteucci & Calura 2005, Ballero et al. 2006), being the total amount of recycled mass small.

Nevertheless, we have decided, preliminary, to use the same parameters and conditions of the homogeneous model, to test the validity of the inhomogeneous one. It is clear from the figures that this new model for a high number of star formation events well approximate the homogeneous model, which is shown in the figures by the black solid line.

4.4.2 The ratios [Ba/Eu] and [Ba/Y]

Our model predicts a spread in the abundances ratios if the ratios of the yields of the same elements are different as a function of the stellar mass. This is not the case for what concern the yields of neutron capture elements considered in our nucleosynthesis prescriptions. In figure 4.13 we show the ratio [Ba/Eu] versus [Fe/H] . As expected the results of the model show a small spread, as for the plot for [α/Fe], being the production ratio between Ba and Eu almost constant as a function of the stellar mass. On the other hand, the observational data

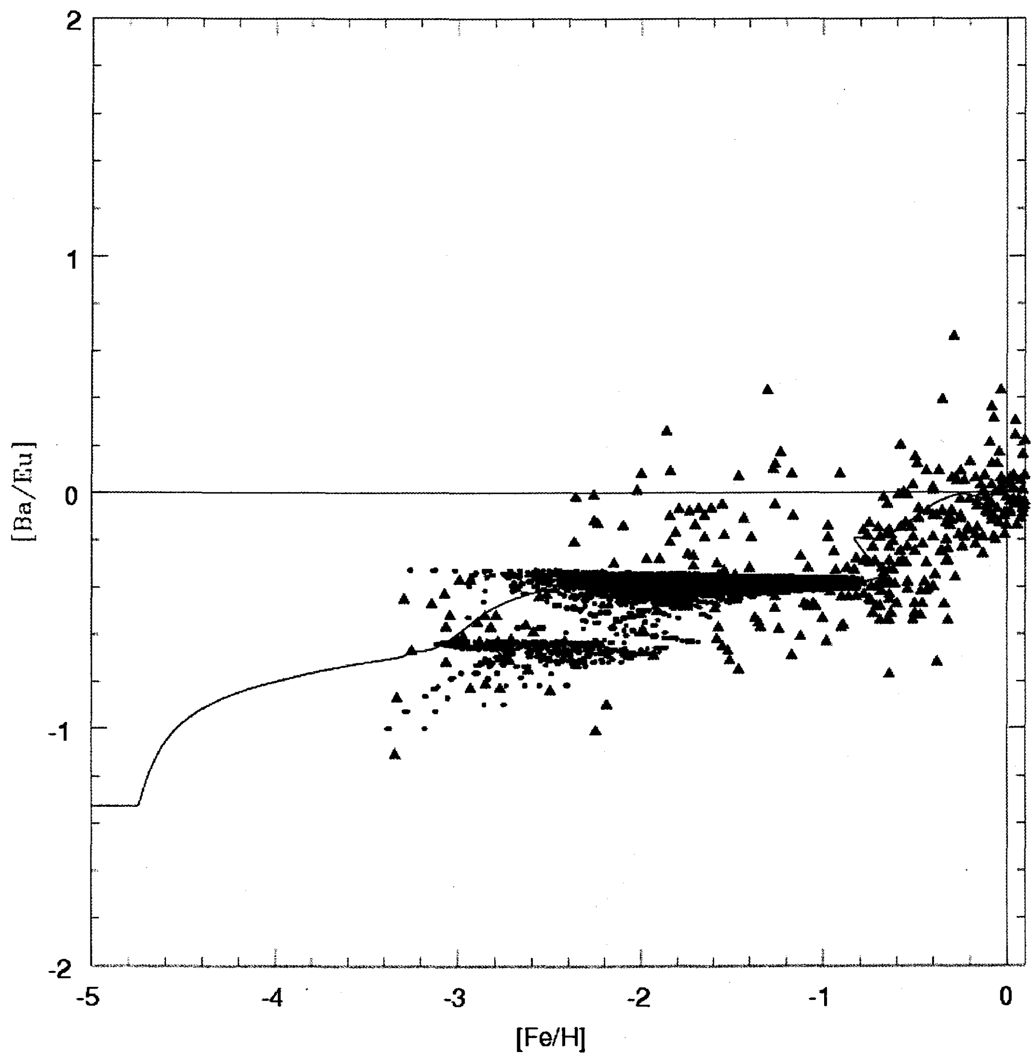

Figure 4.13. [Ba/Eu] vs [Fe/H]. The abundances of simulated stars in blue dots, observational data in red triangles. The black line is the prediction of the homogeneous model

show a spread. We observe that most of the data seem to have a higher Ba abundance than that predicted by our model. Taking into account this fact, the observational spread could be explained either by an earlier production of Ba by s-process in intermediate stars from 3 to $8M_{\odot}$ (that we do not take in account in our nucleosynthesis), or by a self enrichment of the observed stars due to dredge-up or to a binary system with an AGB mass transfer to the presently observed companion star (see Aoki et al. 2006).

In the figure 4.14, we show the ratio [Ba/Y] versus [Fe/H]. The results of the model relative to this ratio is not satisfactory. The observational data show a very large scatter at [Fe/H] $\sim$ -3 that is not be predicted by our model. Contrarily to the [Ba/Eu] ratio, for which the available data show a moderate spread at [Fe/H] $\sim$ -3, [Ba/Y] ratio shows a large spread. A possible way to explain this spread could be that the r-process yields that we use in our model, are indicative of the mean contribution by r-process to the abundances of these elements. We recall from the introduction of this work, that these two elements are in different peaks both for what concern s-process (not so important at this stage), and for what concern r-process. It could be that, as introduced by Otsuki et al. (2003), the r-process is not unique but consists of different contributions and what we use are only the mean values. Massive stars may produce r-process with different patterns, probably as functions of the multiple factors which influence r-process. In our inhomogeneous model we use only one pattern for all the neutron capture elements. This could be the reason why we are not able to well reproduce the spread for the ratios of neutron capture elements. Moreover, this problem should be more visible when we compare neutron capture elements belonging to different peaks as in the case of [Ba/Y].

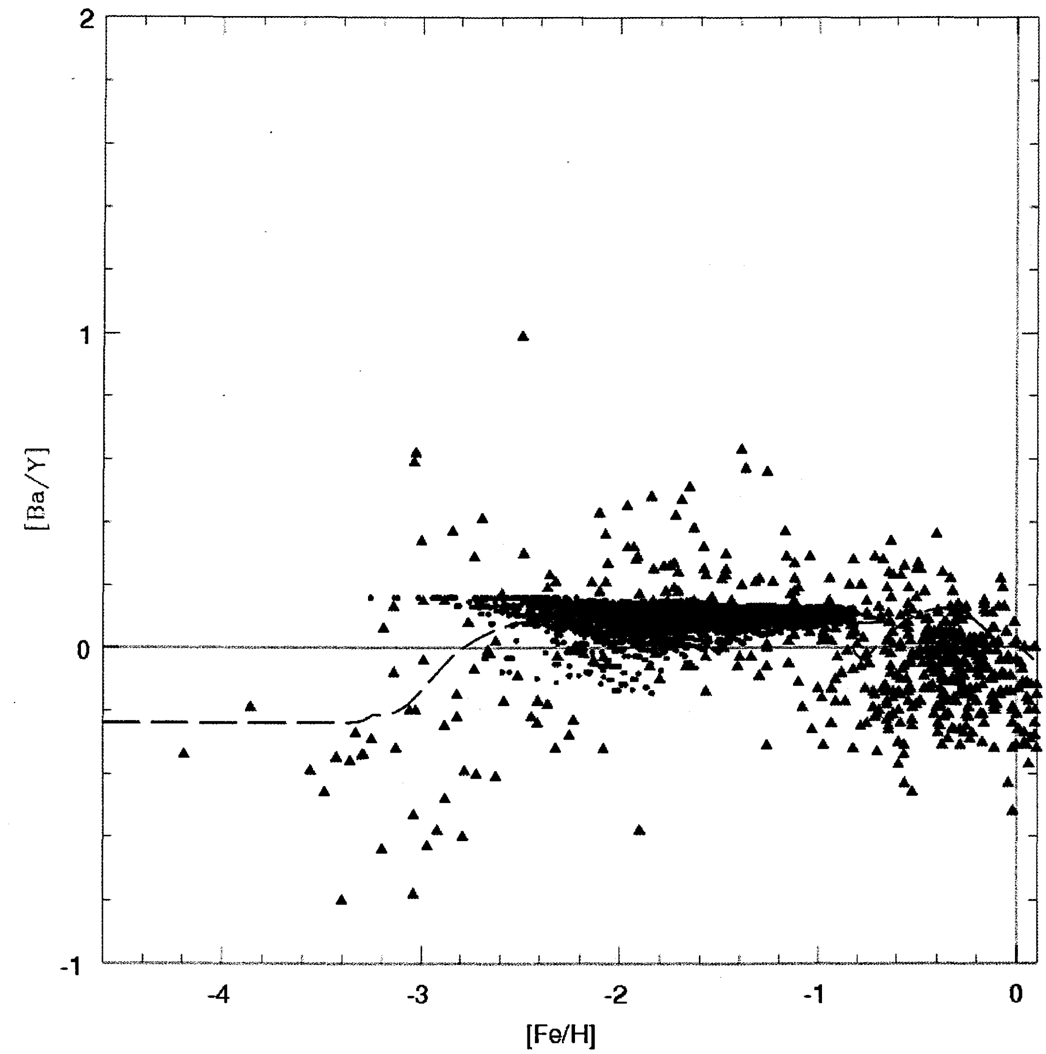

Figure 4.14. [Ba/Y] vs [Fe/H]. The abundances of simulated stars in blue dots, observational data in red triangles. The black line is the prediction of the homogeneous model

Chapter 5

Chemical evolution of barium and europium in Local dwarf spheroidal galaxies

“”From a drop of water,” said the writer, ”a logician could infer the possibility of an Atlantic or a Niagara without having seen or heard of one or the other. So all life is a great chain, the nature of which is known whenever we are shown a single link of it.” by Sir Arthur Conan Doyle

In this chapter we present the results obtained in collaboration with Gustavo Lanfranchi (Department of Astronomy, University of São Paulo). The success of LM03 and LM04 models (see chapter 1) in reproducing several observational constraints allows us to use them as tools to test the theories about the sites of production and the processes responsible for the synthesis of Ba and Eu in dSph galaxies. By adopting the nucleosynthesis prescriptions for these elements which are able to reproduce the most recent observed data for our Galaxy, as shown in chapter 2, and comparing the predictions of the models with observational data, it is possible to verify if the assumptions made regarding the nucleosynthesis of Ba and Eu can also fit the data of local dSph galaxies.

5.1 Observational Data

Recently, red giant stars of dSph galaxies have been the subject of several works with the aim of determining with high-resolution spectroscopy the abundance of several chemical elements including heavy elements such as barium and europium (Bonifacio et al. 2000; Shetrone, Coté & Sargent 2001; Shetrone et al. 2003; Venn et al. 2004; Sadakane et al. 2004; Fulbright, Rich & Castro, 2004; Geisler et al. 2005). From these observations we gathered the data from the galaxies that were analyzed in LM03 and LM04 and for which there are abundance determinations for both Ba and Eu. They are Carina, Draco, Sculptor, Ursa Minor and Sagittarius. Despite of the relative small number of data points, it is possible to compare the observed abundance ratios with the model predictions. We choose to compare the observed ratios [Ba/Fe], [Eu/Fe] and [Ba/Eu] with the ones predicted by the models, since these ratios can provide some clues not only to the nucleosynthesis of Ba and Eu, but also to all s-process and r-process elements.

In order to properly compare different data from different authors with the predictions of the models we adopted the abundance values of Shetrone, Coté & Sargent (2001), Shetrone et al. (2003), and Sadakane et al. (2004) updated by Venn et al. (2004). Venn et al. (2004) homogenized the atomic data for spectral lines of Ba and Eu providing data with improved quality which allow a consistent comparison between data from different sources. Otherwise, the effect of combining these different data would be seen as a larger spread in the abundances and possibly in the abundance ratios of 0.1 to 0.2 dex (see Venn et al. 2004). In the case of Bonifacio et al. (2000) data, Eu is obtained using hyper-fine splitting (HFS) (see their Table 5), but Ba is not. The authors claimed that the Ba abundances obtained with HFS would exhibit no significant difference since the line observed (Ba II 6496.9) is a strong line which is not affected by this correction (Bonifacio private communication, see also Shetrone et al. 2003).

Some of the observed stars, however, exhibit anomalous values of [Ba/H] or [Eu/H], and for this reason were excluded from the sample. Two stars in Ursa Minor, K and 199 (in Shetrone, Coté & Sargent 2001), exhibit heavy-element abundance ratios enhanced relative to those typical for other dSph stars: the Ursa Minor K star has an abundance pattern dominated by the s-process and was classified as a Carbon star while Ursa Minor 199 is dominated by r-process (see also Sadakane et al. 2004). In Sculptor, there are also two stars with enhanced heavy-element abundance: Sc982 (Geisler et al. 2005) and Sculptor H-400

Table 5.1. Models for dSph galaxies. $M_{tot}^{initial}$ is the baryonic initial mass of the galaxy, ν is the star-formation efficiency, w_i is the wind efficiency, and n, t and d are the number, time of occurrence and duration of the SF episodes, respectively.

galaxy	$M_{tot}^{initial}(M_\odot)$	$\nu(Gyr^{-1})$	w_i	n	t(Gyr)	d(Gyr)	IMF
Sculptor	$5 * 10^8$	0.05-0.5	11-15	1	0	7	Salpeter
Draco	$5 * 10^8$	0.005-0.1	6-10	1	6	4	Salpeter
Ursa Minor	$5 * 10^8$	0.05-0.5	8-12	1	0	3	Salpeter
Carina	$5 * 10^8$	0.02-0.4	7-11	2	6/10	3/3	Salpeter
Sagittarius	$5 * 10^8$	1.0-5.0	9-13	1	0	13	Salpeter

(Shetrone et al. 2003). While Shetrone et al. (2003) claimed that the r-process dominated abundance could be attributed to inhomogeneous mixing of the SNe II yields, Geisler et al. (2005) classified Sc982 as a heavy element star which could have been enriched by an other star, which is now dead. Either way, all these stars do not exhibit an abundance pattern characterized only by the nucleosynthesis process occurring inside the star, but also one which was contaminated by external factors. The maintenance of these stars in the sample could lead to an erroneous comparison with the model predictions and, as a consequence, to a misleading interpretation and to wrong conclusions regarding the processes and the site of production of the heavy elements analyzed. Therefore, we excluded these stars from our sample, whereas all the other stars were considered and included in the comparisons with the models predictions.

5.2 Chemical evolution models for the Local dSph galaxies

We use in this work the same chemical evolution model for dSph galaxies galaxies as described in LM03 and LM04. The model is able to reproduce the [α/Fe] ratios, the present gas mass and the inferred total mass of five dSph galaxies of the Local Group, namely Carina, Draco, Sculptor, Sagittarius and Ursa Minor, and also the stellar metallicity distribution of Carina (Koch et al. 2004). The scenario representing these galaxies is characterized by one long episode (two episodes in the case of Carina) of star formation (SF) with very low efficiencies (except in the case of Sagittarius) - $\nu = 0.001$ to 0.5 Gyr $^{-1}$ - and by the occurrence of very intense galactic winds - w_i = 6-13. The model allows one to follow in detail the evolution of the abundances of several chemical elements, starting from the matter reprocessed by the stars and restored into the ISM by stellar winds and type II and Ia supernova explosions.

The main features of the model are:

- one zone with instantaneous and complete mixing of gas inside this zone;
- no instantaneous recycling approximation, i.e. the stellar lifetimes are taken into account;
- the evolution of several chemical elements (H, D, He, C, N, O, Mg, Si, S, Ca, Fe, Ba and Eu) is followed in detail;

In the scenario adopted in the previous works, the dSph galaxies form through a continuous and fast infall of pristine gas until a mass of $\sim 10^8 M_\odot$ is accumulated. One crucial feature in the evolution of these galaxies is the occurrence of galactic winds, which develop when the thermal energy of the gas equates its binding energy (Matteucci & Tornambé 1987). This quantity is strongly influenced by assumptions concerning the presence and distribution of dark matter (Matteucci 1992). A diffuse (R_e/R_d=0.1, where R_e is the effective radius of the galaxy and R_d is the radius of the dark matter core) but massive ($M_{dark}/M_{Lum} = 10$) dark halo has been assumed for each galaxy.

In table 5.1 we summarize the adopted parameters for the models of dSph galaxies.

5.3 Results

5.3.1 Europium

The [Eu/Fe] ratio as a function of [Fe/H] observed in the four Local Group dSph galaxies is compared with the model predictions in the Figures 5.1 to 5.4 (Carina, Draco, Sculptor and Ursa Minor, respectively). The predicted behaviour seen in the plots is the same for all galaxies: [Eu/Fe] is almost constant with supra-solar values ($\sim$ 0.5 dex) until [Fe/H] ~ -1.7 dex (depending on the galaxy). Above this metallicity, the [Eu/Fe] values start decreasing fast in Sculptor and Carina (there are no points at these metallicities for Draco and Ursa Minor) similar to what is observed in the case of the [α/Fe] ratio. This behaviour is consistent with the production of Eu by r-process taking place in massive stars with $M > 10 M_\odot$. Stars

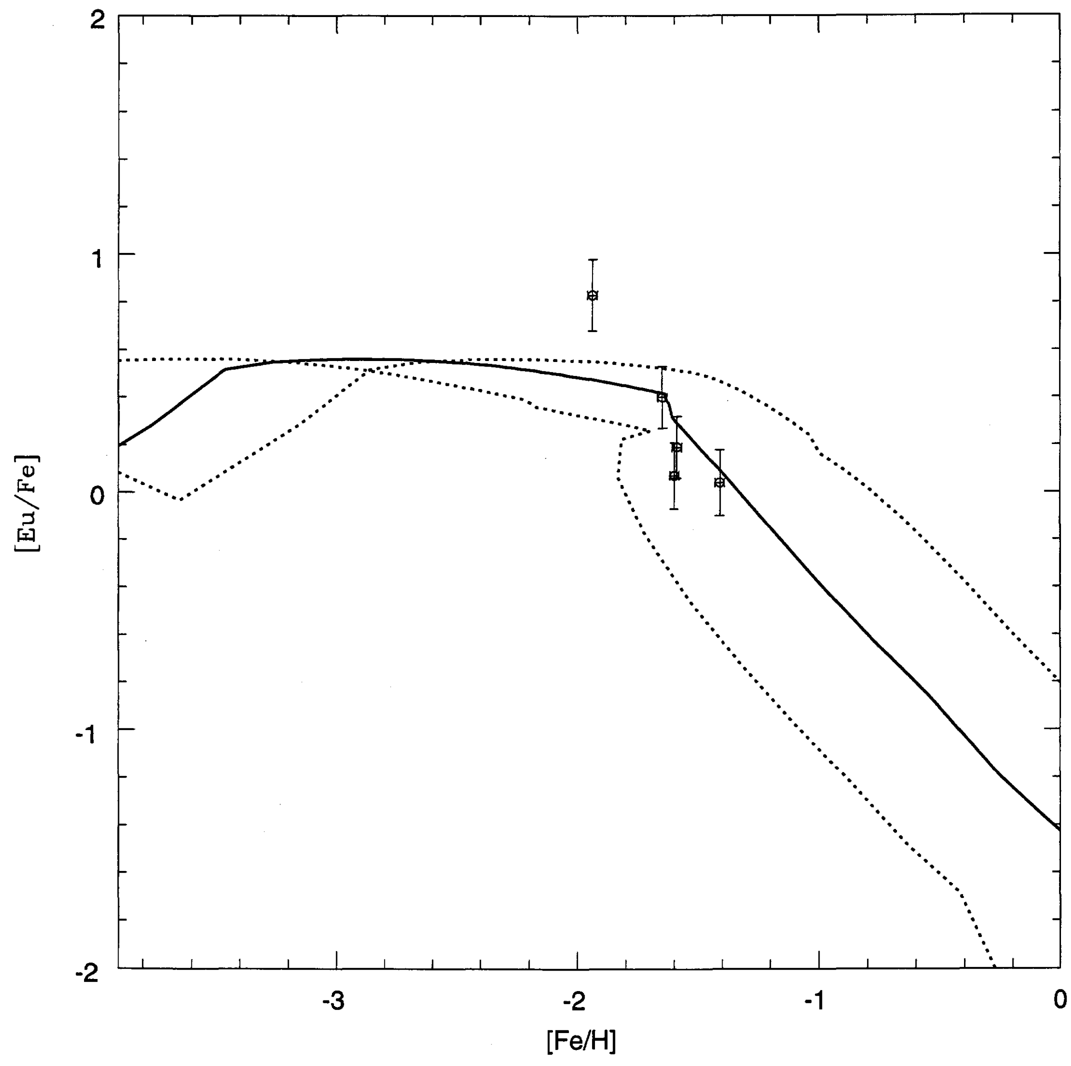

Figure 5.1. [Eu/Fe] vs. [Fe/H] observed in Carina dSph galaxy compared to the predictions of the chemical evolution model for Carina. The solid line represents the best model (ν = 0.1 Gyr^{-1}, w_i = 7) and the dotted lines the lower (ν = 0.02 Gyr^{-1}) and upper (ν = 0.4 Gyr^{-1}) limits for the SF efficiency.

in this mass range have short lifetimes and enrich the ISM at early stages of galactic evolution giving rise to high values of [Eu/Fe], since the production of Fe in these stars is lower than in type Ia SNe occurring later. When the SNe Ia begin to occur, the Fe abundance increases and, consequently, the [Eu/Fe] ratio decreases, as one can see also in the data.

The predicted [Eu/Fe] ratios in all four dSph galaxies well reproduce the observed trend: an almost constant value at low metallicities, and an abrupt decrease starting at [Fe/H] > -1.7 dex. In the model this decrease is caused not only by the nucleosynthesis prescriptions and stellar lifetimes, but also by the effect of a very intense galactic wind on the star formation rate and, consequently, on the production of the elements involved. In fact, since the wind is very efficient, a large fraction of the gas reservoir is swept from the galaxy. At this point, the SF is almost halted and the production of Eu goes down to negligible values. The injection of Fe in the ISM, on the other hand, continues due to the large lifetimes of the stars responsible for its production. The main result is an abrupt decrease in the [Eu/Fe] ratios, larger than the one that one would expect only from the nucleosynthesis point of view if there was no such intense wind. The abrupt decrease follows the trend of the data very well, especially in the case of Sculptor and Carina. For these two galaxies there are stars observed with metallicities higher than the one corresponding to the time when the wind develops ([Fe/H] > -1.7 dex), and which are characterized by lower values of [Eu/Fe], in agreement with our predictions. The observed stars of the other two dSph galaxies, Draco and Ursa Minor, exhibit [Fe/H] values which place them before the occurrence of SNe Ia, so it is not possible to verify if the abrupt decrease in the [Eu/Fe] occurs also in these objects. Only observations of more stars will confirm the trend. It should be said again that the same phenomena explain very well the [α/Fe] ratios and the final total mass and present day gas mass observed in these galaxies (LM03, LM04).

The small differences in the SF and wind efficiencies do not affect strongly the predictions of the models. As one can see in Table 1, the range of values for the SF efficiency is practically the same for Carina, Sculptor and Ursa Minor (ν = 0.02-0.4, 0.05-0.5, 0.05-0.5 Gyr^{-1}, respectively), whereas Draco observational constraints are reproduced by a model with lower values of ν, ν = 0.005-0.1 Gyr^{-1}. These values reflect in very similar curves for the first three galaxies and a curve for Draco with only a small difference, namely a [Eu/Fe] ratio which starts decreasing very slowly at metallicities lower ([Fe/H] $\sim$ -2.0 dex) than in the other three galaxies. However, the abrupt decrease starts at a similar point. The same similarity can be

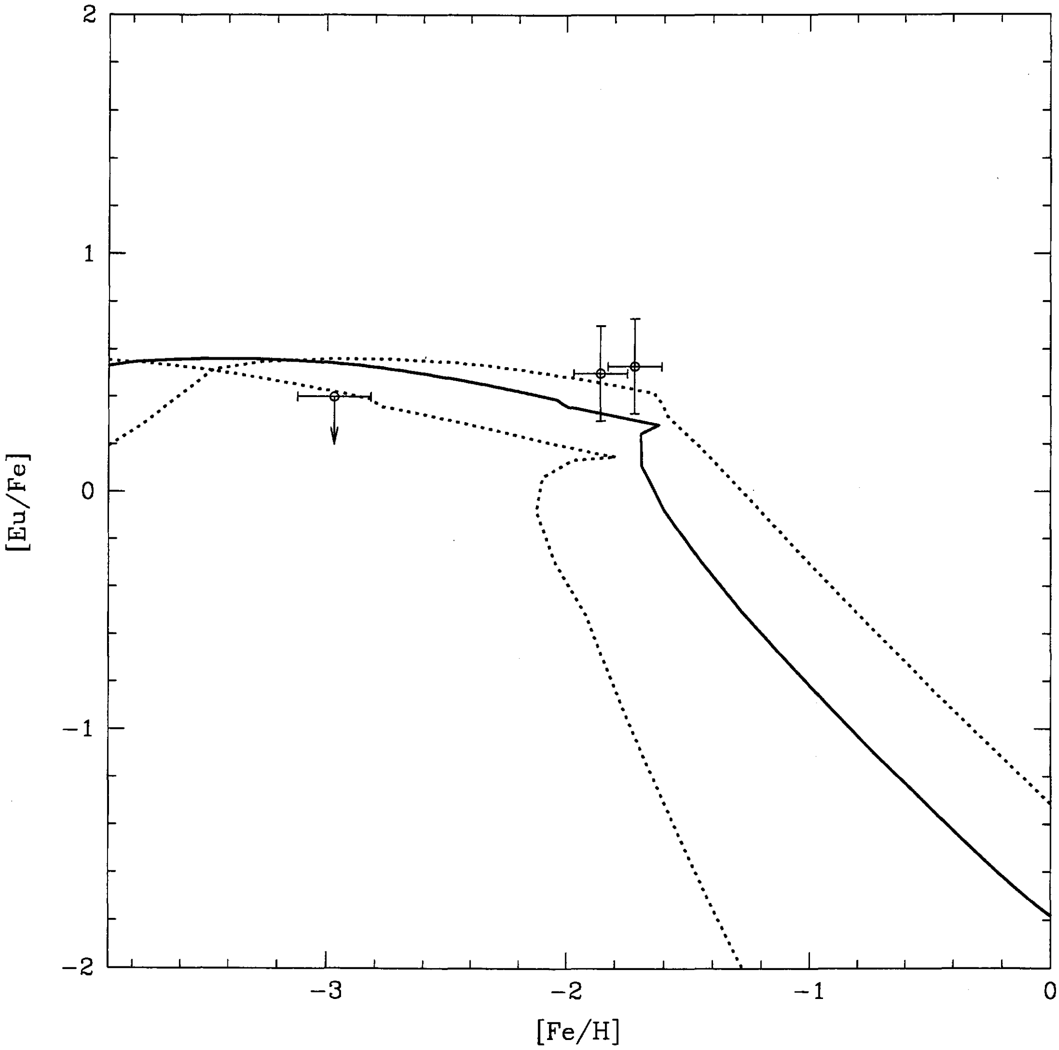

Figure 5.2. [Eu/Fe] vs. [Fe/H] observed in Draco dSph galaxy compared to the predictions of the chemical evolution model for Draco. The solid line represents the best model ($\nu = 0.03$ Gyr^{-1}, $w_i = 6$) and the dotted lines the lower ($\nu = 0.005$ Gyr^{-1}) and upper ($\nu = 0.1$ Gyr^{-1}) limits for the SF efficiency.

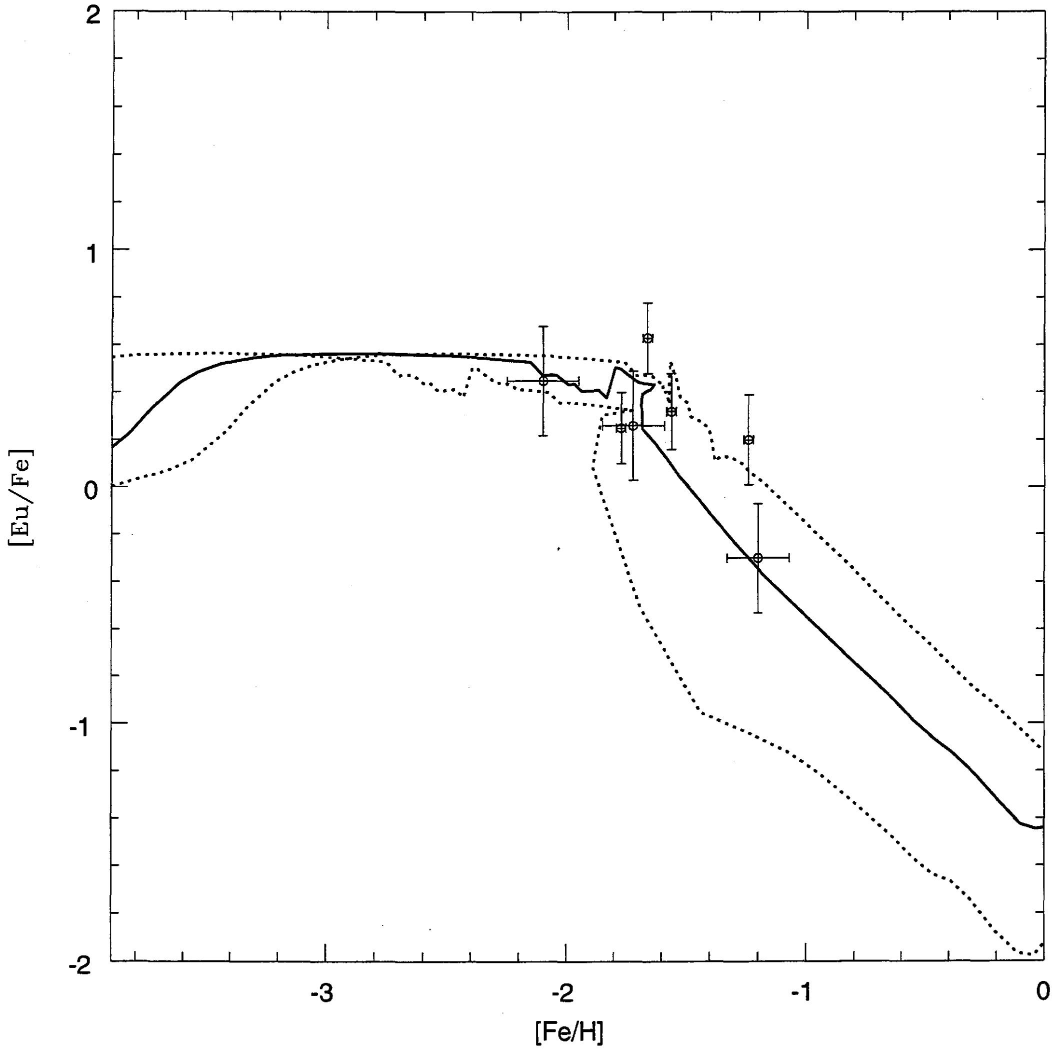

Figure 5.3. [Eu/Fe] vs. [Fe/H] observed in Sculptor dSph galaxy compared to the predictions of the chemical evolution model for Sculptor. The solid line represents the best model ($\nu = 0.2\ Gyr^{-1}$, $w_i = 13$) and the dotted lines the lower ($\nu = 0.05\ Gyr^{-1}$) and upper ($\nu = 0.5\ Gyr^{-1}$) limits for the SF efficiency.

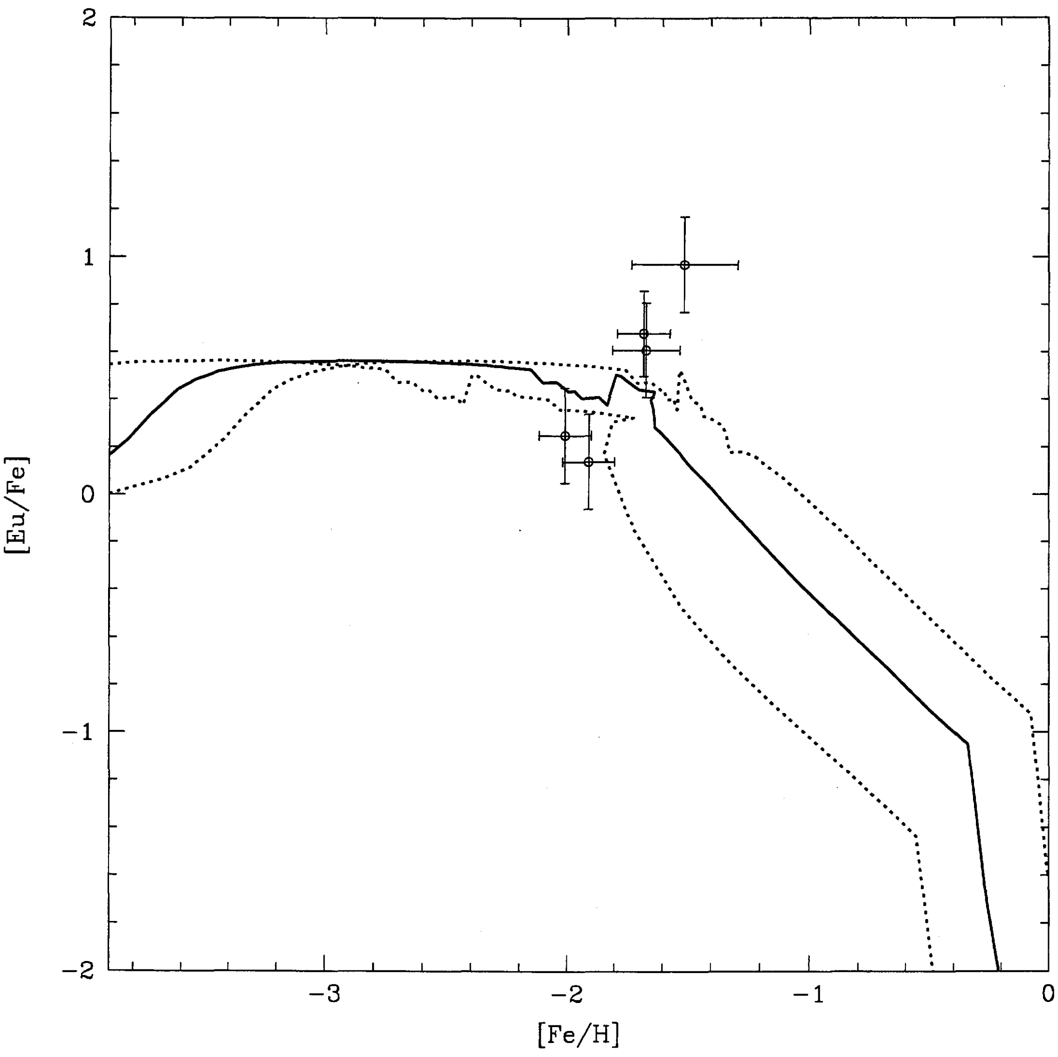

Figure 5.4. [Eu/Fe] vs. [Fe/H] observed in Ursa Minor dSph galaxy compared to the predictions of the chemical evolution model for Ursa Minor. The solid line represents the best model ($\nu = 0.2\ Gyr^{-1}$, $w_i = 10$) and the dotted lines the lower ($\nu = 0.05\ Gyr^{-1}$) and upper ($\nu = 0.5\ Gyr^{-1}$) limits for the SF efficiency.

seen in the values of the wind efficiency: Carina - w_i = 7-11, Draco - w_i = 6-10, Sculptor - w_i = 11-15 - and Ursa Minor - w_i = 8-12. Only Sculptor is characterized by a wind efficiency a little bit higher, but this fact does not influence the pattern of the abundances significantly. They all exhibit an intense decrease in the [Eu/Fe] ratio after the wind develops. The small differences in the ranges of values for w_i are related more directly to the gas mass and total mass observed.

What should be highlighted is that the nucleosynthesis prescriptions adopted here allow the models to reproduce very well the data, supporting the assumption that Eu, also in dSph galaxies, is a pure r-process element synthesized in massive stars in the range $M = 10-30M_{\odot}$, as it is in the Milky Way (see chapter 2 and Cescutti et al. 2006). Besides that, the low SF efficiencies and the high wind efficiencies are required also to explain the [Eu/Fe] observed pattern, especially the abrupt decrease of the data in some dSph galaxies.

5.3.2 Barium

The evolution of [Ba/Fe] as a function of [Fe/H] predicted by the models and compared to the observed data in four Local Group dSph galaxies is shown in the Figures 5.5 to 5.8 (Carina, Draco, Sculptor and Ursa Minor, respectively). One can easily notice that the predicted curves exhibit a similar behaviour in all four galaxies: the predicted [Ba/Fe] ratio increases fast at very low metallicities ([Fe/H] < -3.5 dex), then remains almost constant, close to the solar value, at low-intermediate metallicities (-3.5< [Fe/H] < -1.7 dex) and then starts decreasing soon after the occurrence of the galactic wind at relatively high metallicities ([Fe/H] > -1.7 dex). In this case, the decrease is not so intense as it is in the case of [Eu/Fe], due to the differences in the nucleosynthesis of Ba and Eu.

The predicted shape of the [Ba/Fe] vs. [Fe/H] relation in dSph galaxies can be associated to the two different Ba contributions, from stars in different mass ranges (high masses - 10 to 30 $M_{\odot}$ - and low masses - 1 to 3 $M_{\odot}$). In the low metallicity portion of the plot the production of Ba is dominated by the r-process taking place in massive stars which have lifetimes in the range from 6 to 25 Myr. Therefore, the [Ba/Fe] ratio increases fast reaching values above solar already at [Fe/H] ~ -3.5 dex and stays almost constant up to [Fe/H]=-1.7 dex. It is worth noting that the massive star contribution is more clearly seen when the SF efficiency is low. In this regime, in fact, the stars are formed slowly and the difference between the contribution of stars of different masses is more evident, since the increase of the

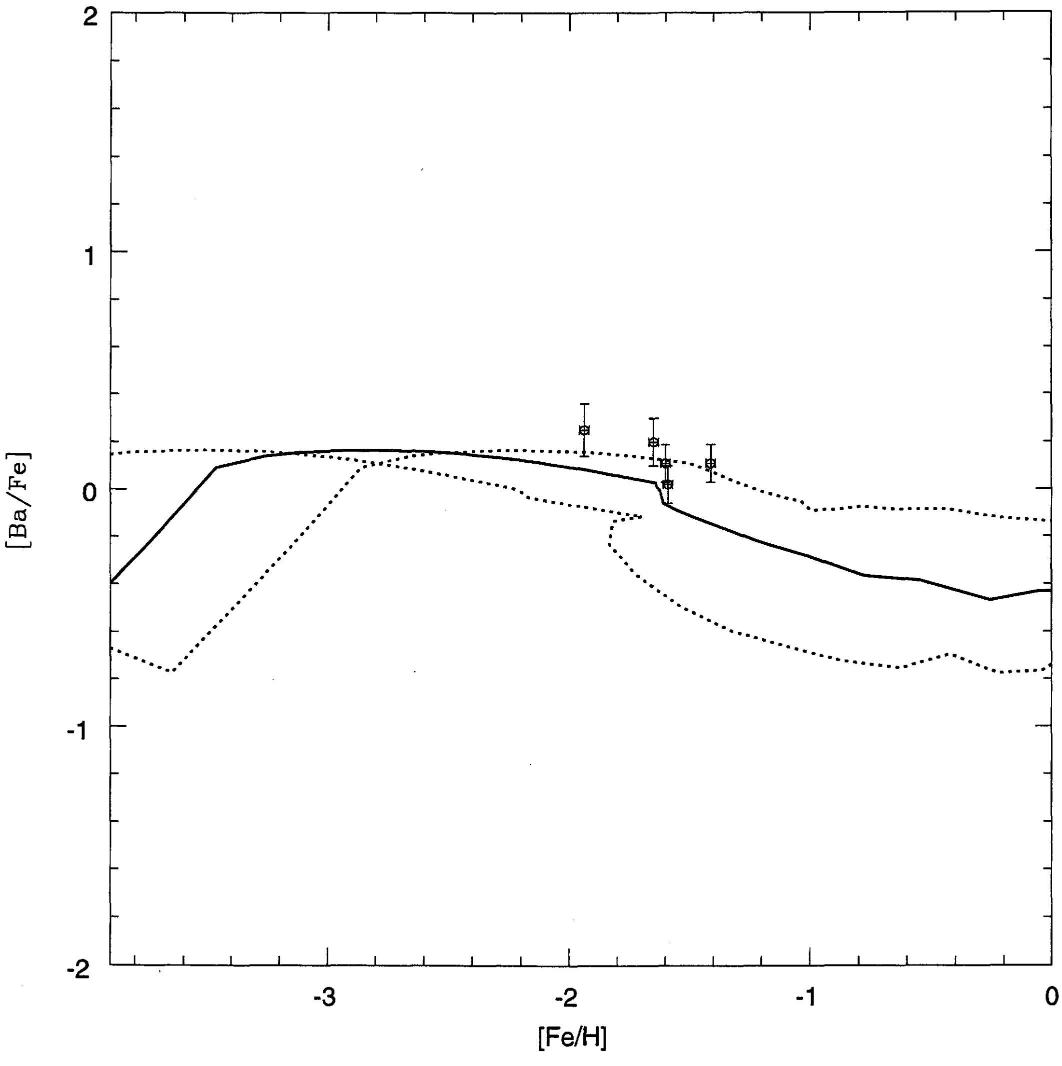

Figure 5.5. [Ba/Fe] vs. [Fe/H] observed in Carina dSph galaxy compared to the predictions of the chemical evolution model for Carina. The solid line represents the best model ($\nu = 0.1\ Gyr^{-1}$, $w_i = 7$) and the dotted lines the lower ($\nu = 0.02\ Gyr^{-1}$) and upper ($\nu = 0.4\ Gyr^{-1}$) limits for the SF efficiency.

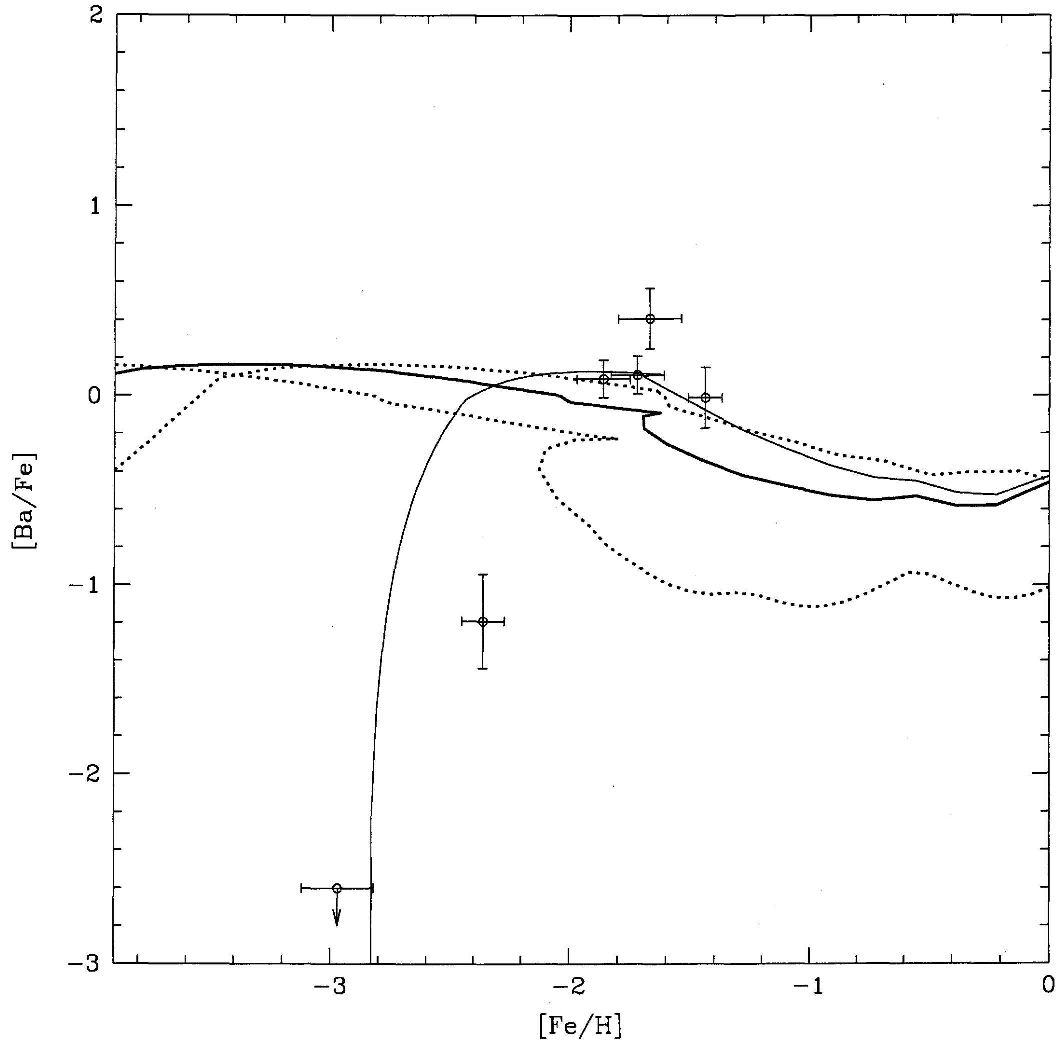

Figure 5.6. [Ba/Fe] vs. [Fe/H] observed in Draco dSph galaxy compared to the predictions of the chemical evolution model for Draco. The solid line represents the best model (ν = 0.03 Gyr^{-1}, w_i = 6) and the dotted lines the lower (ν = 0.005 Gyr^{-1}) and upper (ν = 0.1 Gyr^{-1}) limits for the SF efficiency. The thin line represents the best model without Ba production in massive stars.

metallicity and the evolution of the galaxy proceed at a low speed. On the other hand, when the SF efficiency is higher (like in the Milky Way), the early contribution of massive stars is more difficult to distinguish, because of the much faster increase in metallicity.

At low-intermediate metallicities ($-3.5 <$ [Fe/H] < -1.7 dex), the production of Ba is still the one by r-process taking place in massive stars, in particular in those with masses around the lower limit for the r-process Ba producers ($\sim 10 M_{\odot}$).

The contribution to s-process Ba enrichment from low mass stars (LMS), with lifetimes from 400Myr to 10 Gyr, affects significantly the predicted [Ba/Fe] ratio only after the onset of the wind, consequently only after the occurrence of the first SNe Ia. At this stage, the [Ba/Fe] starts to decrease rapidly, since the first SNe Ia are injecting large amounts of Fe into the ISM. Together with the enrichment of Fe, the SNe Ia release also large quantities of energy in the ISM which gives rise to a galactic wind. As the galactic wind starts, the SFR goes down to very low values and the production of Ba is limited only to the LMS, especially those at the low mass end. The injection of Ba in the ISM at this stage is, however, not so effective due to the galactic wind which removes a large fraction of the material freshly released in the hot medium (Ferrara & Tolstoy 1999, Recchi et al. 2001, 2004). The effect of the Ba production in LMS is particularly important to slow down the abrupt decrease in [Ba/Fe] after the occurrence of the galactic wind. If this production is not taken in account, the [Ba/Fe] values after the onset of the wind would go down faster to very low values.

One can see in the Figures 5.5 to 5.8 that the observational trends at high metallicities are very well reproduced by the model predictions supporting the assumptions made regarding the nucleosynthesis of Ba. As already mentioned the contribution from LMS to the enrichment of Ba becomes important starting from intermediate to high metallicities ([Fe/H] > -1.9 dex), depending on the SF efficiency adopted. In this metallicity range, the data of all four galaxies are very well reproduced, including the stars with low values of [Ba/Fe] which should have formed soon after the onset of the galactic wind.

On the other hand, at low metallicities ([Fe/H] < -2.4 dex) only the observational trend of Carina and Sculptor are well fitted by the model predictions. In Ursa Minor and Draco there are a few stars which exhibits a very low [Ba/Fe] (~ -1.2 dex) at low [Fe/H] (Figures 5.6 and 5.8). These points are well below the predicted curves and close to the values of the Milky Way stars at similar metallicities, which are reproduced by a chemical evolution model with the same nucleosynthesis prescriptions adopted here but with a higher SF efficiency. In

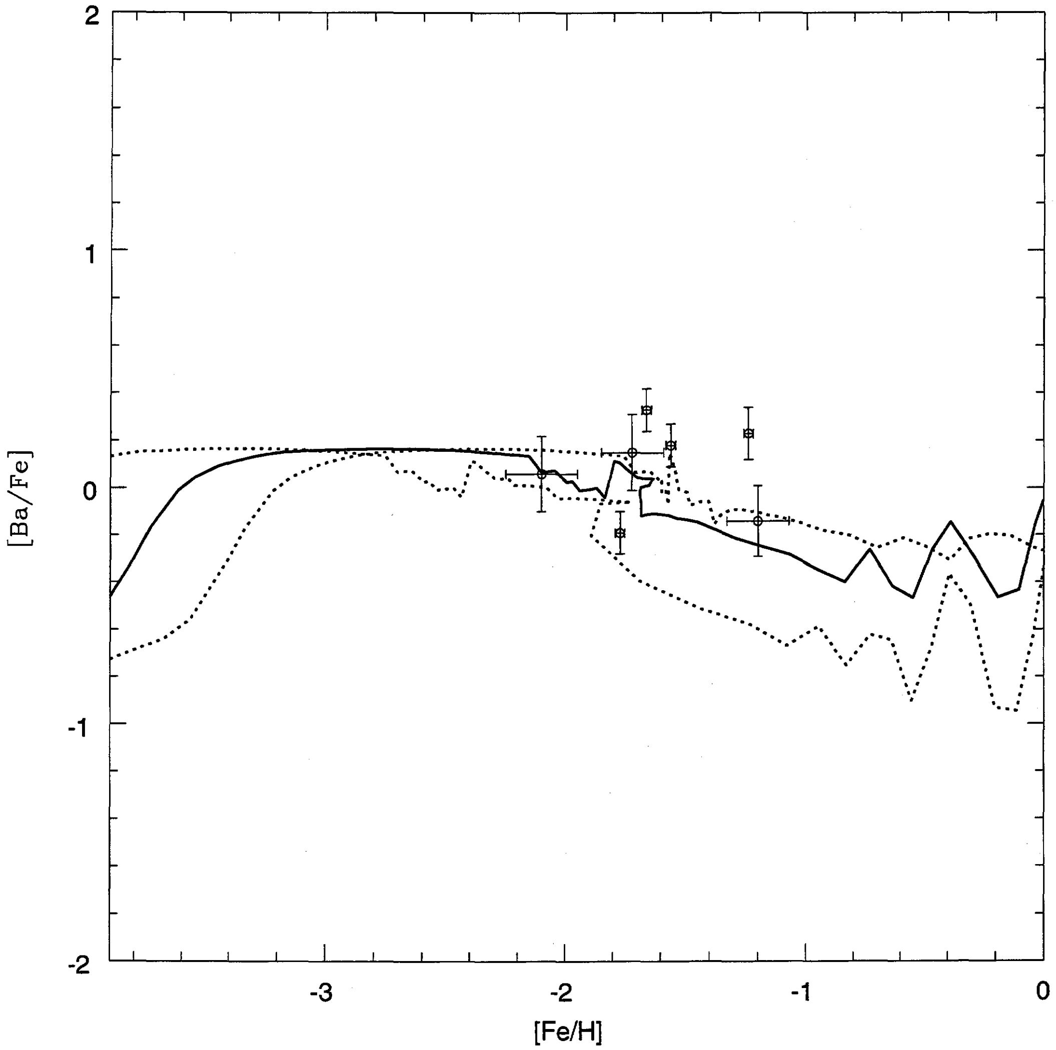

Figure 5.7. [Ba/Fe] vs. [Fe/H] observed in Sculptor dSph galaxy compared to the predictions of the chemical evolution model for Sculptor. The solid line represents the best model ($\nu = 0.2\ Gyr^{-1}$, $w_i = 13$) and the dotted lines the lower ($\nu = 0.05\ Gyr^{-1}$) and upper ($\nu = 0.5\ Gyr^{-1}$) limits for the SF efficiency.

general, it seems like if the data for the solar neighborhood show values of [Ba/Fe] lower than in the dSph galaxies at the same metallicity, although this fact should be confirmed by more data. For the α-elements is the opposite, dSph stars show lower [α/Fe] ratios than Galactic stars at the same metallicity (Shetrone & al. 2001; Tolstoy et al. 2003). LM03 and LM04 suggested that the difference in the behaviour of α-elements in the Milky Way and dSph galaxies should be ascribed to their different SF histories. In particular, the lower [α/Fe] ratios in dSph galaxies are due to their low star formation efficiency which produces a slow increase of the [Fe/H] with the consequence of having the Fe restored by type Ia SNe, and therefore a decrease of the [α/Fe] ratios, at lower [Fe/H] values than in the Milky Way. This effect has been described in Matteucci (2001) and is a consequence of the time-delay model applied to systems with different star formation histories.

Therefore, in the light of what is said above, can we explain also the differences between the predicted [Ba/Fe] in dSph galaxies and in the Milky Way? Again, the SF efficiency is the major responsible parameter for this difference. In the Milky Way model the SF efficiency is much larger (10 - 100 times) than the ones adopted for the dSph galaxies of the sample analyzed here. In the low efficiency regime, the contribution from LMS appears at lower metallicities than in the high SF regime, exactly for the same reason discussed for the [α/Fe] ratios. As a consequence, we predict a longer plateau for the [Ba/Fe] ratio in dSph galaxies than in the solar neighborhood and starting at lower metallicities. This prediction should in the future be confirmed or rejected by more data at low metallicities in dSph galaxies.

Since there are no observed stars at low [Fe/H] in Carina and Sculptor while there are three stars (one with an upper limit) with very low [Ba/Fe] in Draco and Ursa Minor, one could argue that the Ba production from massive stars is not necessary. To better see the effect of the r-process Ba production from massive stars, we computed models suppressing this contribution. In such a case, the predictions of the models lie below all the observed data and are not capable of fitting the stars with low [Ba/Fe]. Nevertheless, one can see from the thin lines in Figures 5.6 and 5.8 that the increase of the [Ba/Fe] ratio occurs at metallicities similar to those of the stars with low [Ba/Fe]. Besides that, this model also reproduces the high values of [Ba/Fe] at high metallicities and the [Ba/Eu] observed (see next section). In that sense, the observed low values of [Ba/Fe], if confirmed by more observations, could be explained by a model with Ba produced only by s-process contribution from LMS. Only more observations of stars with [Fe/H] $<$ -2.0 in dSph galaxies could solve this problem.

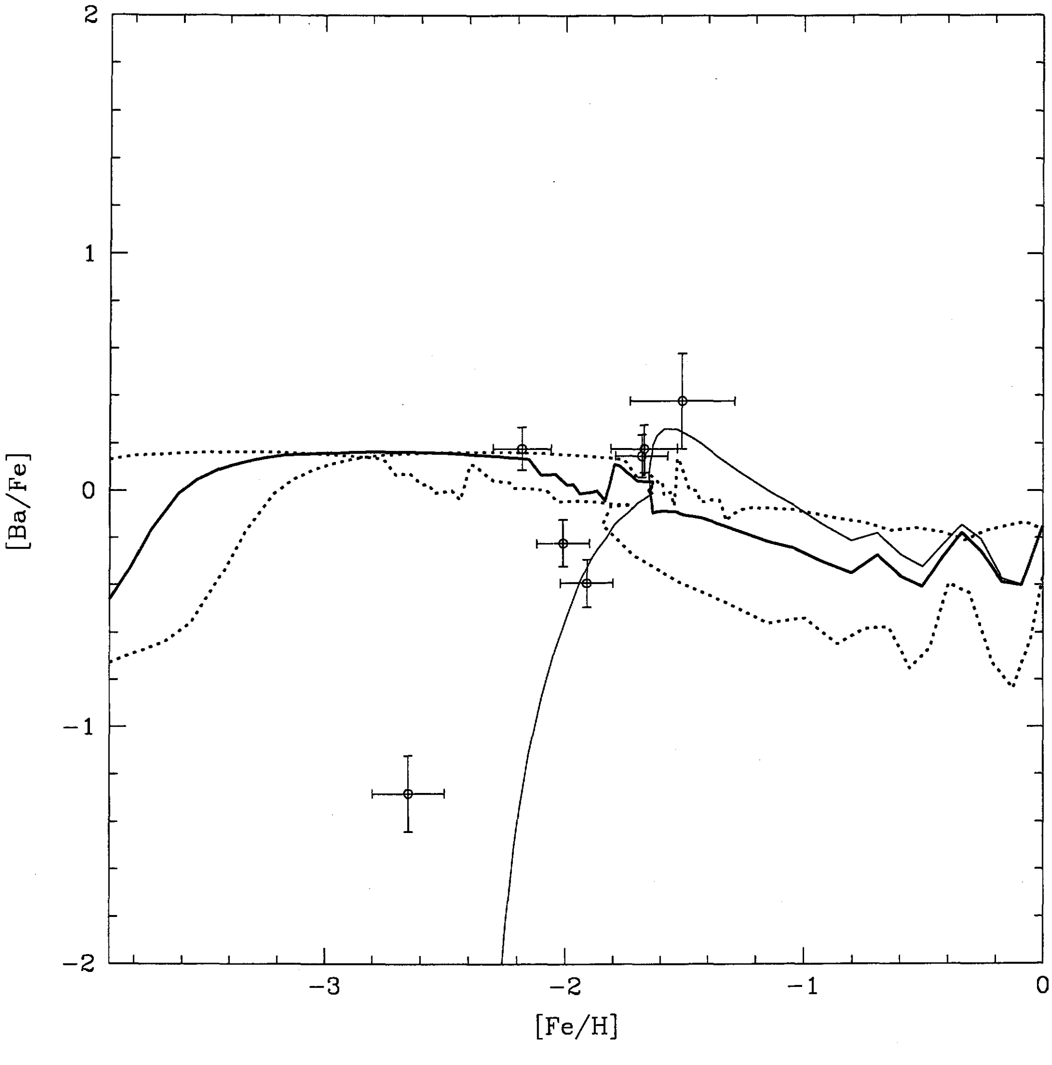

Figure 5.8. [Ba/Fe] vs. [Fe/H] observed in Ursa Minor dSph galaxy compared to the predictions of the chemical evolution model for Ursa Minor. The solid line represents the best model ($\nu = 0.2\ Gyr^{-1}$, $w_i = 10$) and the dotted lines the lower ($\nu = 0.05\ Gyr^{-1}$) and upper ($\nu = 0.5\ Gyr^{-1}$) limits for the SF efficiency. The thin line represents the best model without Ba production in massive stars.

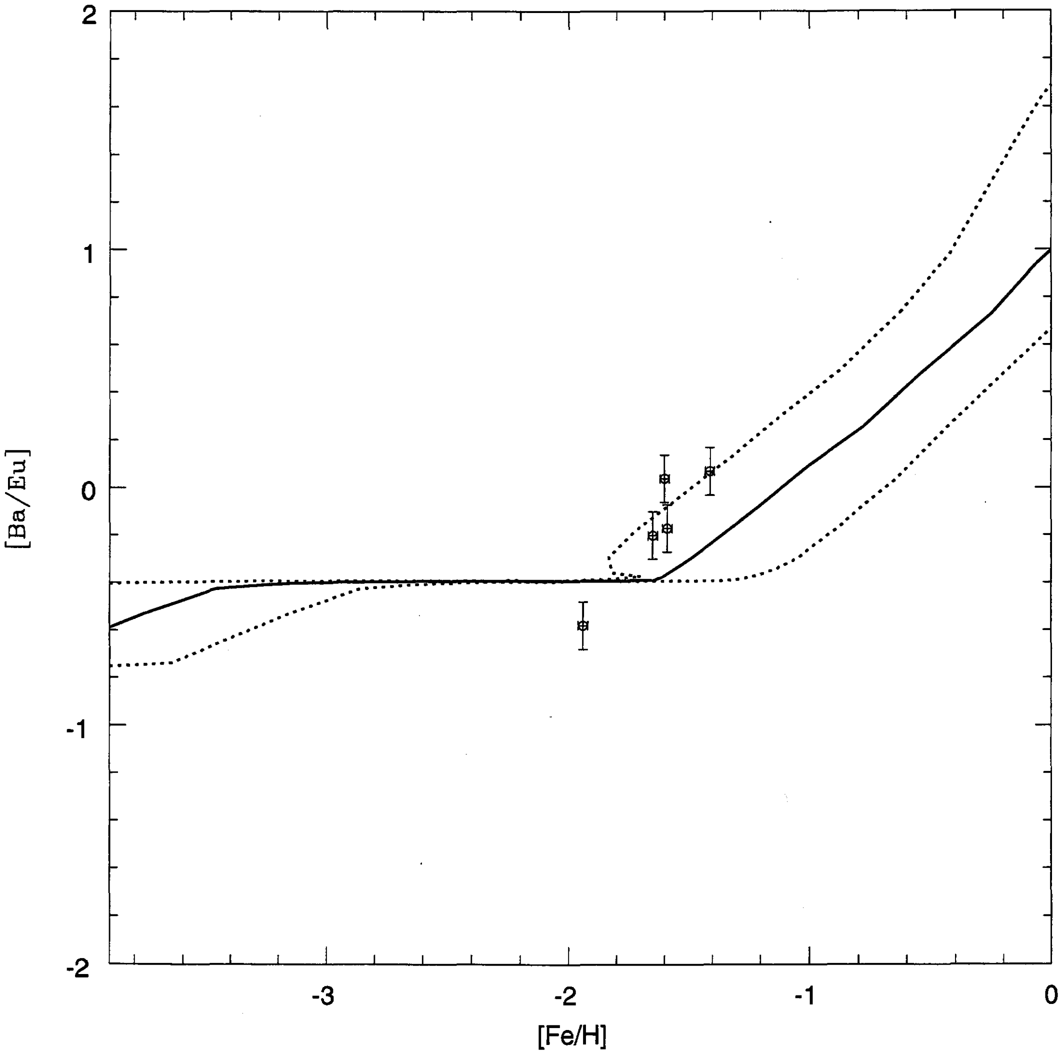

Figure 5.9. [Ba/Eu] vs. [Fe/H] observed in Carina dSph galaxy compared to the predictions of the chemical evolution model for Carina. The solid line represents the best model (ν = 0.1 Gyr^{-1}, w_i = 7) and the dotted lines the lower (ν = 0.02 Gyr^{-1}) and upper (ν = 0.4 Gyr^{-1}) limits for the SF efficiency.

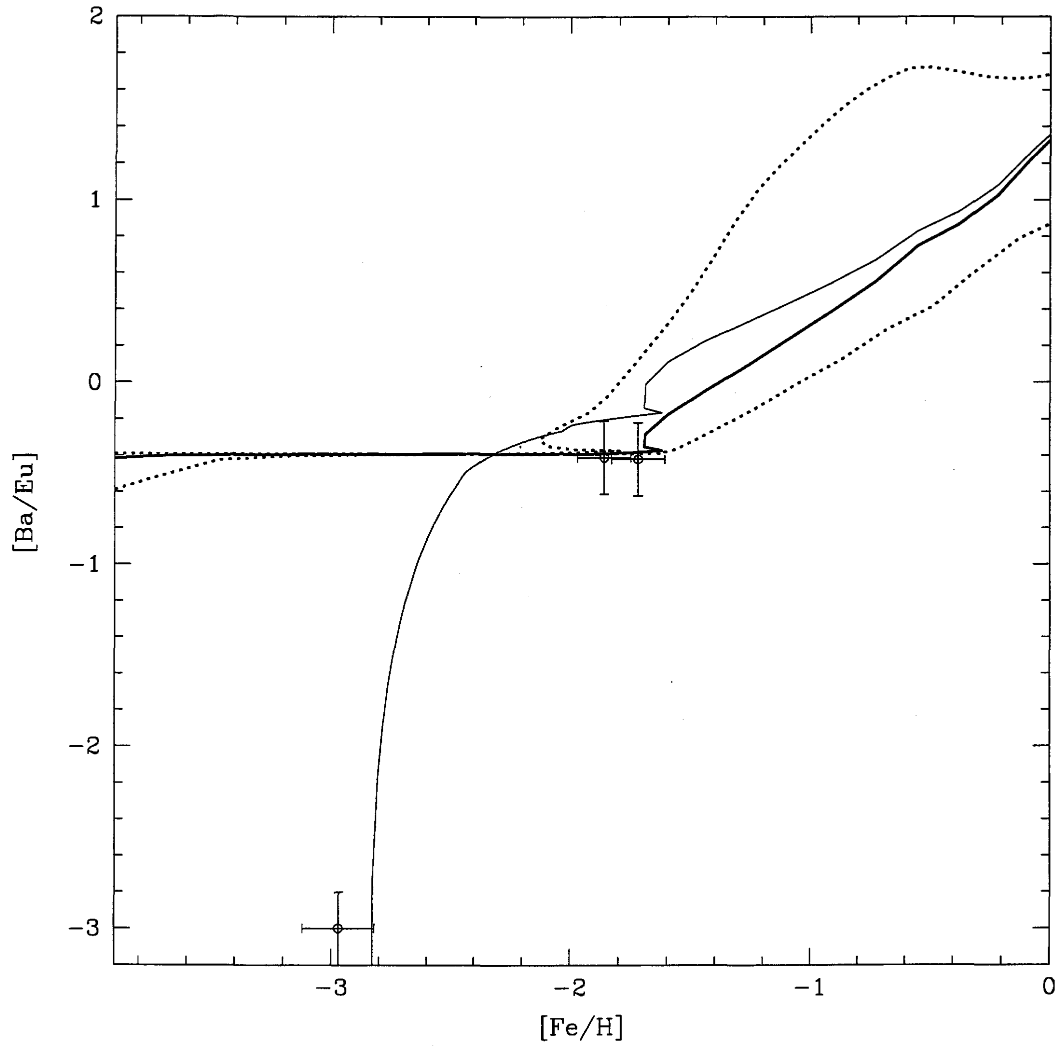

Figure 5.10. [Ba/Eu] vs. [Fe/H] observed in Draco dSph galaxy compared to the predictions of the chemical evolution model for Draco. The solid line represents the best model (ν = 0.03 Gyr^{-1}, w_i = 6) and the dotted lines the lower (ν = 0.005 Gyr^{-1}) and upper (ν = 0.1 Gyr^{-1}) limits for the SF efficiency. The thin line represents the best model without Ba production in massive stars.

5.3.3 The ratio [Ba/Eu]

The comparison between the observed [Ba/Eu] as a function of [Fe/H] and the predicted curves for the four dSph galaxies is shown in Figures 5.9 to 5.12. The models predict a similar pattern for all four galaxies: an almost constant sub-solar value at low metallicities ([Fe/H] < -1.7 dex) and, after that, a strong increase. This pattern is explained again by the adopted nucleosynthesis and by the effect of the galactic wind on the SFR and, consequently, on the production of Ba and Eu. At the early stages of evolution, the high mass stars provide the major contribution to the enrichment of the ISM medium. Since Ba and Eu are both produced by the r-process taking place in massive stars, they both are injected in the ISM when the gas metallicity is still low. The difference is that Eu is considered to be a pure r-process element, while the fraction of Ba that is produced by the r-process is low and its bulk originates instead from LMS. This fact translates into the sub-solar pattern observed in the predicted curves: more Eu than Ba is injected in the ISM at low metallicities, at an almost constant rate. When the LMS start to die and the first SNe Ia start exploding the scenario changes significantly. The LMS inject a considerable amount of Ba into the ISM causing an increase in the [Ba/Eu] ratio. Besides that, the energy released by the SNe Ia contributes to the onset of the galactic wind. Since the wind is very intense, it removes from the galaxy a large fraction of the gas reservoir which feeds the SF. Consequently, the SFR drops down considerably and also the production of Eu by massive stars, because the number of new formed stars is almost negligible. Barium, on the other hand, continues to be produced and injected in the ISM by the LMS (s-process). This fact induces the increase of [Ba/Eu] to be even more intense, as one can see in the predicted curves (Figures 5.9 to 5.12).

The observed trend is very well reproduced by the predicted curves in all four galaxies, especially in the case of Carina and Sculptor (Figures 5.9 and 5.11, respectively). The abundance pattern of these two galaxies not only exhibits the "plateau" at low metallicities, but also the sudden observed increase of [Ba/Eu] after the onset of the wind, suggesting that the adopted nucleosynthesis prescriptions for both Ba and Eu are appropriate and that the scenario described by the chemical evolution models is suitable to explain the evolution of these galaxies. In the case of Draco and Ursa Minor (Figures 5.10 and 5.12, respectively), there are no stars with metallicities larger than [Fe/H] $\sim$ -1.7 dex, the one characteristic for the onset of the galactic wind. Therefore, one cannot verify if this scenario (after the occurrence of the wind) holds also for these systems. However, the "plateau" is very well reproduced,

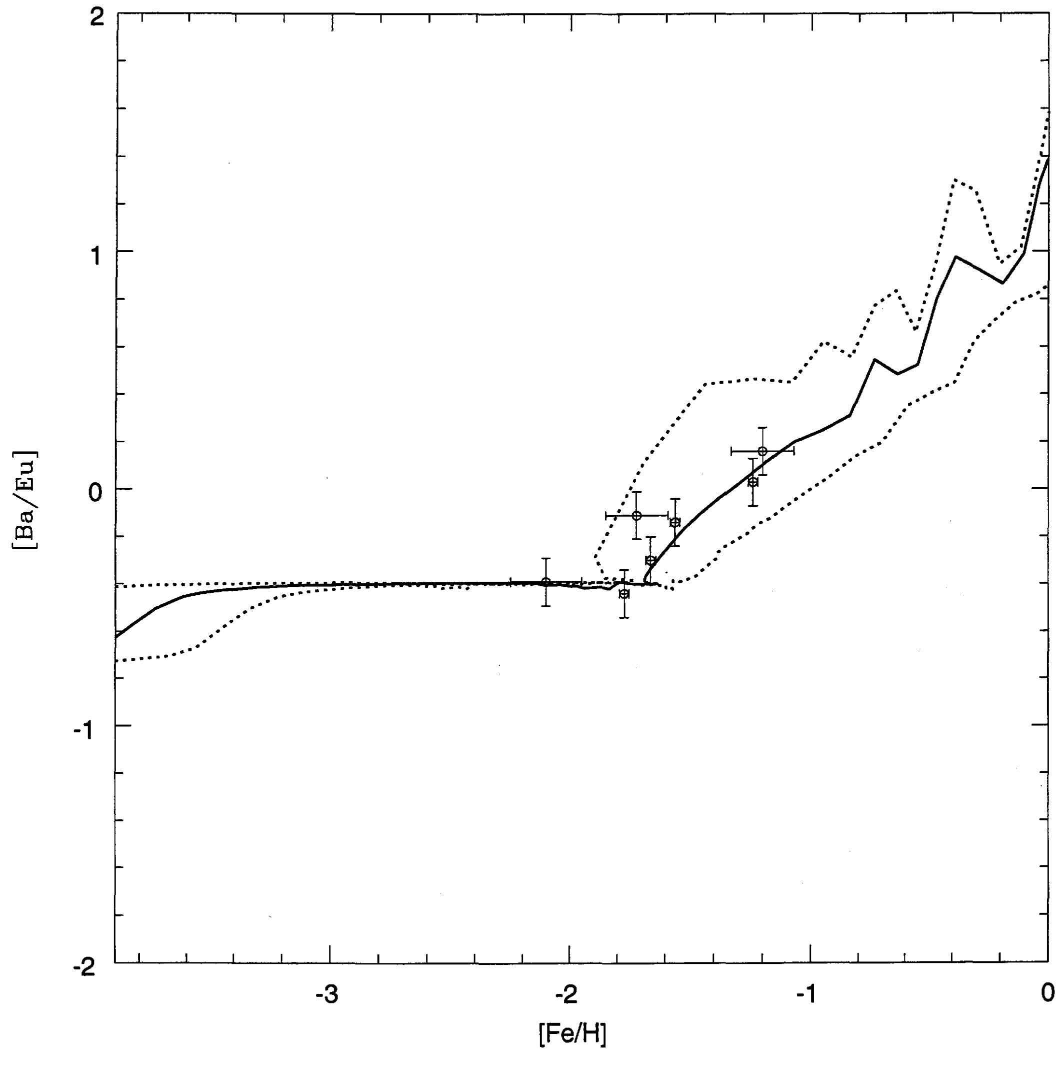

Figure 5.11. [Ba/Eu] vs. [Fe/H] observed in Sculptor dSph galaxy compared to the predictions of the chemical evolution model for Sculptor. The solid line represents the best model ($\nu = 0.2\ Gyr^{-1}$, $w_i = 13$) and the dotted lines the lower ($\nu = 0.05\ Gyr^{-1}$) and upper ($\nu = 0.5\ Gyr^{-1}$) limits for the SF efficiency.

even though there is some dispersion in the data, especially in the case of Ursa Minor.

It is important to stress that the predicted [Ba/Eu] reproduces all the observed trends, and that no star, given the uncertainties (with the exception of Draco 119, which exhibits a very uncertain value due to the limits on Ba and Eu abundances), lies outside the predictions, as it was the case for the two stars with very low [Ba/Fe]. This fact suggests strongly that the outsider stars must be examined separately.

5.3.4 The Sagittarius dSph galaxy

In this section, we present the predictions for [Ba/Fe], [Eu/Fe] and [Ba/Eu] as functions of [Fe/H] in Sagittarius dSph galaxy. Even though there are only two stars (Bonifacio et al. 2000) observed with Ba and Eu, it is interesting to compare the predictions of the models to the data and to analyze how these ratios would behave in this dSph galaxy. As mentioned in LM04, the Sagittarius dSph galaxy exhibits chemical properties which distinguish this galaxy from the other Local Group dSph galaxies. In particular, the SF efficiency (required to reproduce the observed [α/Fe] ratios) and the predicted metallicity distribution of this galaxy differ a lot from the other dSph galaxies analyzed - Draco, Carina, Ursa Minor, Sextan and Sculptor - being more similar to the values assumed for the Milky Way disc. The required SF efficiency is much higher (ν = 1 - 5 Gyr^{-1} compared to ν = 0.01 - 0.5 Gyr^{-1}) and the stellar metallicity distribution exhibits a peak at higher metallicities ([Fe/H] $\sim$ -0.6 dex) than the other dSph galaxies ([Fe/H] $\sim$ -1.6 dex) and close to the one from the solar neighborhood. As a consequence, one would expect also [Ba/Fe], [Eu/Fe] in Sagittarius to be different from the patterns observed in the other four dSph and more similar to those observed in the metal-poor stars of the Milky Way.

In order to predict the evolution of Ba and Eu as functions of Fe, we made use of the Sagittarius dSph model as described in LM04, without any changes in the most important parameters, such as SF efficiency and wind efficiency, and with the same nucleosynthesis prescriptions adopted for the other dSph galaxies. This procedure is justified by the fact that no modifications were required for the LM04 models of the other galaxies (Carina, Draco, Sculptor and Ursa Minor) to fit the observed [Ba/Fe], [Eu/Fe] and [Ba/Eu].

In Figure 5.13, the predictions for Sagittarius dSph galaxy model for [Ba/Fe], [Eu/Fe] and [Ba/Eu] are shown in comparison with the data. As one can clearly see, all three predicted ratios reproduce very well the data and exhibit significant differences (in particular

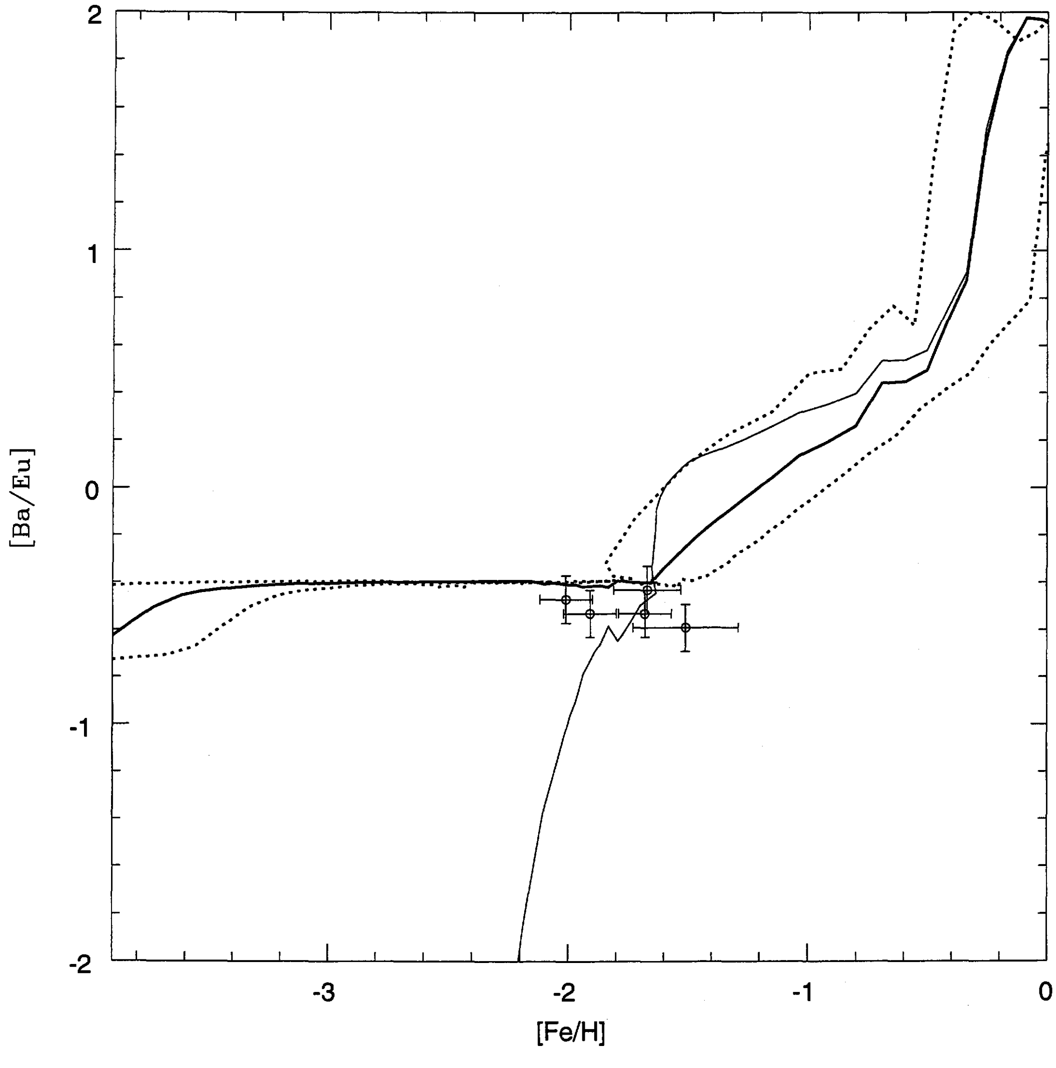

Figure 5.12. [Ba/Eu] vs. [Fe/H] observed in Ursa Minor dSph galaxy compared to the predictions of the chemical evolution model for Ursa Minor. The solid line represents the best model ($\nu = 0.2\ Gyr^{-1}$, $w_i = 10$) and the dotted lines the lower ($\nu = 0.05\ Gyr^{-1}$) and upper ($\nu = 0.5\ Gyr^{-1}$) limits for the SF efficiency. The thin line represents the best model without Ba production in massive stars.

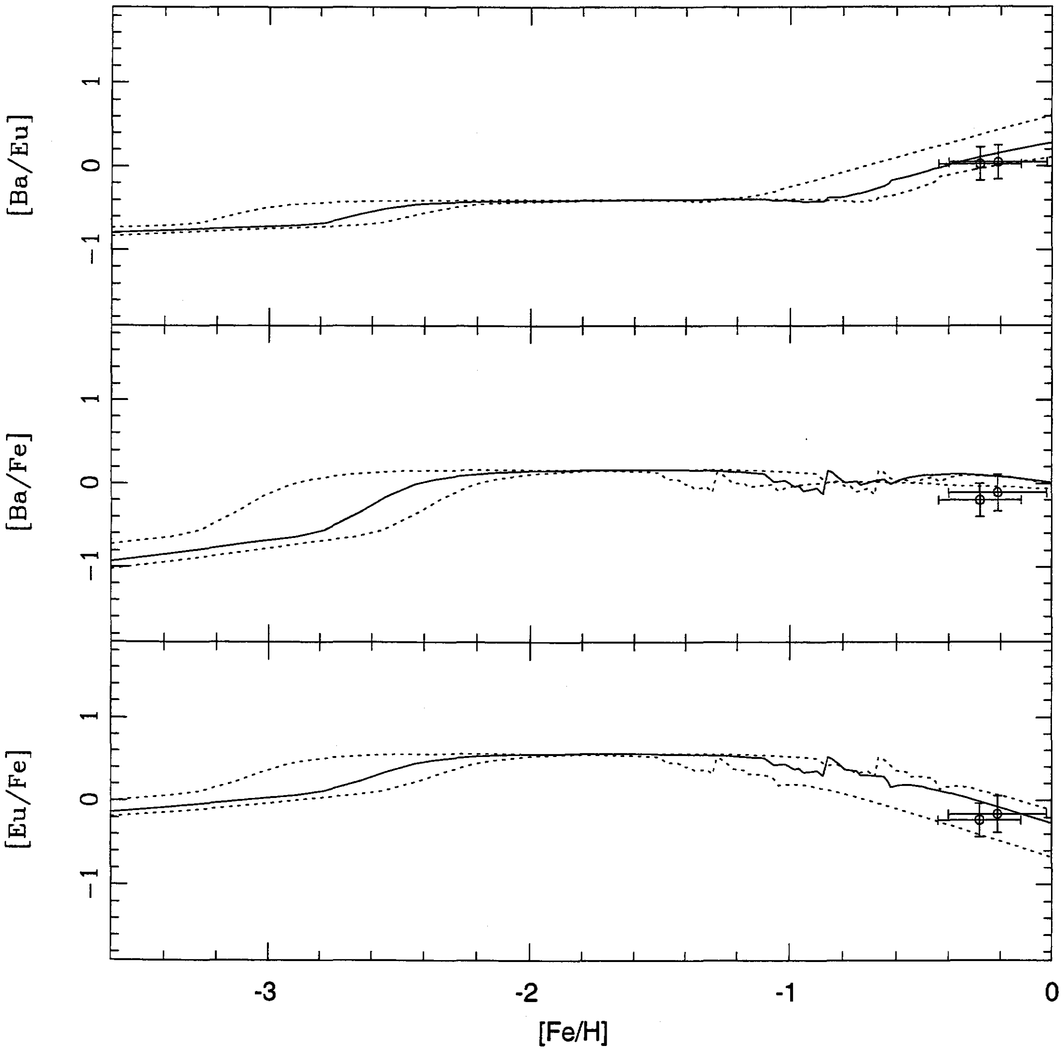

Figure 5.13. The predicted evolution of Ba and Eu as function of [Fe/H] for Sagittarius dSph galaxy compared with the data. The solid line represents the best model ($\nu = 3\ Gyr^{-1}$, $w_i = 9$) and the dotted lines the lower ($\nu = 1\ Gyr^{-1}$) and upper ($\nu = 5\ Gyr^{-1}$) limits for the SF efficiency.

[Ba/Fe]) when compared to the predictions (and observations) for the other dSph galaxies. The decrease in the [Eu/Fe] at relatively high metallicities ([Fe/H] $\sim$ -1.7 dex) observed in the four dSph galaxies, and attributed to the effect of the galactic wind on the SFR, is less intense in the case of Sagittarius. Moreover, one cannot see the high values of [Ba/Fe] at low metallicities ([Fe/H] $<$ -3.0 dex), which were explained as an effect of the low SF efficiency. Also, the predicted [Ba/Eu] ratios do not show the almost constant "plateau" observed at low and intermediate metallicities in the other dSph galaxies. All these differences can be also found when one compares the pattern of these ratios in dSph galaxies with those in the metal-poor stars of the Milky Way. The differences between the predictions of Sagittarius and the other dSph and the similarities with the Milky Way can be attributed to the high values of the SF efficiency adopted for Sagittarius when compared to the other dSph galaxies. These high values, in fact, are more similar to the values generally adopted for the solar neighborhood (Chiappini, Matteucci & Gratton, 1997). Consequently, one could suggest that the chemical evolution of Sagittarius follows roughly that of the Milky Way disc at the solar neighborhood in contrast to the other dSph Galaxies, which exhibit a much slower chemical evolution.

Chapter 6

Comparison between the evolution of Ba, La, Eu and Y in the Milky Way and in the dwarf spheroidal galaxy Sculptor

> *"Passion is like the lightning, it is beautiful,*
> *and it links the earth to heaven, but alas it blinds!"*
> *by H. Rider Haggard*

In this chapter we use the results of the previous chapters, in particular chapter 2 and chapter 5, to compare the results of the Milky Way to those of the dwarf spheroidal galaxies. In particular, we choose Sculptor as typical dwarf spheroidal galaxy. We also include Y and La in our discussion, besides Eu and Ba discussed in the previous chapter. We show how in these two different systems, the Milky Way and Sculptor, the results of the chemical evolution predicts different abundance ratios and these results are confirmed by the observational data. We concentrate on the ratios of neutron capture elements Y-Ba-La-Eu, which are the neutron capture elements measured in Sculptor.

6.1 Results

6.1.1 Ratios of neutron capture elements over iron

In Fig. 6.1 we plot [Y/Fe] vs [Fe/H]. The data for Sculptor are in a small range of [Fe/H] and present a quite large scatter. Nevertheless, Sculptor has a mean ratio [Y/Fe] below the mean ratio of the Milky Way in the same range of [Fe/H], and this confirms the result of our model for Sculptor. The model predicts a strong decrease of the ratio [Y/Fe] due to the galactic wind which takes place for [Fe/H] > -2.

The steepness of the decrease depends on the s-process contribution to each neutron capture elements. The s-process enrichment due to low-mass stars is delayed with respect to the galactic wind time for Sculptor; as a result, the elements with a contribution by the s-process show a smaller decrease of their ratios relative to iron.

In fact, the predictions of the model for the ratio of [Y/Fe], and yttrium has a contribution of s-process , show a smaller decrease than the results for the ratio of europium over iron (see Fig. 6.2).

Europium has a negligible production by s-process and the model predicts a very steep decrease for its ratio over iron in Sculptor and this well fits the observational data for this galaxy whereas the data for the Milky Way do not show this so steep decrease at this stage.

For barium and lanthanum the results are similar to those of yttrium; this is in agreement with the data of Sculptor (see Fig. 6.3, 6.4), even if in these cases there are not significant differences with the data of the Milky Way.

The two different models, which share the same nucleosynthesis, give different results for the two systems due to the different conditions in which the chemical evolution take place, as the presence of a galactic wind in Sculptor, the different star formation history and the different efficiency for star formation (for others details see chapter 2 and 5).

It is worth noting that the main difference in the [Y, Ba, La, Eu/Fe] in Sculptor (and in general in the dSph galaxies) and in the Milky Way is due to the time delay model, namely the different timescales with which different elements are produced, in conjunction with different star formation histories. In the figures 6.1, 6.2, 6.3 and 6.4, we see that the abundance ratios in Sculptor are higher than in the Milky Way at very low metallicities ([Fe/H] < -3.0 dex). This is due to the fact that [Fe/H] grows at a different rate in Sculptor and in the Milky Way. In particular, in Sculptor the SFR is lower than in the Milky Way, thus a given [Fe/H]

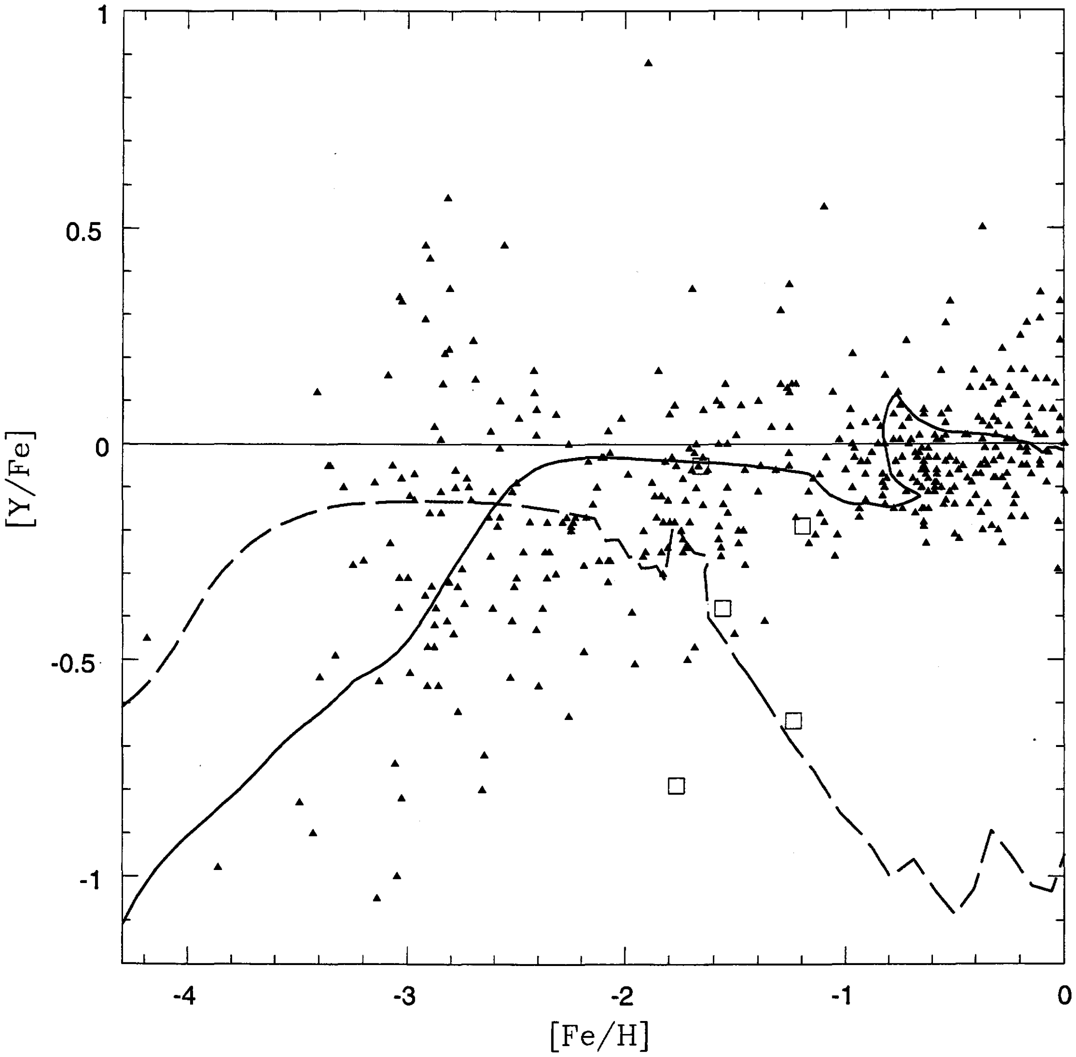

Figure 6.1. [Y/Fe] vs [Fe/H]: the red dots are the observational data for the for the Milky Way, whereas the blue open squares are the data for Sculptor. The results of the model for the Milky Way are plotted in red solid line and the results for Sculptor in blue dashed line.

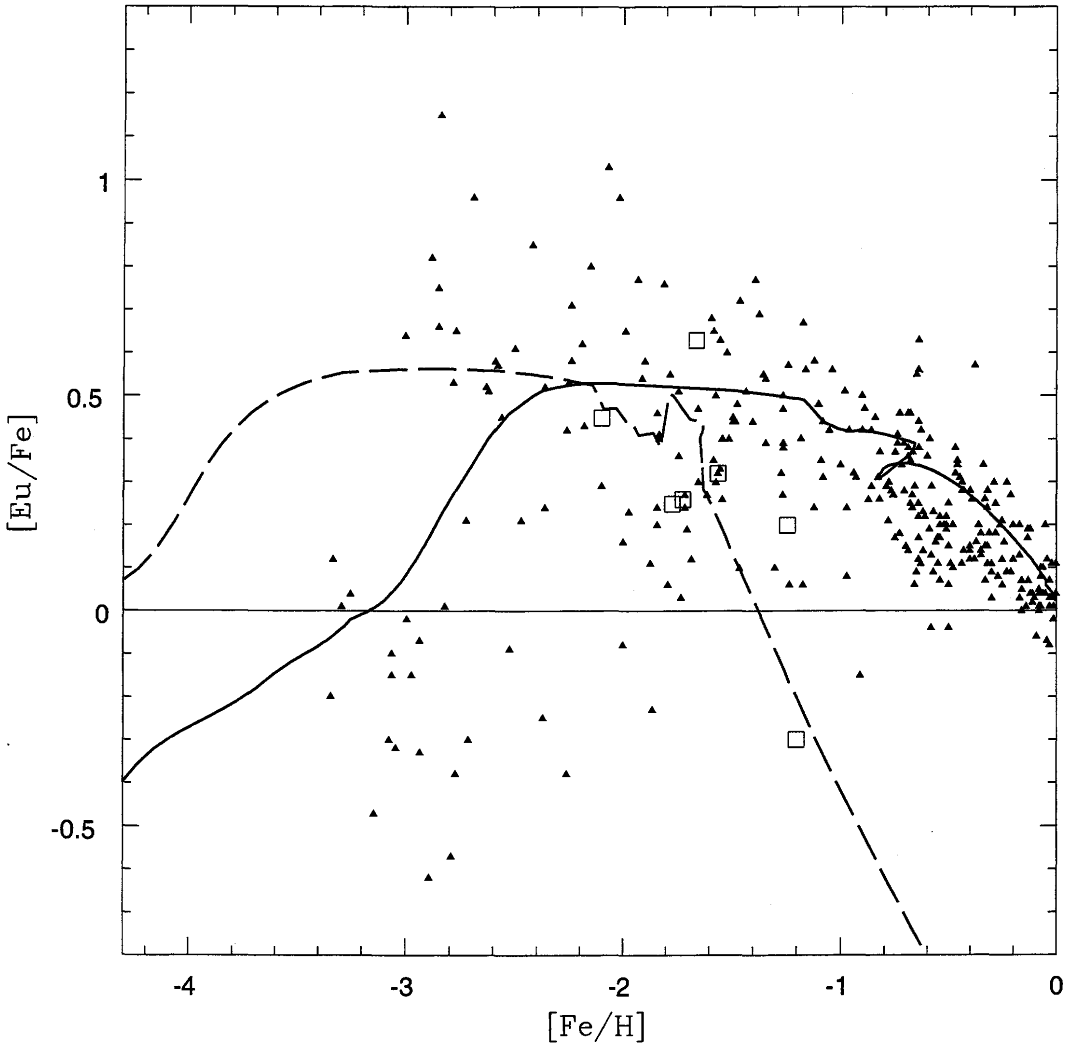

Figure 6.2. [Eu/Fe] vs [Fe/H]: the red dots are the observational data for the Milky Way, whereas the blue open squares are the data for Sculptor. The results of the model for the Milky Way are plotted in red solid line and the results for Sculptor in blue dashed line.

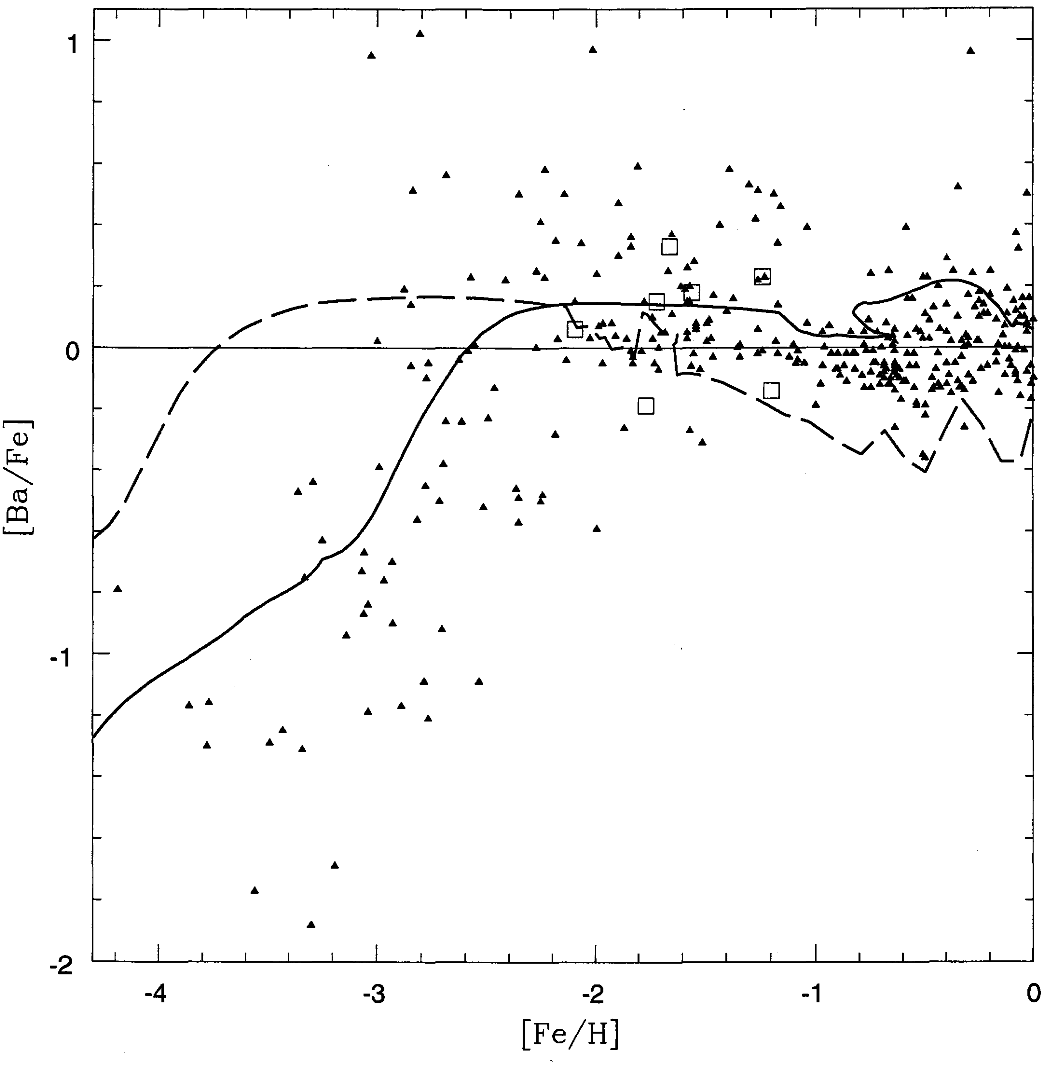

Figure 6.3. [Ba/Fe] vs [Fe/H]: the red dots are the observational data for the Milky Way, whereas the blue open squares are the data for Sculptor. The results of the model for the Milky Way are plotted in red solid line and the results for Sculptor in blue dashed line.

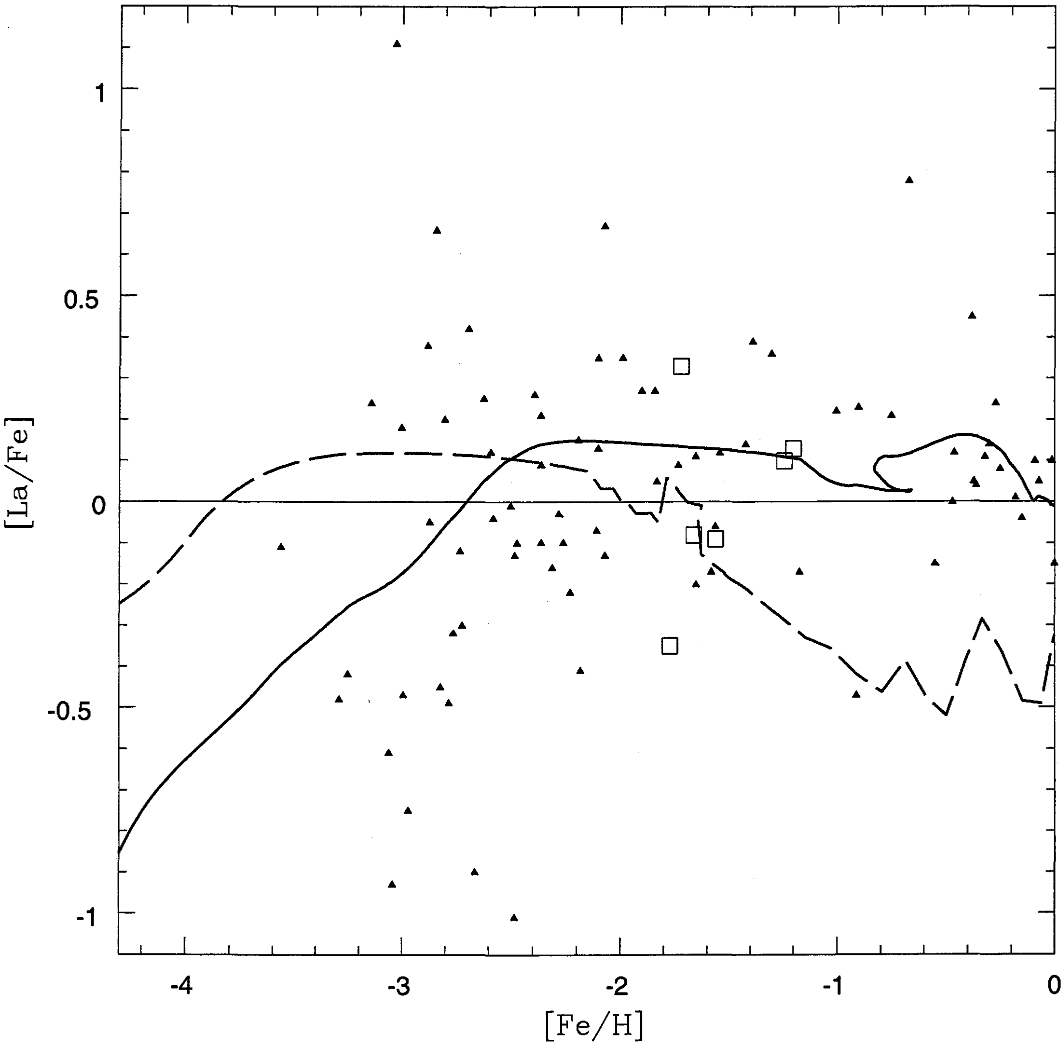

Figure 6.4. [La/Fe] vs [Fe/H]: the red dots are the observational data for the Milky Way, whereas the blue open squares are the data for Sculptor. The results of the model for the Milky Way are plotted in red solid line and the results for Sculptor in blue dashed line.

corresponds to different cosmic epochs in the two systems.

6.1.2 Neutron capture elements ratios: [Y/Eu] - [Ba/Eu] - [La/Eu] - [Ba/Y] - [La/Y]

In Fig.6.5 we show the ratio [Ba/Eu]. The trends of the data in the two systems are quite different. In the Milky Way, the ratio is almost flat up to [Fe/H]$\sim$ -1 at a value of about [Ba/Eu]$\sim$ -0.5, then it increases up to the solar value, in agreement with our model and it is due to s-process enrichment by low mass stars. In the dSph galaxy Sculptor the enrichment by s-process has a different timescale. When the low mass stars start to die and enrich the interstellar medium, the [Fe/H] in Sculptor is only $\sim$ -2 dex. So the ratio [Ba/Eu] in our models starts to increase at lower metallicities in Sculptor than in the Milky Way and this is what is observed in the data. This is a remarkable result and we give here for the first time this kind of interpretation.

For lanthanum we obtain the results shown in Fig. 6.6. As expected, the models give results very similar to those of Ba, being the nucleosynthesis similar. The observational data for the Milky Way are few, but the trend resembles the one of the barium. The trend of the data for Sculptor is the same as for Ba and the model reproduces this trend.

In the case of yttrium, the results of the model for Sculptor do not show a large difference compared to the results for the Milky Way (see Fig. 6.7). However, the two observational points for Sculptor with the highest [Fe/H] show a large difference, so it is hard to say which is the real observational trend and if we take the mean value of the two points the results are quite good.

In Fig. 6.8, 6.9 we show the ratios [Ba/Y] and [La/Y]. Concerning the Milky Way data, the model fits well the observational data for the ratios [Ba/Y] and for [La/Y], even if the data for [La/Y] are few. We note that the results for the [Ba/Y] and for [La/Y] ratios for Sculptor increase for [Fe/H]> -2. The observational data for Sculptor show substantially the same behaviors, even if we find again that the two observational data with the highest [Fe/H] show discrepancy and the model passes about the mean value of the two data.

Therefore, we conclude that the chemical evolution models, both the one for the Milky Way and the one for Sculptor, well fit the observational data. Moreover, they are able to explain why the abundance ratios for neutron capture elements in the two systems are different for the same [Fe/H], in terms of different SFR history, star formation efficiencies

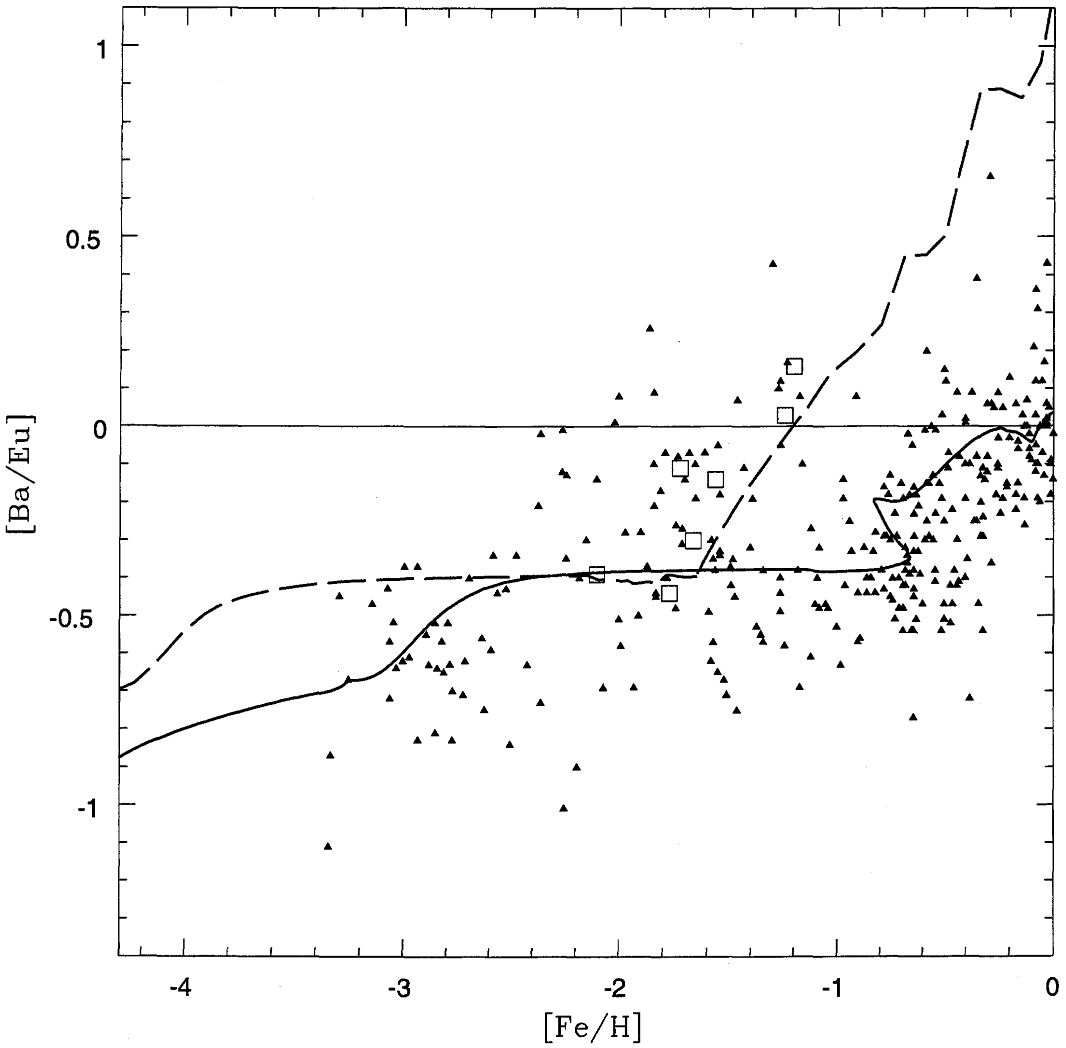

Figure 6.5. [Ba/Eu] vs [Fe/H]: the red dots are the observational data for the Milky Way, whereas the blue open squares are the data for Sculptor. The results of the model for the Milky Way are plotted in red solid line and the results for Sculptor in blue dashed line.

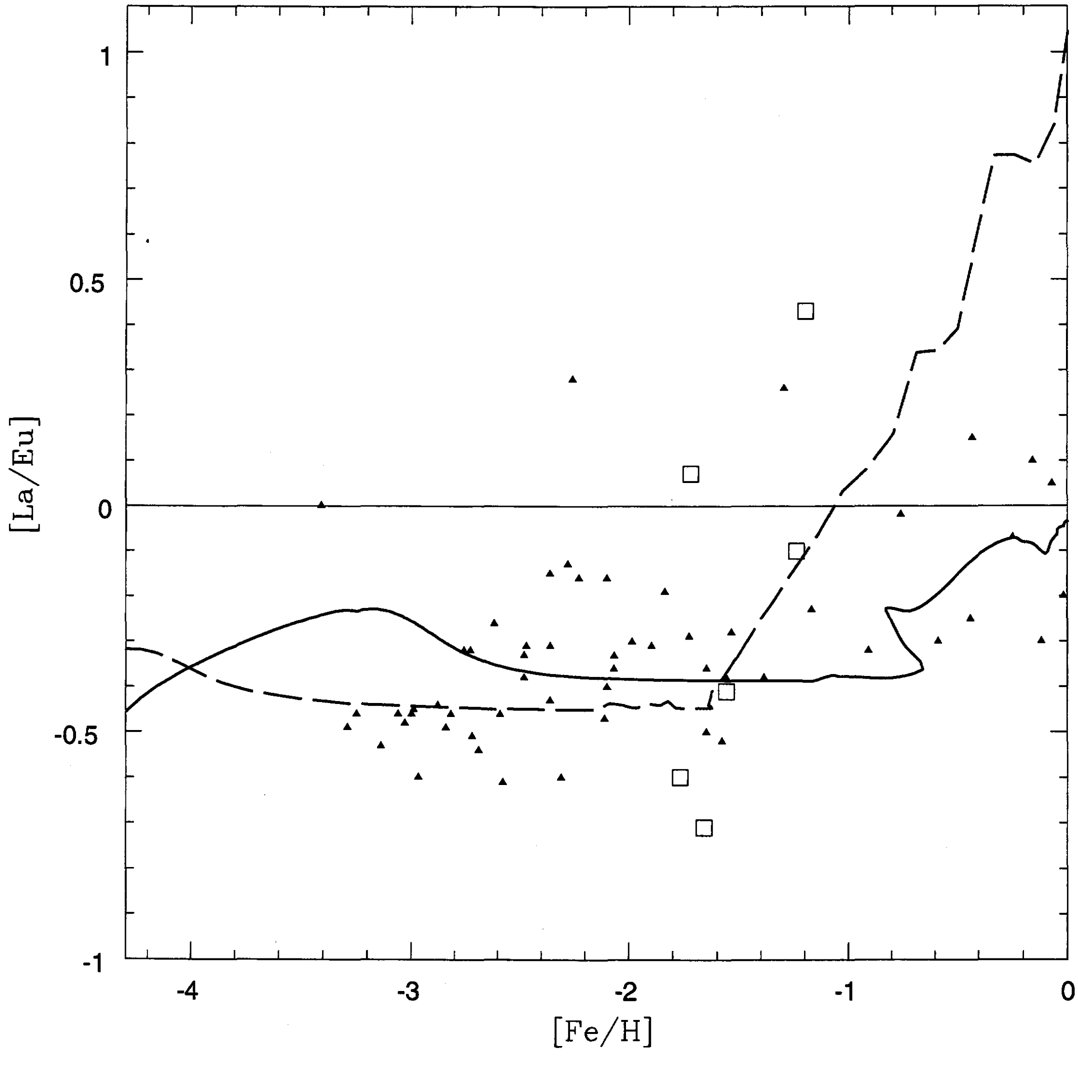

Figure 6.6. [La/Eu] vs [Fe/H]: the red dots are the observational data for the Milky Way, whereas the blue open squares are the data for Sculptor. The results of the model for the Milky Way are plotted in red solid line and the results for Sculptor in blue dashed line.

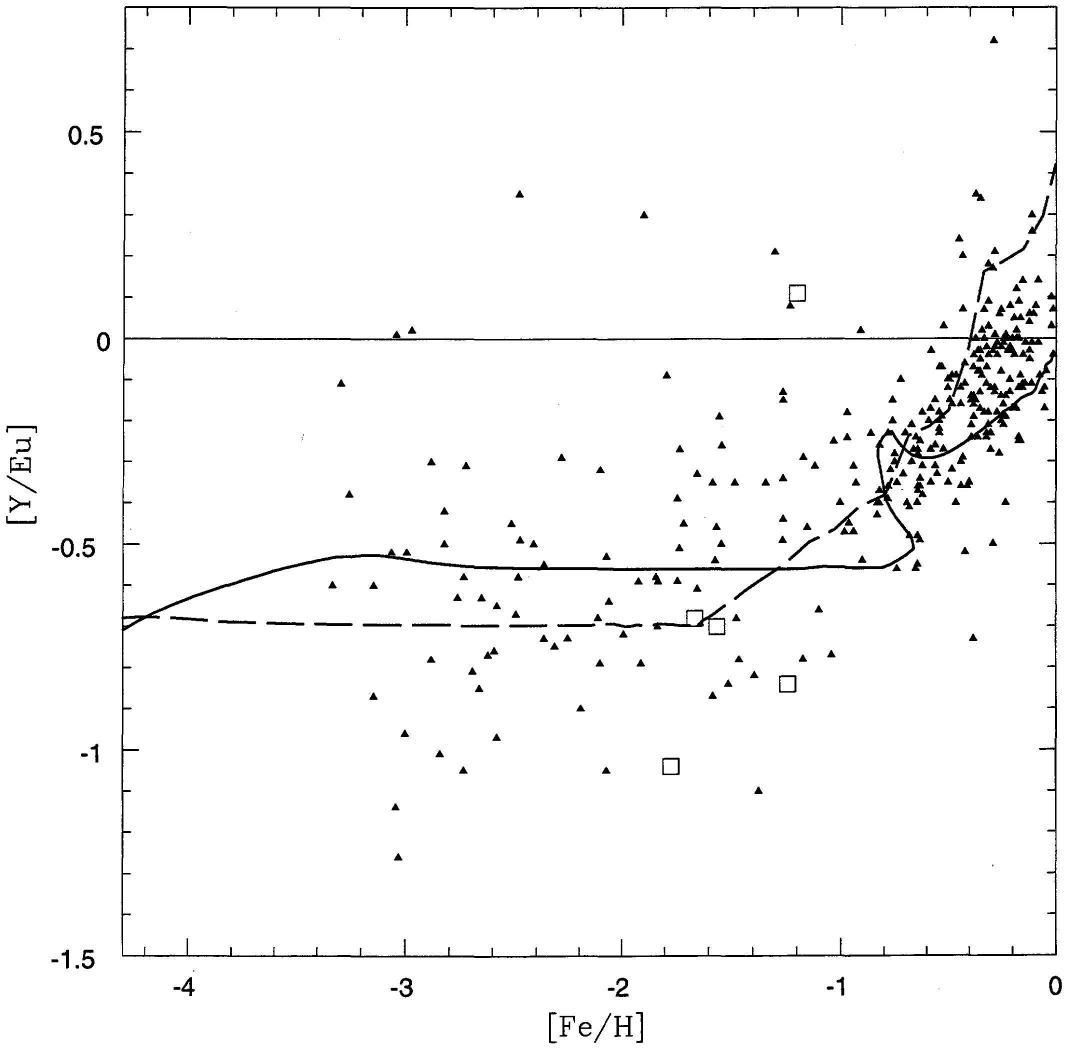

Figure 6.7. [Y/Eu] vs [Fe/H]: the red dots are the observational data for the Milky Way, whereas the blue open squares are the data for Sculptor. The results of the model for the Milky Way are plotted in red solid line and the results for Sculptor in blue dashed line.

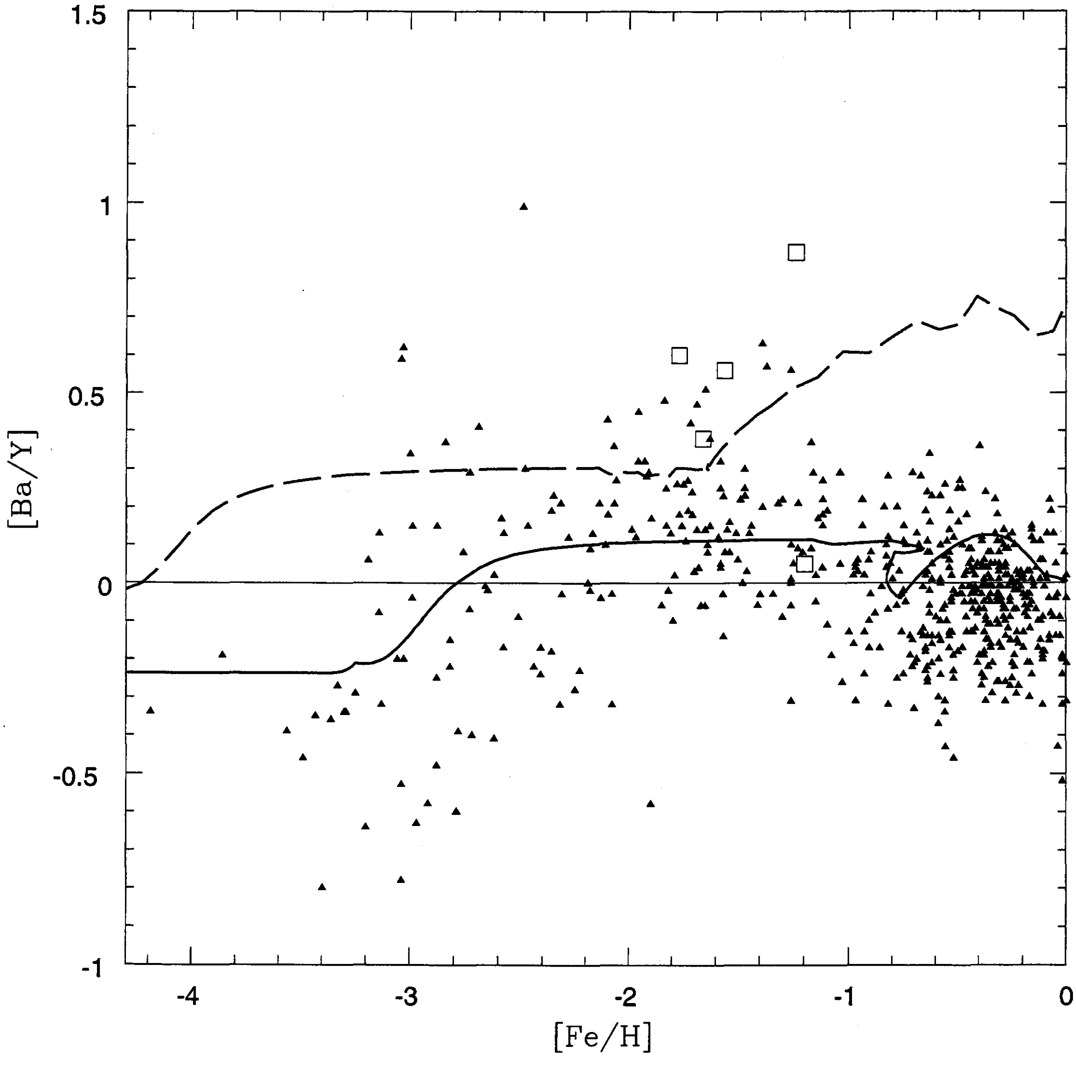

Figure 6.8. [Ba/Y] vs [Fe/H]: the red dots are the observational data for the Milky Way, whereas the blue open squares are the data for Sculptor; The results of the model for the Milky Way are plotted in red solid line and the results for Sculptor in blue dashed line.

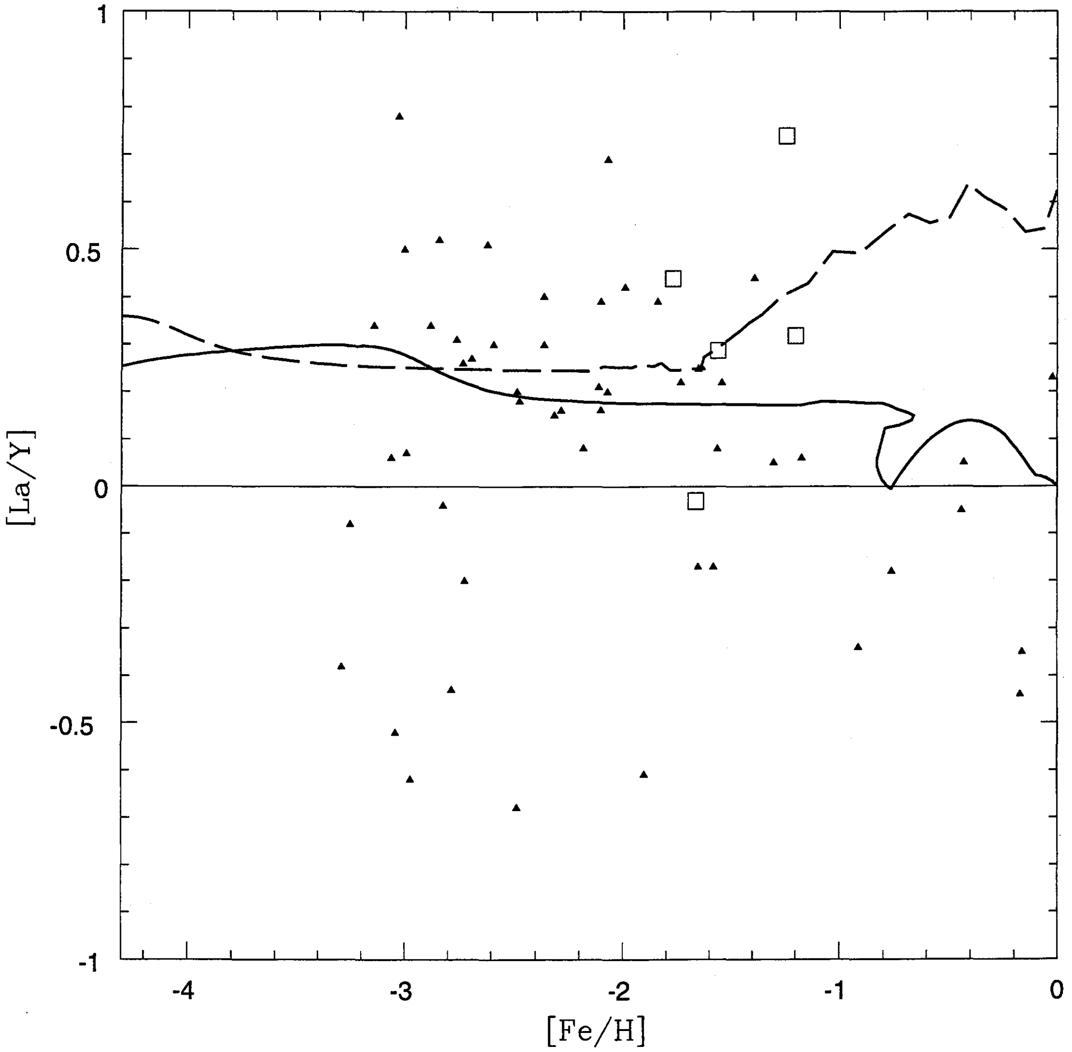

Figure 6.9. [Ba/Y] vs [Fe/H]: the red dots are the observational data for the Milky Way, whereas the blue open squares are the data for Sculptor; The results of the model for the Milky Way are plotted in red solid line and the results for Sculptor in blue dashed line.

and galactic winds.

Chapter 7

Conclusions

> *"... it is possible to make even Venus herself vanish from the firmament by a scrutiny too sustained, too concentrated, or too direct."*
>
> *by Edgar Allan Poe*

7.1 Chemical evolution in the solar vicinity

In the first part of this work, the main goal was to follow the evolution of neutron capture elements by means of a chemical evolution model reproducing the abundance trends for other elements. We used the Chiappini et al. (1997) model in its latest version as described in Chiappini et al. (2003) and François et al. (2004). We have used empirical yields for stars with mass $> 8M_{\odot}$, producing r-process elements. For the r-process elements there are not solid theoretical yields, since the mechanism involved in their production, the so-called r-process, it is still not well understood. We conclude that Ba, La, Sr, Y and Zr need two components: an s-process main component originating in low mass stars (1-3 $M_{\odot}$) plus an r-component originating in stars in the range 10-30$M_{\odot}$. This range is different from the one suggested by Travaglio et al. (1999) and Travaglio et al. (2004) and it has been obtained by requiring the best fit of the new and accurate data. For Eu we estimate that it is mainly produced by an r-process and that stars in the same mass range, 10-30$M_{\odot}$, should be considered as the progenitors of this element.

The nearly constant value of the ratio [Ba/Eu] produced in massive stars by the r-process can be used to estimate the fraction of barium in the solar abundance produced by the slow process. We have obtained in this way a fraction that is slightly different from the previous results: 60% instead of 80%. The yields that we derived and even the fact that the ratio of the r- process production of Eu and Ba seems to be be nearly constant could be very useful in studies involving nucleosynthesis in stellar models and even in nuclear physics studies. The open question remains the observed, and probably real, large spread in the [el/Fe] ratios for the neutron capture elements at [Fe/H]. Our homogeneous model can in fact reproduce the mean trend of the the data but not the spread.

7.2 Abundance gradients in the Milky Way

The aim of this chapter was to compare new observational data on the radial gradients for 19 chemical elements (including s- and r-process elements) with the predictions of our chemical evolution model for the Milky Way. This model has been tested on the properties of the solar vicinity and contains a set of yields which best fits the abundances and abundance ratios in the solar vicinity, as shown in François et al. (2004).

The bulk of observational data comes from the abundances derived in a large number of Cepheids observed by 4AL. For the first time with these data it has been possible to verify the predictions for many heavy elements with statistical validity.

The comparison between model predictions and observational data showed that our model well reproduces the gradients of almost all the elements that we analyzed. Since abundance gradients can impose strong constraints both on the mechanism of galaxy formation, in particular of the galactic disk, and on the nucleosynthesis prescriptions, we can conclude that:

- The model for the Milky Way disk formation, assuming an inside-out building-up of the disk, as suggested originally by Matteucci & François (1989), can be considered successful; for almost all the considered elements, we find a good fit to the observational data ranging from 5 to 17 kpc. In particular, the model assuming a constant total surface mass density for the halo best fits the data of Cepheids. At large galactocentric distances the halo mass distribution influences the abundance gradients (see Chiappini et al. 2001).

- In our chemical evolution model we adopt a threshold in the gas density for star formation in the disk of $7 M_{\odot} pc^{-2}$, whereas for the halo phase we have several options with and without a threshold. The threshold in the halo, when considered, is $4M_{\odot}pc^{-2}$. We also assume a constant surface mass density for the halo or variable with galactocentric distance. This is important for the gradients at very large galactocentric distances, where the enrichment from the halo predominates over the enrichment occurring in the thin disk, thus influencing the abundances at such large distances. We conclude that to reproduce the flat gradients suggested by the abundance measurements at large galactocentric distances, we need to assume a constant density distribution and a threshold in the star formation during the halo phase. However, there are still many uncertainties in the data at very large galactocentric distances and only more data will allow us to draw firm conclusions on this important point.

- By means of the assumed nucleosynthesis prescriptions, we have successfully reproduced the abundance gradients of each specific element, as well as the [el/Fe] vs [Fe/H] relations in the solar neighborhood, for both neutron capture elements and for α- and iron peak elements.

7.3 Inhomogeneous model for the Galactic halo

In this chapter we tried to solve the problem of the spread at low metallicity of the [el/Fe] ratios for neutron capture elements. We developed a new model for the chemical evolution of the halo in the Milky Way. We showed in this model that a random birth of stellar masses, coupled with the different mass ranges responsible for the production of α-elements and neutron capture elements, respectively, can explain the large spread in the abundances of metal poor stars for neutron capture elements and the smaller spread for α-elements. We used for this model the same parameters of the homogeneous one. We adopted this point of view because these parameters have been already constrained to give good results compared to the observational data at higher metallicities. In fact, toward high metallicities ([Fe/H]>-2.0 dex) the model naturally gives results compatible with the homogeneous model. However, this set of parameters is a starting point and the model still needs a better investigation of the parameter space; in particular, for what concern the early galactic stages, the model predicts a too fast increase of the [Fe/H] and produces a too small number of stars with a metallicities [Fe/H]< -3. Moreover this new model generates a too large number of metal free stars. To avoid these problems a different and slower star formation history can be used, in order to provide a smoother increase of the metallicities. To solve the problem of the metal free stars, a top-heavy IMF can be applied for the very first period. In fact, many theoretical models for the metal free stars predict the existence of a top-heavy IMF (see Larson 1998, Abel, Bryan & Norman 2000, Hernandez & Ferrara 2001, Nakamura & Umemura 2001, Mackey, Bromm, & Hernquist 2003).

7.4 Dwarf spheroidal galaxies

In the last part of this work, we have applied the nucleosynthesis prescriptions for the neutron capture elements, derived in chapter 2 for the Milky Way, to five dSph galaxies, in order to verify the assumptions regarding the production of these elements. We have implemented these new nucleosynthesis prescriptions in a chemical evolution model, which was able to reproduce several observational constraints of the Local Group dSph galaxies (such as [α/Fe], present day gas mass, estimated final total mass, metallicity distribution). The model galaxies are characterized by the SF prescriptions, such as the number and the duration of the SF episodes and also by the wind efficiency. The prescriptions for the SF history are taken from the suggestion arising from their color-magnitude diagrams. In the chapter 5, we have compared the results of the chemical evolution of Ba and Eu in 5 dSph galaxies (Draco, Sculptor, Carina, Ursa minor and Sagittarius); in chapter 6 we have compared the chemical evolution of the dSph Sculptor with the one the Milky Way and in this case we have shown also the results for Y and La. The main conclusions can be summarized as follows:

- The observed [Eu/Fe], [Ba/Fe] and [Ba/Eu] ratios are very well reproduced by the models for Draco, Carina, Ursa Minor, Sculptor and Sagittarius with the same nucleosynthesis that we have used in the Milky Way. There is the exception of two stars (one in Draco and another in Ursa Minor) which exhibit very low values of [Ba/Fe] at low metallicities ([Fe/H] < -2.4 dex); these two stars could be explained by a model in which Ba is produced only by s-process occuring in stars with masses in the range 1 - 3 $M_{\odot}$, but they could be also anomalous stars.
- The evolution of [Y/Fe], [La/Fe], [Y/Eu], [La/Eu], [Ba/Y] and [La/Y] ratios, which we have followed only for the dSph Sculptor, confirms the goodness of the prescriptions also for these elements when we compare the results of the model to the observational data.

- The comparison between Sculptor and the Milky Way permits us to show the different predicted and observed values in these two systems. Although more data for the dSph galaxies are necessary, we can interpret these different ratios at a given metallicity as due to the much less efficient star formation that we need to adopt to reproduce the abundances of dSph galaxies, compared to the Milky Way. In the star formation regime adopted for the dSph galaxies, in fact, the metallicity increases more slowly and the different contributions for the enrichment of neutron capture elements in the ISM appear at lower metallicities than in the Milky Way.

- The dSph galaxies cannot be the building blocks of the Milky Way galaxy, being their chemical evolution and chemical composition very different. This cannot rule out that clumps of gas, progenitors of dSph galaxies in a isolate evolution, merged to our Galaxy at a very early stage; on the other hand, interactions between the Milky Way and dSph galaxies do exist as shown by the galaxy Sagittarius, which is gradually being disrupted by the tidal interaction with our Galaxy, as suggested also by the same chemical signature of Sagittarius and the globular cluster Palomar 12, which is nowadays in the halo of the Galaxy (Sbordone et al. 2006).

- We underline that only more data, possibly extended toward larger metallicities, and a robust statistical basis can confirm definitively our results.

Bibliography

[1] Abel T., Bryan G.L., Norman M.L., 2000, ApJ, 540, 39

[2] Anders E., Grevesse N., 1989, GeCoA, 53, 197

[3] Alibés A., Labay J., Canal R., 2001, A&A, 370, 1103

[4] Andrievsky S.M., Bersier D., Kovtyukh V.V. et al 2002, A&A 384, 140

[5] Andrievsky S.M., Kovtyukh V.V., Luck R.E. et al 2002, A&A 381, 32

[6] Andrievsky S.M., Kovtyukh V.V., Luck R.E. et al 2002, A&A 392, 491

[7] Andrievsky S.M., Luck R.E., Martin P. et al 2004, A&A 413, 159

[8] Argast D., Samland M., Gerhard O.E., Thielemann, F.-K., 2000, A&A, 356, 873

[9] Argast D., Samland M., Thielemann F.-K., Qian Y.-Z., 2004, A&A, 416, 997

[10] Arimoto N., Yoshii Y., 1987, A&A, 173, 23

[11] Arlandini C., Käppeler F., Wisshak K. et al., 1999, ApJ, 525, 886

[12] Asplund M., Grevesse N., Sauval A. J., 2005, ASPC, 336, 25A

[13] Ballero S.K., Matteucci F., Chiappini C., 2006, NewA, 11, 306

[14] Baraffe I., El Eid M.F., Prantzos N., 1992, A&A, 258, 357

[15] Beers T.C., Preston G.W., Shectman S.A., 1992, A.J., 103, 1987

[16] Beers T.C., Rossi S., Norris J.E., Ryan S.G., Shefler T., 1999, A.J., 117, 981

[17] Boissier S., Prantzos N., 1999, MNRAS, 307, 857

[18] Bonifacio P., Hill V., Molaro P., Pasquini L., Di Marcantonio P., Santin P., 2000, A&A, 359, 663

[19] Bonifacio P., Sbordone L., Marconi G., Pasquini L., Hill V., 2004, A&A, 414, 503

[20] Bono G., Marconi M., Cassisi S. et al. 2005, ApJ, 621, 966

[21] Burris D.L., Pilachowski C.A., Armandroff T.E. et al., 2000, ApJ, 544, 302

[22] Busso M., Gallino R., Lambert D.L., Travaglio, C., Smith V.V., 2001, ApJ, 557, 802

[23] Busso M., Gallino R., Wasserburg G.J., 1999, ARA&A ,37, 239

[24] Cappellaro E., Evans R., Turatto M., 1999, A&A, 351, 459

[25] Carney B.W., Wright J.S., Sneden C. et al., 1997, A.J., 114, 363

[26] Carigi L., Hernandez X., Gilmore G., 2002, MNRAS, 334, 117

[27] Carney B.W., Yong D., Teixera de Almeida M.L., Seitzer P., 2005, AJ, 130, 1111

[28] Carraro G., Bresolin F., Villanova S. et al., 2004, AJ, 128, 1676

[29] Carraro G., Chiosi C., Girardi L., Lia C., 2001, MNRAS, 327, 69

[30] Cayrel R., Depagne E., Spite M. et al., 2004, A&A, 416, 1117

[31] Cescutti G., François P., Matteucci F., Cayrel R., Spite M., 2006, A&A, 448, 557

[32] Cescutti G., Matteucci F., François P., Chiappini C., 2006, astro-ph/0609813

[33] Chang R. X., Hou J. L., Shu C. G., Fu C.Q., 1999, A&AS, 141, 491

[34] Chiappini C., Matteucci F., Gratton R.G., 1997, ApJ, 477, 765

[35] Chiappini C., Matteucci F., Meynet G., 2003b, A&A, 410, 257

[36] Chiappini C., Matteucci F., Padoan P., 2000, ApJ, 528, 711

[37] Chiappini C., Matteucci F., Romano D., 2001, ApJ, 554, 1044

[38] Chiappini C., Romano D., Matteucci F., 2003a, MNRAS, 339, 63

[39] Clayton D.D., Rassbach, M.E., 1967, ApJ, 168, 69

[40] Cowan J.J., Sneden C., Beers T.C. et al. 2005, ApJ, 627, 238

[41] Cowan J.J., Sneden C., Burles S., Ivans I.I., Beers T.C., Truran J.W., Lawler J.E., Primas F., Fuller G.M., Pfeiffer B., Kratz K.-L., 2002, ApJ, 572, 861

[42] Daflon, S., Cunha K., 2004, ApJ, 617, 1115

[43] Dolphin A.E., MNRAS, 2002, 332, 91

[44] Dopita M.A., Ryder S.D., 1994, ApJ, 430, 163

[45] Edvardsson B., Andersen J., Gustafsson B. et al., 1993, A&A, 275, 101

[46] Feast M. W., Walker A. R., 1987, ARA&A, 25, 345

[47] François P., Depagne E., Hill V. et al., 2007, in preparation

[48] François P., Matteucci F., Cayrel R. et al., 2004, A&A, 421, 613

[49] Freiburghaus C., Rembges J.-F., Rauscher T., Kolbe E., Thielemann F.-K., Kratz K.-L., Pfeiffer B., Cowan J.J., 1999, ApJ, 516, 381

[50] Freiburghaus C., Rosswog S., Thielemann F.-K., 1999, ApJ, 525L, 121

[51] Fulbright J.P., 2000, AJ, 120, 1841

[52] Fulbright J.P., 2002, AJ, 123, 404

[53] Fulbright, J.P., Rich R.M., Castro S., 2004, ApJ, 612, 447

[54] Gallino R., Arlandini C., Busso M., Lugaro M., Travaglio C., Straniero O., Chieffi A., Limongi M., 1998, ApJ, 497, 388

[55] Geisler D., Smith V.V., Wallerstein G., Gonzalez G., Charbonnel C., 2005, AJ, 129, 1428

[56] Gilroy K.K., Sneden C., Pilachowski C.A., Cowan J.J., 1988, ApJ, 327, 298

[57] Gratton R.G., Sneden C., 1988, A&A, 204, 193

[58] Gratton R.G., Sneden C., 1994, A&A, 287, 927

[59] Greggio, L., Renzini, A., 1983a, A&A, 118, 217

[60] Greggio, L., Renzini, A., 1983b, in. Frascati Workshop on First Stellar Generations, Vulcano, Italy, Societa Astronomica Italiana, vol. 54, no. 1, p. 311-319

[61] Grevesse N., Sauval A.J., 1998, Space Sci. Rev., 85, 161

[62] Hartwick F. 1976, ApJ, 209,418

[63] Hernandez X., Ferrara A., 2001, MNRAS, 324, 484

[64] Hernandez X., Gilmore G., Valls-Gabaud D., 2000, MNRAS, 317, 831

[65] Hill V., et al., 2002, A&A, 387, 560

[66] Honda S., Aoki W., Kajino T. et al., 2004, ApJ, 607, 474

[67] Hou J. L., Prantzos N., Boissier S., 2000, A&A, 362, 921

[68] Iben, I. Jr., Renzini A., 1982a, ApJ, 259, 79

[69] Iben, I. Jr., Renzini A., 1982b, ApJ, 263, 23

[70] Ikuta C., Arimoto N., 1999, PASJ, 51, 459

[71] Ishimaru Y., Wanajo S., 1999, ApJ, 511L, 33

[72] Ishimaru Y., Wanajo S., Aoki, W., Ryan, S.G., 2004, ApJ, 600L, 47

[73] Iwamoto, K., Brachwitz F., Nomoto K., Kishimoto N., Umeda H., Hix W.R., Thielemann F.-K., 1999, ApJS, 125, 439

[74] Johnson J.A., 2002, ApJS, 139, 219

[75] Johnson J.A., Bolte M., 2001, ApJ, 554, 888

[76] Johnson J.A., Bolte M., 2002, ApJ, 579, 616

[77] Käppeler F., Beer H., Wisshak K., 1989, Rep.Prog.Phys., 52, 945

[78] Kennicutt R.C.Jr., 1989, ApJ, 344, 685

[79] Kennicutt R.C.Jr., 1998, ApJ, 498, 541

[80] Koch A., Edvardsson B., 2002, A&A,381, 500

[81] Koch A., Grebel E.K., Harbeck D., Wilkinson M., Kleyna J., Gilimore G., Wyse R.F. G., Evans W., 2004,ANS, 325, 44

[82] Kroupa P., Tout C.A., Gilmore G. 1993, MNRAS, 262, 545

[83] Lamb S.A., Howard W.M., Truran J.W., Iben I.Jr., 1977, ApJ, 217, 213

[84] Lanfranchi G., Matteucci F., 2003, MNRAS, 345, 71

[85] Lanfranchi G., Matteucci F., 2004, MNRAS, 351, 1338

[86] Langer N., Henkel C., 1995, Space Sci. Rev., 74, 343

[87] Larson R.B., 1998, MNRAS, 301, 569

[88] Limongi M., Chieffi A., 2003, ApJ, 592, 404

[89] Luck R.E., Gieren W.P., Andrievsky S.M. et al. 2003, A&A, 401, 939

[90] Mackey J., Bromm V., Hernquist L., 2003, ApJ, 586, 1

[91] MacLow M., Ferrara A., 1999, ApJ, 513, 142

[92] Maeder A., & Meynet G., 1989, A&A, 210, 155

[93] Martin C.L., Kennicutt R.C.Jr., 2001, ApJ, 555, 301

[94] Mashonkina L., Gehren T., 2000, A&A, 364, 249

[95] Mashonkina L., Gehren T., 2001, A&A , 376, 232

[96] Mathews G.J., Bazan G., Cowan J. J., 1992, ApJ, 391, 719

[97] Mathews G.J., Cowan J. J., 1990, Nature, 345, 491

[98] Matteucci F., 1986, ApJ, 305, 81

[99] Matteucci F., 1992, ApJ, 397, 32

[100] Matteucci F., 1996, FCPh, 17, 283

[101] Matteucci F., Brocato E., 1990, ApJ, 365, 539

[102] Matteucci F., Calura F., 2005, MNRAS, 360, 447

[103] Matteucci F., Chiosi C., 1983, A&A, 123, 121

[104] Matteucci F., François P., 1989, MNRAS, 239, 885

[105] Matteucci F., Greggio L., 1986, A&A, 154, 279

[106] Matteucci F., Pipino A., 2005, MNRAS, 357, 489

[107] Matteucci F., Recchi S., 2001, ApJ, 558, 351

[108] Matteucci F., Romano D., Molaro P., 1999 A&A, 341, 45

[109] Matteucci F., Tornambé A., 1987, A&A, 185, 51

[110] Mazzali, P. A., Chugai, N. N., 1995, A&A, 303, 118

[111] McWilliam A., Preston G.W., Sneden C., Searle L., 1995, AJ, 109, 2757

[112] McWilliam A., Rich R. M., 1994, ApJS, 91, 749

[113] McWilliam A., Searle L., 1999,Ap&SS, 265, 133

[114] Meynet G., Maeder A., 2002, A&A, 390, 561.

[115] Nakamura F., Umemura M., 2001, ApJ, 548, 19

[116] Nissen P.E., Schuster W.J., 1997, A&A, 326, 751

[117] Nomoto K., Hashimoto M., Tsujimoto T., Thielemann F.-K., Kishimoto N., Kubo Y., Nakasato N., 1997, Nucl. Phys. A, 616, 79

[118] Otsuki, K., Mathews G.J., Kajino T., 2003, NewA, 8, 767

[119] Pagel B.E.J., Tautvaisiene G., 1995, MNRAS, 276, 505

[120] Pagel B.E.J., Tautvaisiene G., 1997, MNRAS, 288, 108

[121] Peters J.G., 1968, ApJ, 154, 225

[122] Pompeia L., Barbuy B., Grenon M., 2003, ApJ, 592, 1173

[123] Portinari L., Chiosi C. 1999, A&A, 350, 827

[124] Prantzos N., Boisser S., 2000, MNRAS, 313, 338

[125] Prochaska J.X., Naumov S.O., Carney B.W., McWilliam A., Wolfe A.M., 2000, AJ, 120, 2513

[126] Raiteri C.M., Gallino R., Busso M., 1992, ApJ, 387, 263

[127] Raiteri C.M., Villata M., Gallino R., Busso M., Cravanzola, A., 1999, ApJ, 518, L91

[128] Rauscher T., Heger A., Hoffmann R.D., Woosley S.E., 2002, ApJ, 576, 323

[129] Recchi S., Matteucci F., D'Ercole A., 2001, MNRAS, 322, 800

[130] Recchi S., Matteucci F., D'Ercole A., Tosi M., 2004, A&A, 426, 37

[131] Reid M.J., 1993, ARAA, 31, 345

[132] Ryan S., Norris J.E., Beers T.C., 1996, ApJ, 471, 254

[133] Sadakane K., Arimoto N., Ikuta C., Aoki W., Jablonka P., Tajitsu A., 2004, PASJ, 56, 1041

[134] Salpeter E.E., 1955, ApJ, 121, 161

[135] Sbordone L., Bonifacio P., Buonanno R., Marconi G., Monaco L., Zaggia S., 2006, astro-ph 0612125

[136] Scalo J.M., 1986, FCPh, 11, 1

[137] Scalo J.M., 1998 in "The Stellar Initial Mass Function" ASP Conf. Ser. Vol. 142 p.201

[138] Schmidt M., 1959, ApJ, 129, 243

[139] Shetrone M., 2004, astro/ph 0411030

[140] Shetrone M., Côté P., Sargent W.L.W., 2001, ApJ, 548, 59

[141] Shetrone M., Venn K.A., Tolstoy E., Primas F., 2003, AJ, 125, 684

[142] Siess L., Livio M., Lattanzio J., 2002, ApJ, 570, 329

[143] Smecker-Hane T., McWilliam A., 1999, in Hubeny I. et al., eds. Spectrophotometric Dating of Stars and Galaxies, ASP Conference Proceedings, Vol. 192, p.150

[144] Sneden C., Cowan J.J., Ivans I.I., Fuller G.M., Burles S., Beers T.C., Lawler J.E., 2000, ApJ, 533, 139

[145] Sneden C., Cowan J.J., Burris D.L., Truran J.W., 1998, ApJ, 496, 235

[146] Sneden C., Cowan J.J., Lavier J.E., Burles S., Beers T.C., Fuller G.M., 2002, ApJ, 566, L25

[147] Sneden C., Cowan J.J., Lawler J.E., Ivans I.I., Burles S., Beers T.C., Primas F., Hill V., Truran J.W., Fuller G.M., Pfeiffer B., Kratz K.-L., 2003, ApJ, 591, 936

[148] Stephens A., 1999, AJ, 117, 1771

[149] Stephens A., Boesgaard A.M., 2002, AJ, 123, 1647

[150] Thielemann F.K., Nomoto K., Hashimoto M., 1996, ApJ, 460, 408

[151] Tinsley B.M., 1979, ApJ, 229, 1046

[152] Tinsley B.M., 1980, FCPh, 5, 287

[153] Tolstoy E., Venn K.A., Shetrone M., Primas F., Hill V., Kaufer A., Szeifert T., 2003, AJ, 125, 707

[154] Tosi M., 1988, A&A, 197, 338

[157] Travaglio C., Galli D., Burkert A., 2001, ApJ, 547, 217

[156] Travaglio C., Galli D., Gallino R. et al., 1999, ApJ, 521, 691

[157] Travaglio C., Gallino R., Arnone E., Cowan J., Jordan F., Sneden C., 2004, ApJ, 601 864

[158] Truran J.W., 1981, A&A, 97, 391

[159] Tsujimoto T., Shigeyama T., Yoshii Y., 1999, ApJ, 519L, 63

[160] Umeda H., Nomoto K. 2002, ApJ, 565, 385

[161] van den Hoek L.B., Groenewegen M.A.T. 1997, A&A Suppl., 123, 305

[162] Venn K. A., Irwin M., Shetrone M.D., Tout, C.A., Hill V., Tolstoy E., 2004, AJ, 128, 1177

[163] Ventura P., D'Antona F., Mazzitelli I., 2002, A&A, 393, 21

[164] Wanajo S., Tamamura M., Itoh N., Nomoto K., Ishimaru Y., Beers T.C., Nozawa S., 2003, ApJ, 593, 968

[165] Whelan J., Iben I. Jr., 1973, ApJ, 186, 1007

[166] Wheeler J. C., Sneden C., Truran J.W.Jr., 1989, ARA&A, 27, 279

[167] Woolf V.M., Tomkin J., Lambert D.L., 1995, ApJ, 453, 660

[168] Woosley S.E., Hoffmann, R.D., 1992, ApJ, 395, 202

[169] Woosley S.E., Weaver, T.A., 1995, ApJ, 101, 181

[170] Woosley S.E., Wilson J.R., Mathews G.J., Hoffman R.D., Meyer B.S., 1994, ApJ, 433, 229

[171] Yong D., Carney B.W., Teixera de Almeida M.L, 2005, AJ, 130, 597

[172] Yong D., Carney B.W., Teixera de Almeida M.L, Pohl B.L, 2006, AJ, 131, 2256

Acknowledgements

First of all, I wish to thank Francesca Matteucci, who led me during these three years. All her experience, all her suggestions and criticisms made me grow up as a scientist but also as a person. My gratitude goes also to Patrick François, who provided new and unpublished data as well as many unvaluable suggestions and for inviting me at the Observatoire de Paris. I wish to warmly thank Gustavo Lanfranchi for the fruitful collaboration on the chemical evolution of dwarf spheroidal galaxies. I also wish to thank Cristina Chappini, Francesco Calura, Antonio Pipino and Simone Recchi for all the interesting and stimulating discussions. Finally, I whish to thank professor Jim Truran for his enlightening suggestions.

List of Figures

List of Tables